Leonard Knöll

Master Thesis supervised by
Univ.-Prof. Dipl.-Ing. Dr.mont. Gerhard Thonhauser
Dipl.-Ing. B.Sc. Asad Elmgerbi

The Process of Building a Mechanical Earth Model Using Well Data

dpe DEPARTMENT PETROLEUM ENGINEERING

MONTAN UNIVERSITÄT

This work is dedicated to my parents who supported me
no matter which decisions I have taken in life.

Affidavit

I declare in lieu of oath that I wrote this thesis and performed the associated research myself using only literature cited in this volume.

Eidesstattliche Erklärung

Ich erkläre an Eides statt, dass ich diese Arbeit selbständig verfasst, andere als die angegebenen Quellen und Hilfsmittel nicht benutzt und mich auch sonst keiner unerlaubten Hilfsmittel bedient habe.

_____

Name, 28 November 2016

Abstract

Modern well construction projects are technically and economically challenging. In order to complete the well in time and within budget the non-productive time which is associated with lost circulation, kicks, wellbore instability and anomalous pore pressure regimes has to be minimized. These issues are strongly related to the stress regime in the area. Therefore, a good knowledge of stress regime in the area of interest helps to mitigate the delay caused by the mentioned issues, consequently cost and risks are reduced. Using log measurements, a mechanical earth model (MEM) can be built so instability zones are predicted and issues avoided.

The mechanical earth model is a numerical representation of the state of stress and rock mechanical properties for a specific stratigraphic section in a field or basin. The model is linked to geologic structure through the local stratigraphy and seismic data. In addition to property distribution (e.g. density, porosity) the model incorporates the pore pressure, state of stress and rock mechanical properties (e.g. UCS, friction angle, Young's Modulus and Poisson's Ratio). The stresses on the reservoir are caused by the overburden weight, any superimposed tectonic forces, and by production and injection. The properties are derived from various logs e.g. sonic log, density log using various methods. Before and during drilling the model is calibrated using core and pressure test results. After analysing rock failure, a safe mud weight can be recommended.

At first, this work introduces the topic by discussing what a well-centric 1D-MEM is and the potential economic benefits are elaborated.

In the second part, it presents the required equations and methods to derive rock properties from log data and other sources and explains how the stress state and a safe mud weight window not causing failure can be derived.

In the third part the presented equations and methods are applied to an offshore well data and a MEM for that well is built. The modelling process is described and results are presented.

Finally, the process, results and occurred problems are discussed. It closes by concluding problems and potential benefits of the MEM in general and discusses future potential of the method and possible research on it.

Zusammenfassung

Moderne Bohrprojekte sind technisch und wirtschaftlich herausfordernd. Um die Bohrung im Rahmen der geplanten Zeit und des geplanten Budgets abteufen zu können, muss die "non-productive time" aus Bohrlochinstabilität minimiert werden. Die Instabilität durch Kicks und Spülungsverlust hängt mit dem Spannungszustand im Gestein zusammen. Kennt man also die Spannungen, ist es möglich die Stabilität zu verbessern und so Verzögerungen zu vermeiden. Dadurch werden Zeit und Kosten gespart und Risiken reduziert. Mit Hilfe von Bohrlochlogs lässt sich ein Mechanical Earth Model (MEM) erstellen um Problemzonen vorherzusehen und Instabilität zu vermeiden.

Das MEM ist eine numerische Repräsentation des Spannungszustands und der mechanischen Gesteineigenschaften für einen bestimmten Bereich eines Feldes. Das Modell ist über die lokale Stratigraphie und seismische Daten in die umgebende Geologie eingebunden. Zusätzlich zur Verteilung der Dichte, Porosität, etc. enthält das Modell den Spannungszustand und mechanische Gesteinseigenschaften (einaxiale Druckfestigkeit, Reibungswinkel, Elastizitätsmodul, Poissonzahl, etc.). Die Spannungen im Gestein werden verursacht durch lithostatischen Druck, tektonische Spannung, Injektionen und Förderung. Die Eigenschaften werden aus verschiedenen Bohrlochlogs wie z.B. Akustik- und Dichtelogs abgeleitet. Vor und während des Bohrens werden Daten aus Bohrkernmessungen und LOT zur Kalibrierung des Modells verwendet. Nach Analyse der Bedingungen für das Versagen des Gesteins, kann eine Empfehlung für die Bohrspülungsdichte gemacht werden.

Zuerst führt diese Arbeit generell in die Thematik 1D MEM ein und behandelt das Einsparungspotential.

Im zweiten Teil werden die Gleichungen und Methoden vorgestellt, die zum Ableiten der Gesteinsparameter aus Bohrlochlogs und anderen Quellen benötigt werden. Außerdem wird erklärt, wie daraus die Spannungen und sichere Bohrspülungsdichte abgeleitet werden.

Im dritten Teil werden die vorgestellten Gleichungen und Methoden auf Daten aus einer Offshorebohrung angewendet und ein MEM entwickelt. Der Modellierungsprozess wird beschrieben und Resultate werden präsentiert.

Schließlich werden der Prozess, die Resultate und aufgetretene Probleme diskutiert. Die Arbeit schließt mit Schlussfolgerungen zu Problemen und potentiellen Vorzügen des MEM generell und zeigt mögliches Zukunftspotential auf für das MEM und weitere Forschung zum Thema.

Acknowledgements

I thank my second advisor Dipl.-Ing. Asad Elmgerbi for supporting me and making this thesis possible. He supplied the necessary data to conduct this thesis and replaced my previous advisor.

I am also very grateful to the German taxpayers who make my subsidized student loans possible and the Austrian taxpayers for paying for my master's degree. This makes social upwards mobility possible.

Furthermore, I thank the staff and lecturers at the university and my friends of various backgrounds that always supported me.

Contents

Chapter 1 Introduction 1
1.1 Problem Overview 1
1.2 Motivation 3
1.3 Objectives 5
Chapter 2 MEM Literature Review 6
2.1 Overburden Stress 12
2.2 Elastic Properties of the Rocks 13
2.3 Rock Strength Parameters 16
2.4 Pore Pressure 21
2.4.1 Eaton's Method 22
2.4.2 Bowers Method 25
2.4.3 Complications 26
2.5 Horizontal Stresses 27
2.5.1 Minimum Horizontal Stress 29
2.5.2 Maximum Horizontal Stress 33
2.5.3 Stress Orientation 36
2.6 Failure Mechanisms 37
2.6.1 Mohr Coulomb 38
2.6.2 Drucker Prager 40
2.6.3 Modified Lade 40
2.6.4 Mogi Coulomb 41
2.7 Mud Window and Wellbore Stability 42
Chapter 3 MEM Building Process (Case Study) 46
3.1 Well Overview 47
3.2 Data Gathering 49
3.3 Log and Core Data 50
3.4 Data Conversion and Quality Control 51
3.5 Overburden Stress 53
3.6 Elastic Properties 54
3.7 Rock Strength 57
3.8 Pore Pressure 60
3.9 Min. and Max. Horizontal Stress 61
3.10 Induced Stresses 63

3.11 Failure and Stability 65
3.12 Discussion 73
3.12.1 Trouble Zone 1 74
3.12.2 Trouble Zone 2 74
3.12.3 Trouble Zone 3 75
3.12.4 Recommendation for Casing Seat Selection and Mud Weight 76
Chapter 4 Conclusion and Recommendations 79
4.1 Conclusion 79
4.2 Recommendations and Future Work 81

Chapter 1 Introduction

1.1 Problem Overview

Wellbore instability is one of the most critical challenges affecting the entire life cycle of a well, not only the well construction phases. It is one of the major causes of non-productive time (NPT) by causing issues such as borehole collapse, lost circulation, stuck pipe, sand production and other related well failure events. NPT is any event that interrupts the progress of a planned operation causing a time delay; it includes the total time needed to resolve the problem until the operation is resumed again from the point or the depth where the NPT event occurred.

According to Halliburton, NPT typically accounts for up to 32 percent of drilling operations costs for deep-water wells (Halliburton 2016). Schlumberger states that geomechanical problems are associated with 40 percent of the drilling related NPT in deep -water and other challenging environments. (Schlumberger 2016). The total cost of geomechanics related issues is multiple billions of dollars. Another source states that on average, 22% of the drilling budget can be attributed to wellbore related NPT. Fifty percent of this NPT is associated with geomechanics related issues (stability, lost circulation, stuck pipe, etc.) meaning 11% of the drilling budget (Mody 2013).

Figure 1 and Figure 2 show instability as percentage of total well time for sub salt and non sub salt wellbores in the Gulf of Mexico. The following sections deal with their NPT.

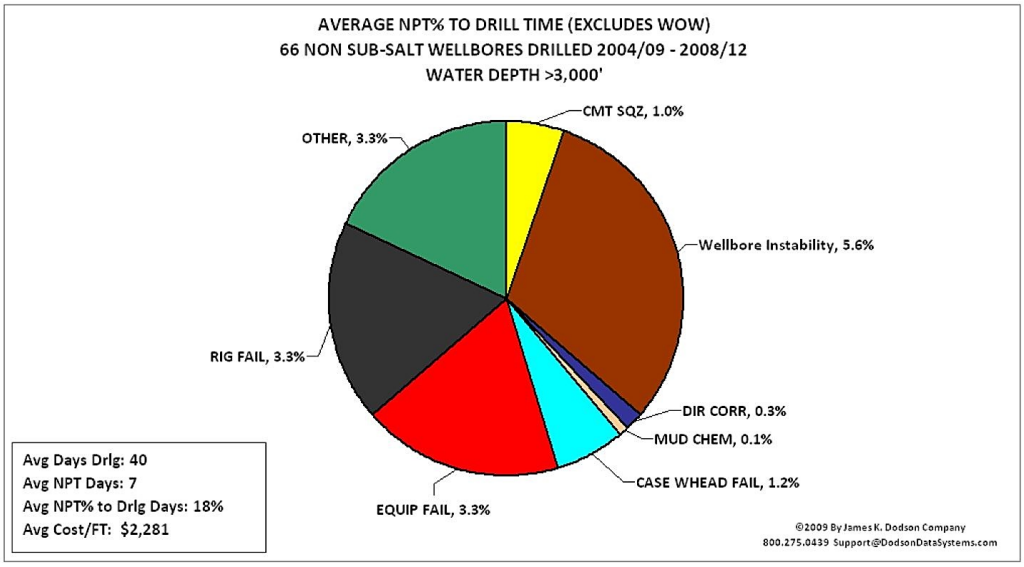

Figure 1: NPT for non sub-salt wellbores in the Gulf of Mexico (York et al. 2009)

As it can be seen from Figure 1, 5.6% of total well cost for these wells is attributed to wellbore instability. For the average cost/ft of $ 2,281 that equals 127.73 $/ft which would mean $ 2,550,000 for a 20,000 ft well.

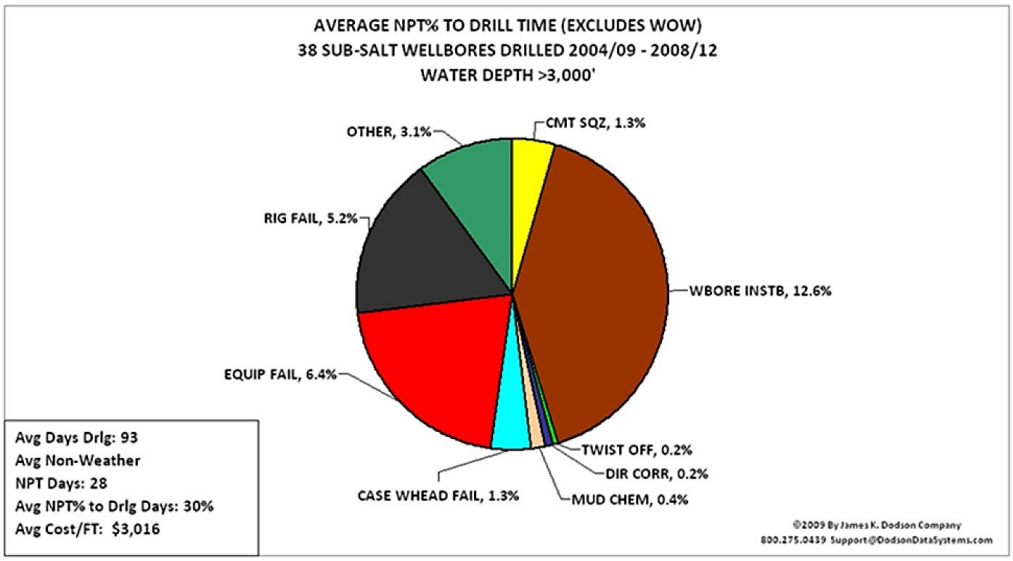

Figure 2: NPT for sub-salt wellbores in the Gulf of Mexico (York et al. 2009)

For the sub-salt wells the costs are even higher. Wellbore instability here caused cost of 12.6% of total well cost. For the average cost/ft of $ 3,016 that equals 380.02 $/ft which would mean $ 7,600,300 for a 20,000 ft well.

In summary, the unexpected instability events increase risk, reduce safety, potentially harm crew and cause non-productive time. Moreover, they are costly and can easily lead to a cost overrun if they occur frequently. Successful construction of wells containing trouble zones depends on accurate analysis of all available well data to deliver the well and its objectives. Being familiar with the local drilling environment can substantially reduce risk. Unfortunately, often data and learning from previous well construction attempts are ignored. The next well design is left unchanged expecting different results than on the previous failed attempt. Although this approach is illogical it has too often been the norm in many offshore environments as proven by the amount of money spent on avoiding issues drilling known and expected trouble zones. (York et al. 2009)

In many cases the best drilling practices used to address trouble zones are limited to just a few conventional methods with limited effectiveness. A lack of rock mechanics knowledge can prevent the most efficient solution from being applied. Some operators are implementing planning programs that integrate the latest processes and technologies to address drilling risks upfront. Cutting-edge technologies such as managed pressure drilling, drilling with casing or liners, solid expendable casing have been highly effective. Implementing proactive analysis and evaluation processes and

applying the latest tools and techniques can efficiently address operational risks to ultimately reduce NPT and associated costs.

1.2 Motivation

In the previous section the high costs of wellbore instability were discussed. This clearly shows that the present cost saving potential is high if wellbore instability events could be better controlled or ideally prevented. One possibility to reduce the frequency of instability events is to analyze the geomechanical situation and incorporate it into the well plan to design parameters.

A popular way of using geomechanics to improve well design is to analyse the state of in situ stresses and use them to derive a safe mud weight that will likely not cause instability issues. A typical plot of these stresses is shown in Figure 3.

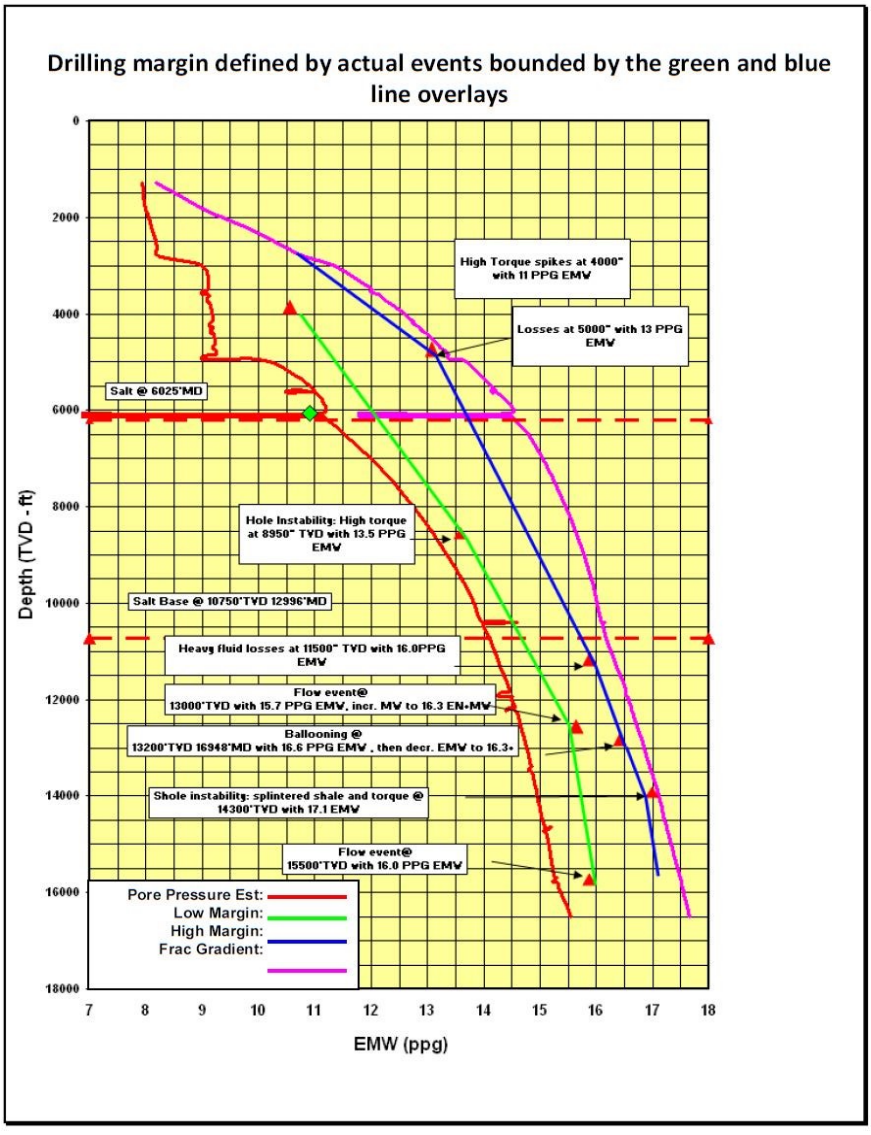

Figure 3: Typical deep-water narrow margin PP/FG curve (York et al. 2009)

The low and high margin were defined using historically occurred instability events indicated by red triangles and a description in a text box. It is easy to see that instability occurs before the fracture pressure or pore pressure are reached which makes clear that the calculated stresses always have an underlying uncertainty. Taking the instability events into account, an upper and lower margin for the mud weight was set. Using a mud weight between these margins, instability can be mitigated.

To calculate these stresses and set these margins a so called Mechanical Earth Model (MEM) can be established. It takes geomechanics into account to derive the safe mud weight window. Chapter 2 of this work deals with the MEM in detail.

Case studies have been published where a Mechanical Earth Model (MEM) has been built after wells in a field encountered stability issues. The model helped to drill further wells with fewer problems. One case published by Qiu et al. (Qiu et al. 2013) is about a horizontal well drilled in a Libyan field. Figure 4 shows root causes for NPT for that well. As stated before, it can be seen that the majority of issues are geomechanics related. By analyzing the issues and their depths and using log data a wellbore stability prediction for the planned well has been created. The mud weights have been changed. Sticking to the plan for the new well resulted in problem free operations. That way NPT has been reduced and thus costs have been reduced.

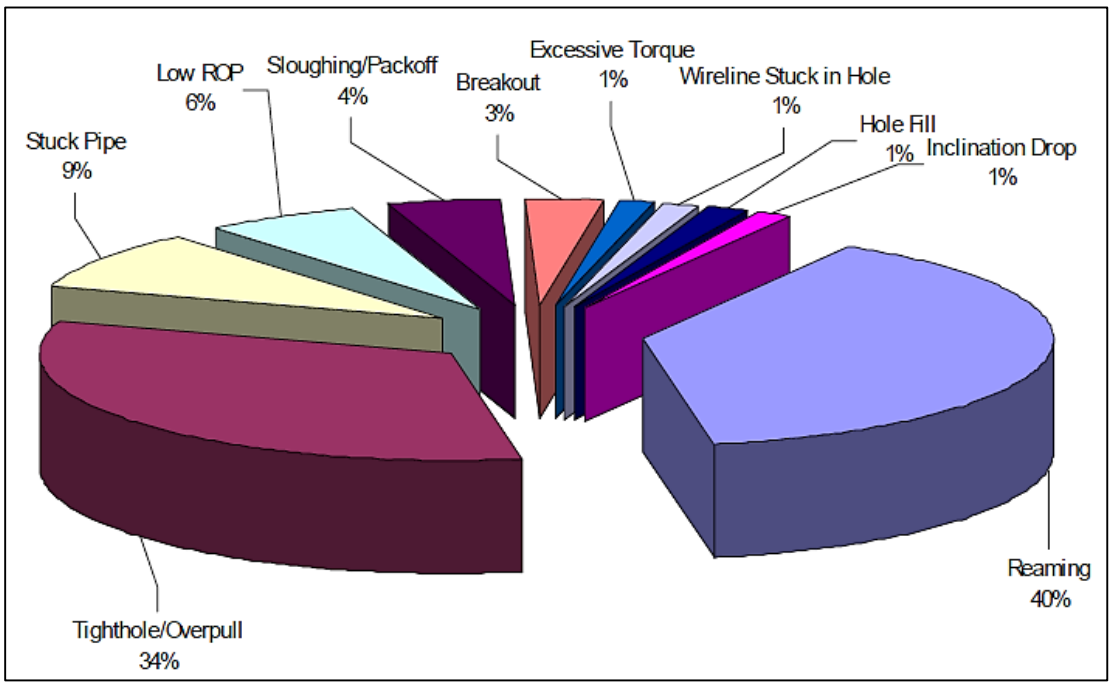

Figure 4: Statistical NPT breakdown by drilling event type (Qiu et al. 2013)

1.3 Objectives

In the previous sections it was shown that wellbore stability can cause a large fraction of the NPT so reducing the number of instability events would lead to less NPT and consequently higher cost saving. Since most of these instability events stem from geomechanical reasons, analyzing the geomechanical situation can help gain knowledge about when and where instability could occur and how it can be prevented. One of the tools of analysis is the MEM which is subject of this thesis. The main goal of this thesis is to prove that one dimensional MEM can be used to build reliable safe mud window. In order for this thesis to be able to achieve the mentioned goal, the following objectives were set to be the main focus for the thesis.

- Create a literature review that summarizes the necessary theory, equations and methods required to build a 1D MEM
- Apply the theory to an offshore well data set, make necessary assumptions, build a 1D MEM for that well and showcase the resulting plots
- Discuss the results, modeling process, chances and risks

The following flowchart shows the general workflow of this thesis.

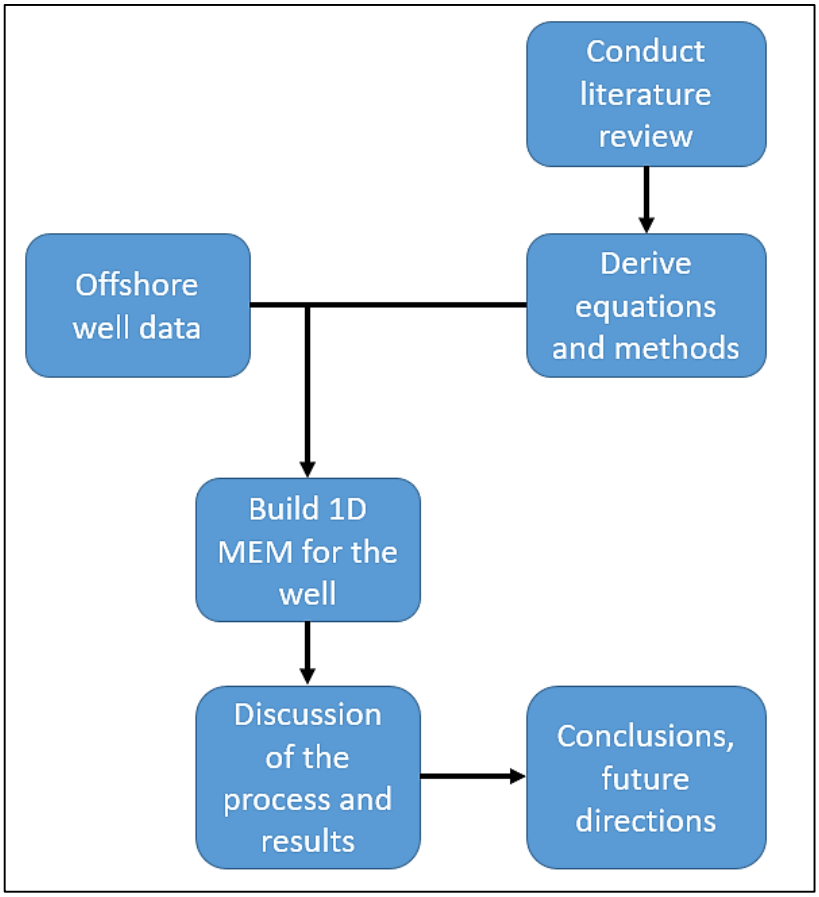

Figure 5 Thesis flowchart

Chapter 2 MEM Literature Review

Many of today's well construction projects are technically and economically challenging. Examples include deep-water exploration wells in the Gulf of Mexico, offshore field development projects such as Hibernia, Newfoundland, Canada and onshore field development projects in tectonically active regions such as the Cusiana field in Colombia. (Plumb et al. 2013)

Wells with anomalous pore pressure and fracture gradient profiles require a good pre-drill pore pressure and fracture gradient prediction in order to design a suitable casing program and safe mud window. A casing program designed on a profile significantly less problematic than that encountered may compromise the attainable total depth (TD) of the well. The cost of materials and rig time spent running extra casing significantly adds to the cost of the well. The risk of taking kicks which can be both costly and dangerous can also be reduced by a more rigorous pre-drill pore pressure prediction coupled with real-time pore pressure analysis from Logging While Drilling (LWD) measurements. In the deep-water Gulf of Mexico there are examples of wells which require a good mechanical earth model (MEM) in order to be drilled safely and economically. Despite decades of industry attention, wellbore instability is responsible for many costly stuck pipe incidents. Stuck pipe is responsible for lost bottom hole assemblies (BHAs) and considerable NPT spent freeing pipe, performing additional wiper trips and hole cleaning. In cases where wellbore stability problems are severe, the economics of developing a field can become challenging. (Plumb et al. 2013)

Minimizing non-productive time associated with wellbore instability and unexpected pore pressure regimes reduces the risk of dangerous accidents and is required to complete the well on time and within budget. But this is a complex task that requires thorough pre-spud planning to identify drilling risks and geological hazards and to develop contingency plans for handling those risks. It requires an understanding of the field's geomechanics. Gaining good knowledge and establishing a successful plan requires a process for building a mechanical earth model and using it to provide information for decision makers in time. Building a mechanical earth model during the well planning phase and revising it in real time has proven to be extremely valuable in delivering complex wells safely while minimizing unplanned well construction costs and accelerating learning about the field. Information developed and applied during early field delineation has payback extending over the life of the field. (Plumb et al. 2013)

The mechanical earth model is a numerical representation of the state of in situ stresses and rock mechanical properties for a specific stratigraphic section in a field or basin. The model is linked to geologic structure through the local stratigraphy and seismic data. Other than stratigraphic information it contains various types of information like mechanical parameters, stress state in the rock and failure mechanics that can be used for many different decisions. The most popular decision that the literature discusses is the safe mud weight window estimation but many others are affected by the results. Table 1 illustrates the relationship between components of the mechanical earth model and drilling planning and execution decisions. This work focuses on how the model is build and used to estimate the safe mud weight to improve stability.

Drilling Decision	**Earth Stresses, pore pressure**	**Rock Failure Mechanisms**	**Rock Mechanical Parameters**	**Geologic Structure Stratigraphy**
Well location	X	X	X	X
Rig selection and BOP rating	X			
Trajectory analysis	X	X	X	X
Casing design	X			X
Safe Mud weigh	X			
Wellbore stability	X	X	X	X
Drilling fluids	X	X	X	X
Drilling practices	X	X	X	X
Cementing Strategy	X			
Bit selection			X	X

Table 1: Relationship between drilling decisions and the mechanical earth model (Plumb et al. 2013)

In its basic form, the MEM consists of depth profiles: of the elastic and/or elasto-plastic parameters, rock strength and the earth stresses referenced to the local stratigraphic section.

Figure 6 shows a 1-dimensional representation of a mechanical earth model and links to the stratigraphy and 3D-seismic cube. From left to right the profiles include: Poisson's ratio (ν), Young's modulus (E), unconfined compressive strength (UCS), friction angle (Φ), pore pressure (P_p), minimum horizontal stress (σ_h), maximum horizontal stress (σ_H), vertical stress (σ_v), and the direction of horizontal stress axes.

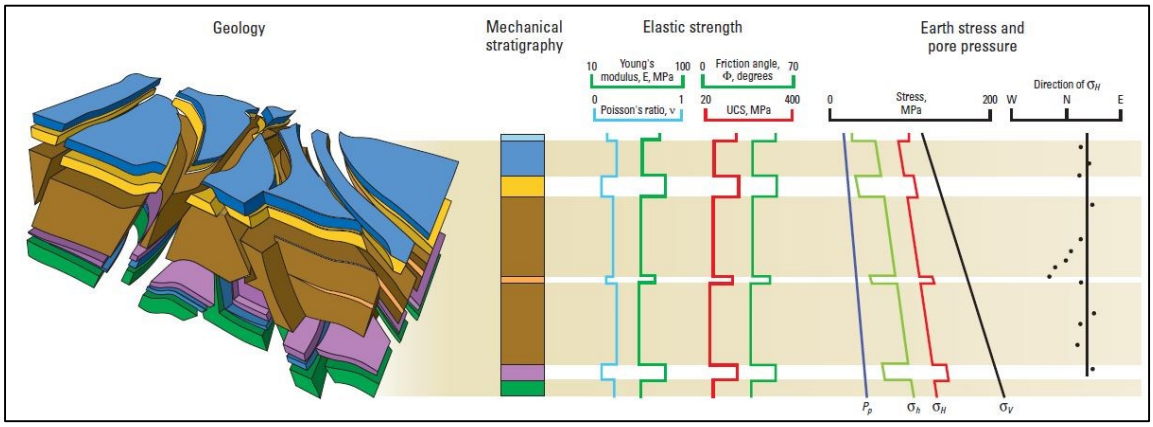

Figure 6: Concept of the MEM (Ali, A. H. A. et al. 2003)

Lithological variations in MEM parameters are governed by the mechanical stratigraphy. Research has shown that rock strength and earth stresses profiles are modulated according to the nature of the dominant load-bearing solid phase. The mechanical stratigraphy is a bimodal textural model of a stratigraphic sequence. The bimodal classification differentiates rocks with clays as the dominant load-bearing solid from rocks with quartz or carbonate minerals as the dominant load-bearing solid. Petrophysical models are then used to transform the mechanical stratigraphy into elastic, elasto-plastic and rock strength profiles. Lateral variations in mechanical properties, associated with geologic structure, are captured by linking the mechanical stratigraphy to a 3-dimensional (3D) framework model. The 3D-framework model consists of surfaces, such as formation tops and faults. The surfaces are interpreted from seismic data, guided by log data and the geologist's lithostratigraphic model. In its most complete form, the MEM consists of a full 3D description of pore pressure, stress and mechanical properties. In practice, the complexity of the model evolves in step with the acquisition of new information. From exploration to development, the model evolves from of a sparse set of 1- dimensional profiles to a full 3D description of rock properties and earth stresses. The degree of detail captured by the model will vary from field to field depending on the perceived operational risks. (Plumb et al. 2013) This thesis will mainly deal with 1-dimensional MEM.

The mechanical earth model concept is one of the practical outcomes of the Cusiana study. But the need for information about the earth to improve stability has been known for many years. Throughout the 1980s the practical theory of wellbore stability advanced slowly in step with the development of faster computers and better logging tools such as sonic and imaging logs. Wellbore stability modeling techniques of various levels of complexity have been established at that time. A breakthrough occurred in the early 1990s when BP encountered severe wellbore instability in the Cusiana field in Colombia. The at that time conventional approaches to solving stability problems simply did not work (Last et al. 2013)

It took a multi-company team of geoscientists and engineers almost 1 year to compile enough geomechanics information about the field to affect an improvement in the drilling performance. During the time when the model was being compiled wellbore stability was a continuing problem. This experience motivated the development of the mechanical earth model. (Plumb et al. 2013)

Few fields in the world today have suffered wellbore stability problems as severe as those in Cusiana. But today operators and service companies are expected to drill more complex wells in less time and at lower cost. Under these constraints, even relatively minor-wellbore stability problems can be extremely expensive (from $100,000 to $250,000/day offshore). Under these circumstances, the tendency to design wells based on close geology can lead to costly surprises. Important lessons from Cusiana that apply equally well to lower-risk projects include (Plumb et al. 2013):

- Use of all available data to develop geomechanics knowledge of the field.
- Balance the complexity of data analysis with available time and information.
- The value of three specific types of information: failure mechanisms, state of stress and rock mechanical properties.
- The value of real-time information.
- The value of data management and good communication.

Well managed and communicated data leads to a better model. Derived information about the state of stress, rock mechanical properties and failure will be more accurate. Real time information can be used to update the model to enable reactions if the reality deviates from assumptions made from offset well data. High quality data that is updated real time leads to the best model with lowest uncertainty leading to the best

stability predictions possible. The more expensive the project is, the more costs are at stake, the more important this becomes.

Drilling a high risk well without gathering and analyzing the geomechanical information can lead to various surprises that raise questions. The proper action would not be clear. For example, instability could suddenly appear. Would an increase or decrease of mud weight or a change in drilling fluid or a combination help? Why did the previous azimuth not show any issues but the current one causing problems? Pore pressure is unexpectedly high or low. Is the current casing plan still safe? If these problems occur, substantial cost overruns can occur. An earth model incorporated in the planning phase that gets monitored and updated while drilling will have initial costs but can help minimize the economic impact of later occurring instability problems.

An integrated geomechanical process that has been used to successfully minimize risks on high-risk projects looks as follows:

1. Build a MEM. It represents all geological and rock mechanics information that currently exists in the field.
2. Use MEM to forecast wellbore stability along the planned well path.
3. Monitor the data while drilling to discover anomalies. They indicate flaws in the data or the MEM.
4. Analyze the anomalies to determine the sources of error. Immediate action on the rig can be initiated if required.
5. Correct the MEM. (e.g. abnormally low or high pore pressure)

Potentially valuable information is captured and resulting stability forecasts are revised by revisions to the model when new data is acquired. The loop continues. This requires team work and excellent communications among the planning team, at the rig site and in between. Recent experience has shown that an initial MEM can be generated for most fields in about 1 month (Plumb et al. 2013). It is then refined continuously while drilling and as new wells are drilled. Table 2 shows typical sources of information used to acquire data such as rock properties that is required to construct a MEM.

Property profiled	Source logs	Other sources
Mechanical stratigraphy	Gamma ray, density, resistivity, sonic compressional velocity (v_p)	Cuttings, cavings, sequence stratigraphy
Pore pressure (P_p)	v_p, check-shot survey, resistivity	Interval velocity from seismic data, formation integrity test, daily drilling reports
Overburden stress (σ_v)	Bulk density	Cuttings
Stress direction	Oriented multiarm calipers, borehole images, oriented velocity anisotropy	Structural maps, 3D seismic data
Minimum horizontal stress (σ_h)	v_p and sonic shear velocity (v_s), wireline stress tool	P_p, leakoff tests, extended leakoff tests, microfrac, step-rate injection tests, local or regional database, daily drilling reports, modeling
Maximum horizontal stress (σ_H)	Borehole images	P_p, σ_h, rock strength, database, wellbore stress model
Elastic parameters [Young's modulus (E), shear modulus (G), Poisson's ratio (ν)	v_p and v_s, bulk density	Database, laboratory core tests, cavings
Rock-strength parameter [unconfined compressive strength (UCS), friction angle (ϕ)]	v_p and v_s, bulk density, mechanical stratigraphy	Database, laboratory core tests, cavings
Failure mechanisms	Borehole image, oriented multiarm caliper	Daily drilling reports, cavings

Table 2: Data required for building an MEM (Ali, A. H. A. et al. 2003)

The log data can either be acquired by using wireline tools or logging while drilling tools. It is compiled from various disciplines like drilling engineers, geologists, mud loggers, reservoir engineers, etc. and then organized onto a computer system. From there it is first processed (editing, QC, etc.) and then interpreted to receive geomechanics parameters like the rock strength, pore pressure, various stresses, etc. The degree of detail in the MEM depends on the operational needs and risks of the field. It could be a simple one-dimensional set of depth profiles showing rock properties and stresses or a sophisticated 3D model.

The MEM created before drilling will be based on historical and offset data so it will contain uncertainties and be out of date. While drilling, the model is then updated. A completed MEM is also a valuable source of information for future wells and should be saved and managed properly for future use. Figure 7 shows the typical workflow for constructing a MEM. It has been used to successfully build an MEM and save costs and reduce by Ahmed et al. (Ahmed et al. 2014)

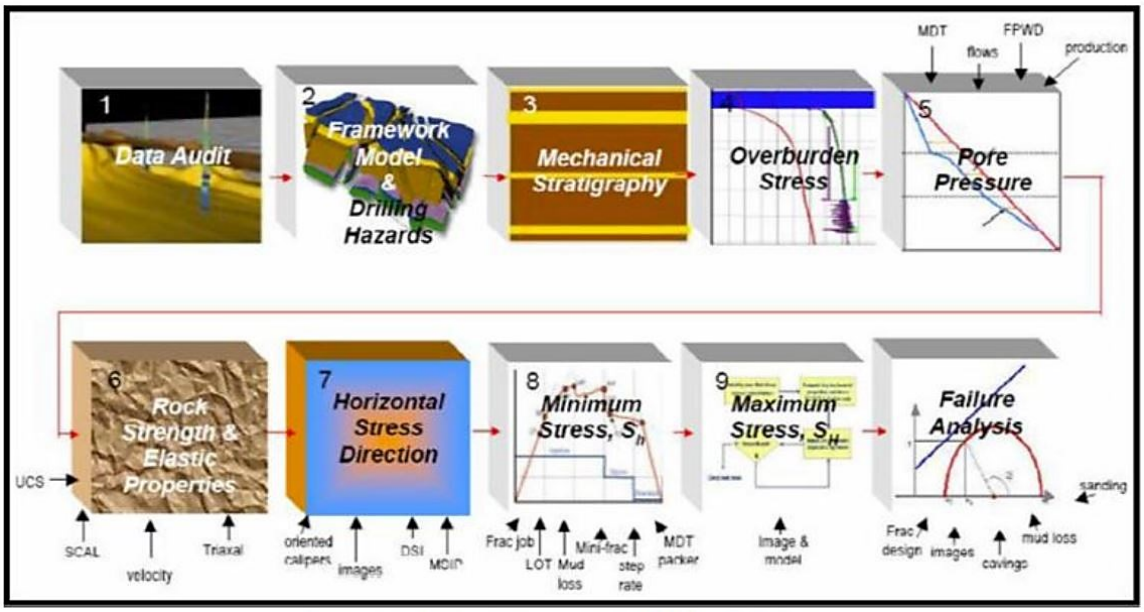

Figure 7: MEM construction workflow (Ahmed et al. 2014)

The following part of this chapter deals with the required properties for the MEM. It discusses which rock parameters are required and how they can be derived from log measurements and how they can be calibrated using Leak of test and core data. It makes clear which stresses are required for a stability analysis and shows how they can be derived from the rock properties. As shown in Figure 7 it finally deals with rock failure analysis where the calculated stresses are required to derive when rock failure occurs. This allows deriving the maximum permitted wellbore pressure which is linked to the used mud weight; eventually mud weights can be estimated and safe mud window can be developed.

2.1 Overburden Stress

The overburden stress or vertical stress (σ_v) is induced by the weight of the overlying formations. The typical source to determine it is the density log data. The bulk density is integrated over the overburden depth and multiplied by the gravitational constant to receive the resulting vertical stress. This can be expressed by Equation 1. If a formation

is not logged exponential extrapolation is sometimes used to model the unlogged region.

$$\sigma_v = \int_0^z \rho(z)\, g\, dz \tag{1}$$

Where σ_v is the vertical stress, $\rho(z)$ the bulk density at depth z and g the gravitational constant.

Another local source would be analyzing the cuttings at the surface to receive the density at the current depth. Continuous analysis of the cuttings can lead to a continuous density profile.

2.2 Elastic Properties of the Rocks

Young's Modulus (E), shear modulus (G) and Poisson's ratio (ν) can be acquired via core analysis and are then called static elastic properties. Doing so only yields information about the depth from which the core was taken. To receive continuous information, the properties are usually derived from sonic log measurements. These are called dynamic elastic properties.

The dynamic elastic properties do not equal the static elastic properties obtained through laboratory tests. This is due to strain magnitude. The acoustic measurements are done using a very small energy pulse which is reversible and so the dynamic moduli are obtained within a perfectly elastic regime. For core measurements, however, large strains have to be applied during loading, some of which are irreversible. The measured moduli are therefore not purely elastic but introduce additional irreversible deformation caused by friction (plastic part). This means the static strains are always larger than the dynamic strains so the static elastic moduli are always smaller than the dynamic elastic moduli. (Adisornsuapwat et al. 2013)

In order to obtain static elastic properties from the dynamic properties, correlations have to be used. For example, the dynamic data can be correlated against core data or the correlation can be acquired from an already drilled offset well nearby. There have also been some correlations published in literature and companies hold proprietary information about such correlations. The following equations can be used to derive dynamic properties from sonic log data:

$$G_{dyn} = 13474.45 \frac{\rho_b}{(\Delta t_s)^2} \quad (2)$$

$$K_{dyn} = 13474.45 \frac{\rho_b}{(\Delta t_c)^2} - \frac{4}{3} G_{dyn} \quad (3)$$

$$E_{dyn} = \frac{9 G_{dyn} K_{dyn}}{G_{dyn} + 3K_{dyn}} \quad (4)$$

$$\nu_{dyn} = \frac{3K_{dyn} - 2G_{dyn}}{6K_{dyn} + 2G_{dyn}} \quad (5)$$

Where ϱ_b is the bulk density in g/cm³

Δt_s the shear wave slowness in μs/ft

Δt_c the compressional wave slowness in μs/ft

G_{dyn} the dynamic Shear Modulus in Mpsi

K_{dyn} the dynamic Bulk Modulus in Mpsi

E_{dyn} the dynamic Young's Modulus in Mpsi

ν_{dyn} the dynamic Poisson's Ratio

13474.45 a conversion factor

The next step is to correlate this data to static data (for example core test results) to receive the continuous static data profiles. There have also been some correlations for certain types of rocks or certain geographical areas published. The following equation can be used to correlate dynamic to static parameters:

$$E_{static} = a * e\text{^}(b * E_{dyn}) \quad (6)$$

Where a and b are constants. It can also be used for the other dynamic properties respectively. (Haidary et al. 2015)

Another suggested relationship is as follows:

$$E_{static} = a * {E_{dyn}}^b \quad (7)$$

To find the best fitting correlation multiple approaches should be taken and various published relationships should be considered. Table 3 shows some published correlations to receive the unconfined compressive strength (UCS) or the static Young's Modulus.

Lithology	Equation	Reference
Igneous and Metamorphic	$E_s = 1.263\ E_d - 29.5$	King (1983)
Igneous and Metamorphic	$UCS = 4.31\left(\frac{E_d}{10}\right)^{1.705}$	King (1983)
Sedimentary	$E_s = 0.74\ E_d - 0.82$	Eissa and Kazi (1988)
Sedimentary	$\log(E_s) = 0.02 + 0.7\log(\rho E_d)$	Eissa and Kazi (1988)
Sedimentary	$E_s = 0.018\ E_d^2 + 0.422\ E_d$	Lacy (1997)
Sedimentary	$UCS = 0.278\ E_s^2 + 2.458\ E_s$	Lacy (1997)
Soft Rocks	$UCS = 2.28 + 4.0189\ E_s$	Bradford et al. (1988)
Hard Rocks (E_s > 15 Gpa)	$E_s = 1.153\ E_d - 15.2$	Nur and Wang (1999)
Shale	$UCS = 0.77\ v_p^{2.93}$	Horsrud (2001)
Shale	$E_s = 0.076\ v_p^{3.23}$	Horsrud (2001)
Shale	$E_s = 0.0158\ E_d^{2.74}$	Ohen (2003)
Mudstone	$E_s = 0.103\ UCS^{1.086}$	Lashkaripour (2002)
Limestone	$E_s = 0.541\ E_d + 12.852$	Ameen et al. (2009)
Limestone	$UCS = 2.94\ (\frac{E_s^{0.83}}{\Phi^{0.088}})$	Asef and Farrokhrouz (2010)
Different Rocks	$UCS = 2.304\ v_p^{2.43}$	Kilic and Teymen (2008)

Table 3: Various correlations for UCS and static Young's Modulus (Najibi et al. 2015)

These correlations have been found to sometimes fit lab test data but often do a poor job. It is recommended to calibrate them further to acquired lab test data if available to increase accuracy. Figure 8 shows some comparisons of correlations to test data conducted on various limestone samples from Iran where the different quality of correlations can be seen.

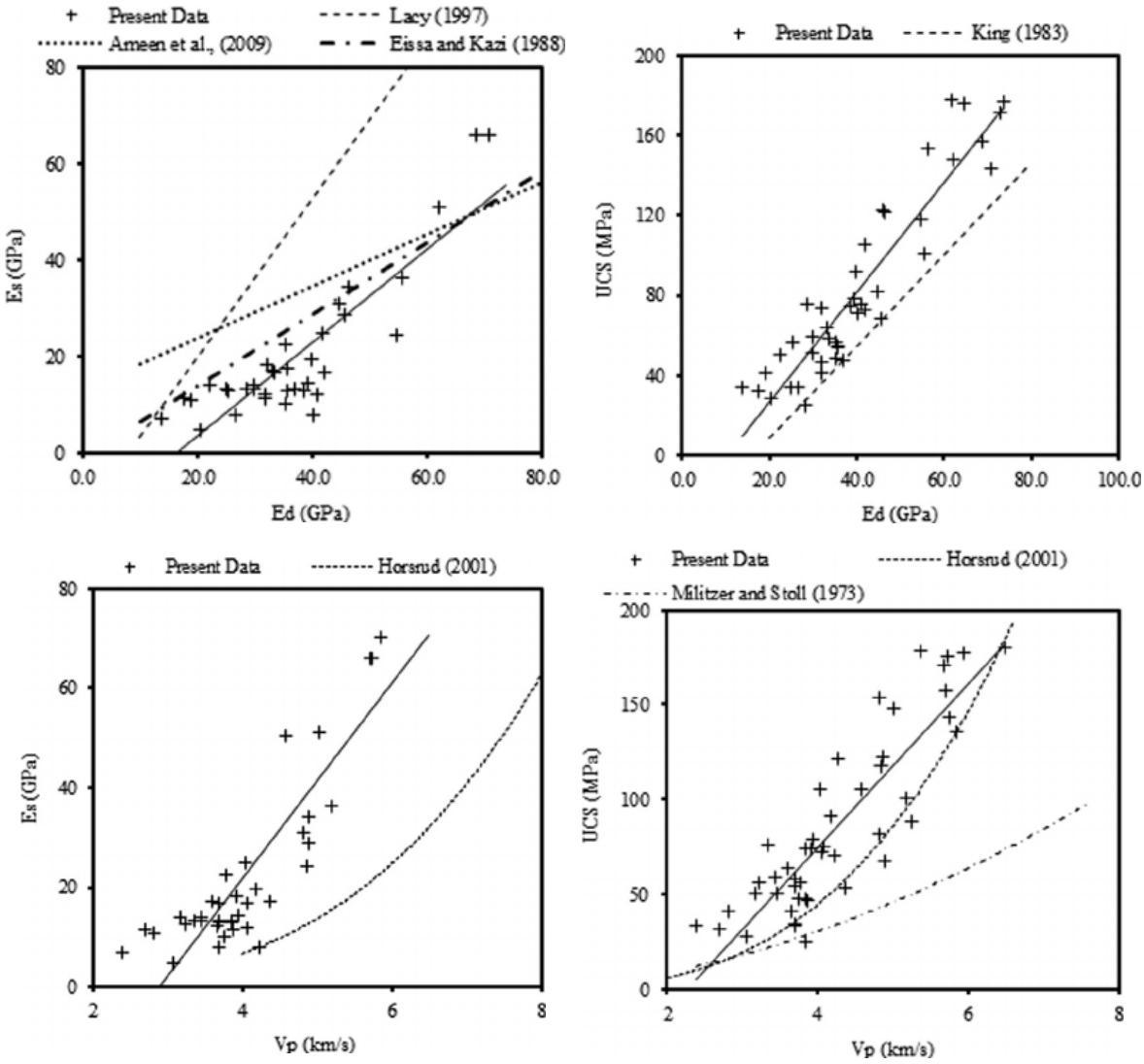

Figure 8: Comparison of various published correlations to test data (Najibi et al. 2015)

2.3 Rock Strength Parameters

The unconfined compressive strength (UCS) and angle of internal friction (φ) of sedimentary rocks are key parameters needed to address a range of geomechanical problems ranging from limiting wellbore instabilities during drilling, to assessing sanding potential and quantitatively constraining stress magnitudes using observations of wellbore failure.

Laboratory-based UCS and φ are typically determined through triaxial tests on cylindrical samples that are obtained from depths of interest. In practice, however, many geomechanical problems in reservoirs must be addressed when core samples are unavailable for laboratory testing. Core samples of overburden formations are in fact almost never available for testing. Many wellbore instability problems are encountered

in overburden zones. As a practical approach to these problems, a number of empirical relations have been proposed that relate rock strength to parameters measurable with geophysical well logs. Using such relations is often the only way to estimate strength in many situations because cores for laboratory tests are not available. The basis for these relations is the fact that many of the same factors that affect rock strength also affect other physical properties such as velocity, elastic moduli and porosity.

In many cases, such relationships have been suggested for sedimentary rocks mainly because the strength information is greatly demanded in reservoirs for drilling and maintenance of wellbores. In general, a strength–physical property relationship for a specific rock formation is developed based on calibration through laboratory tests on rock cores from the given field. If there are no core samples available for calibration, the next best thing would be to use empirical strength relations based on measurable physical properties. Because there are multiple choices of strength models for various rock types in different geological settings, it is necessary to understand the characteristics of the models and their range of applicability prior to utilizing them. (Chang et al. 2006)

Figure 8 and Table 3 also show a few correlations for the UCS. It is easy to see how some correlations are off and some a rather good approximation. The most accurate correlation in that data set was King's (1983) to the dynamic Young's Modulus E_{dyn} . Table 4 shows more developed correlations for the UCS. As with the elastic properties, the correlations usually need to be calibrated with test data from the formation to achieve satisfactory accuracy.

The correlations in Table 4 have been applied to published rock data from many different authors by *Chang, C et al.* (Chang et al. 2006) to investigate their quality and applicability. For example, Figure 9 shows the difference between calculated UCS and measured UCS for shale.

Lithology, Location	Equation for UCS	Reference
Sandstone, Thuringia, Germany	$0.035\ V_p - 31.5$	Freyburg (1972)
Sandstone, Bowen Basin, Australia	$1200\exp(-0.036\ \Delta t)$	McNally (1987)
Sandstone, Gulf Coast	$1.4138 \times 10^7\ \Delta t^{-3}$	McNally (1987)
Sandstone, Gulf Coast	$3.3 \times 10^{-20}\rho^2 v_p^4(\frac{1+\nu}{1-\nu})^2(1-2\nu)(1+0.78v_{clay})$	Fjaer et al (1992)
Sandstone, Cook Inlet, Alaska	$1.745 \times 10^{-9}\rho v_p^2 - 21$	Moos et al. (1999)
Sandstone, Australia	$42.1\exp(1.9\ \times 10^{-11}\rho v_p^2)$	Moos et al. (1999)
Sandstone, Gulf of Mexico	$3.87\exp(1.14\ \times 10^{-10}\rho v_p^2)$	Moos et al. (1999)
Sandstone	$46.2\exp(0.027\ E)$	Moos et al. (1999)
Sandstone, worldwide	$2.28 + 4.1089\ E$	Bradford et al. (1998)
Sandstone, worldwide sedementary basins	$254\ (1 - 2.7\Phi)^2$	Vernik et al (1993)
Sandstone	$277\exp(-10\Phi)$	Vernik et al (1993)
Shale, North Sea	$0.77\ (304.8/\Delta t)^{2.93}$	Horsrud (2001)
Shale, Gulf of Mexico	$0.43\ (304.8/\Delta t)^{3.2}$	Horsrud (2001)
Shale, worldwide	$1.35\ (304.8/\Delta t)^{2.6}$	Horsrud (2001)
Shale, Gulf of Mexico	$0.5\ (304.8/\Delta t)^3$	Horsrud (2001)
Shale, North Sea	$10\ (304.8/\Delta t - 1)$	Lal (1999)
Shale, North Sea	$7.97\ E^{0.91}$	Horsrud (2001)
Shale	$7.22\ E^{0.712}$	Horsrud (2001)
Shale	$1.001\Phi^{-1.143}$	Lashkaripour and Dusseault (1993)
Shale, North Sea	$2.922\Phi^{-0.96}$	Horsrud (2001)
Shale	$0.286\Phi^{-1.762}$	Horsrud (2001)
Limestone and Dolomite	$(7682/\Delta t)^{1.82}/145$	Militzer and Stoll (1973)
Limestone and Dolomite	$10\text{^}(2.44 + 109.14/\Delta t)/145$	Golubev and Rabinovich (1976)
Limestone	$13.8\ E^{0.51}$	Golubev and Rabinovich (1976)
Dolomite	$25.1\ E^{0.34}$	Golubev and Rabinovich (1976)
Limestone and Dolomite, Russia	$276(1 - 3\Phi)^2$	Rzhevsky and Novick (1971)
Limestone and Dolomite, Middle East	$143.8\exp(-6.95\Phi)$	Rzhevsky and Novick (1971)
Limestone and Dolomite	$135.9\exp(-4.8\Phi)$	Rzhevsky and Novick (1971)

Table 4: Various published correlations to receive the UCS (Chang et al. 2006)

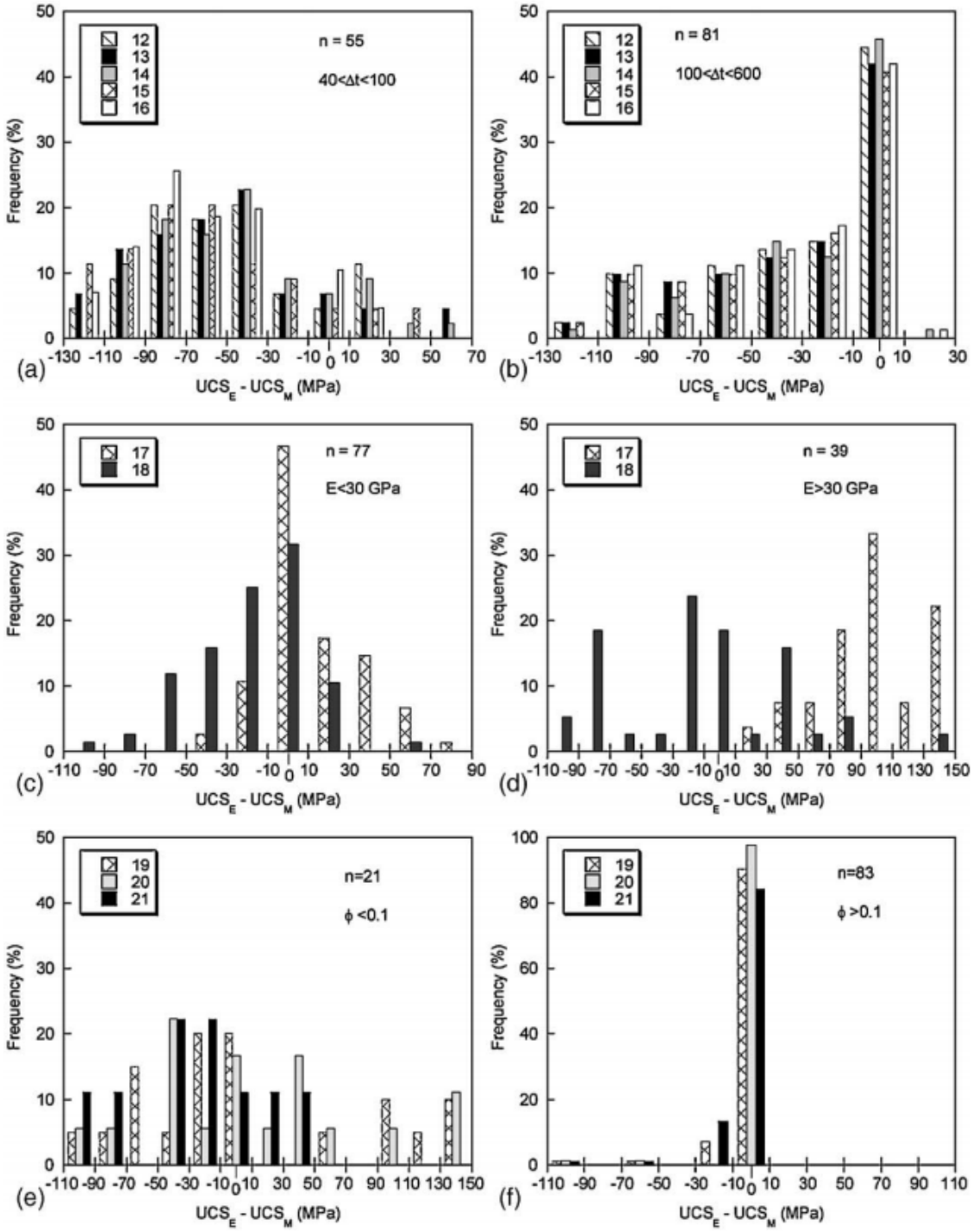

Figure 9: Difference between calculated and measured UCS for shale (Chang et al. 2006)

It can be generally said for all correlations for rock strength and elastic parameters that they match reasonably well for the subset of data used when they were developed. The applicability to other data is very different and was revealed in that study to be poor for many correlations. For example, a correlation created for North Sea shale will fit

North Sea shale reasonably well but not necessarily any other shale. This effect can be seen when comparing chart **b)** to chart **a)** in Figure 9**.** The used correlations have been developed for rather high porosity thus slow shale and because of that better fit the high slowness data in **b)** than the lower porosity, low slowness data in **a).** The fit for the high porosity data is reasonable and tends to underestimate the UCS which makes the calculations safer. Similarly, the fit for the lower Young's Modulus, higher porosity data in **c)** is better than for low porosity rocks in **d)** but less accurate than the correlations used before that utilize slowness data. The best fit is achieved with the correlations using porosity data when applied to high porosity shale (> 10%), similar to the shale used when they were developed. This is seen in the charts **f)** vs **e)**. This means that it is very important to think about the subset of data used to acquire the correlations and apply them only to similar data. Even higher accuracy can be achieved when lab data is available and the chosen correlation is further calibrated using the lab data.

The angle of internal friction φ is a measure of the ability of a rock to withstand shear stress. It is the angle between the normal force and resultant force during failure due to a shearing stress. The tangent (shear / normal) is the coefficient of sliding friction. These parameters can be determined with laboratory tests. The angle of internal friction along with the UCS is required for many commonly used failure criterions to estimate the strength of the rock at depth. As with the previously discussed parameters, it is often estimated using correlations to log data, because lab data is not available. Table 5 shows two published equations for the internal friction angle.

Lithology	Equation for internal friction angle	Reference
Shale	$\sin^{-1}((v_p - 1000)/(v_p + 1000))$	Lal (1999)
Sandstone	$57.8 - 105\Phi$	Weingarten and Perkins (1995)

Table 5: Equations for internal friction angle (Chang et al. 2006)

Figure 10 shows how these correlations estimate the angle of internal friction compared to different published test results.

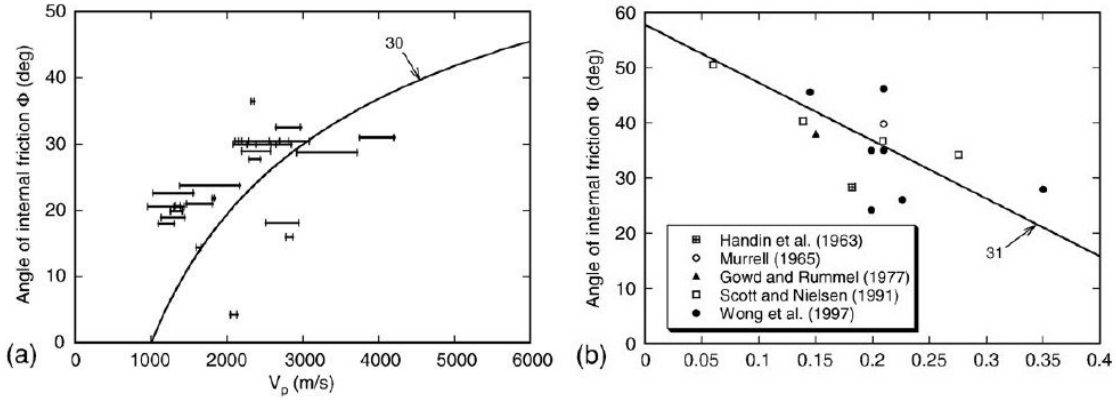

Figure 10: Internal friction angle correlations compared to test data (Chang et al. 2006)

The data suggests that the correlation for compressional wave velocity tends to underestimate the internal friction angle, especially for velocities below 1500 m/s (porous, low density rock). However, the uncertainty is not as significant as for the estimation of the UCS. Additionally, the effect of the internal friction angle on the rock strength estimation using failure criteria is not as significant as the effect of the UCS. So it can be concluded that the given correlations deliver workable results. Further calibration with test data will lead to better results.

2.4 Pore Pressure

The only accurate way to determine pore pressure is by direct measurement. These measurements are typically done in reservoirs when fluid samples are taken using a wireline formation testing tool. Advanced technology allows for measurement of in-situ pore pressure while drilling. Using these tools on shale to receive proper data is almost impossible, because their permeability and porosity are so low. Often the only available data before drilling is seismic data which can be used to get predrill estimates. These estimates are further improved with data acquired when drilling.

The pore pressure is an important component in a Mechanical Earth Model and critical to the calculation of horizontal stresses, wellbore stability analysis and other geomechanics applications. Sonic and resistivity logs can be used to identify pore pressure trends which can be used to estimate the pore pressure. The estimated pore pressure needs to be calibrated by pore pressure data. The following methods are only intended for use with shales.

2.4.1 Eaton's Method

Eaton's method is a very popular method that has been originally developed for the Gulf of Mexico for undercompacted, overpressured shales and needs to be calibrated accordingly. It relies on Terzaghi's equation of 1948:

$$\sigma_{effective} = \sigma_{overburden} - P_{pore} \tag{8}$$

Which is reorganized to:

$$P_{pore} = \sigma_{overburden} - \sigma_{effective} \tag{9}$$

Terzaghi's principle states that if a rock is subjected to a stress, in this case vertical, the stress is opposed by the fluid pressure of pores in the rock, which is the pore pressure. This means that to receive the effective stress acting on the rock, the pore pressure needs to be deducted.

This relationship is displayed in Figure 11. The effective stress lies between the pore pressure and the overburden stress.

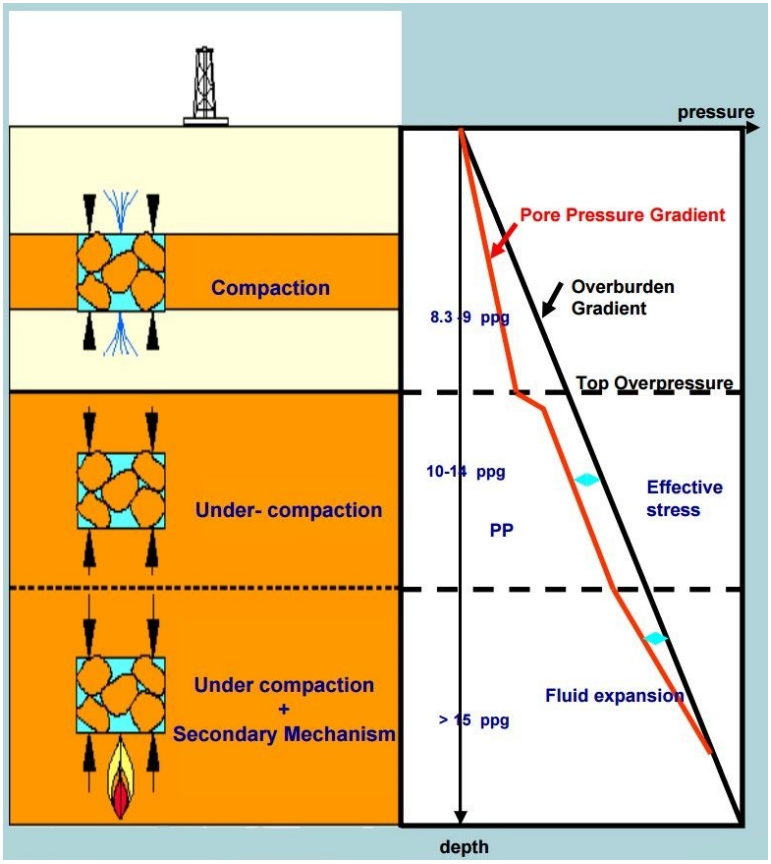

Figure 11: Overburden and pore pressure gradients and effective stress (Formento 2004)

The effective stress term is then correlated to log data such as resistivity or wave velocity or slowness to receive the commonly used Eaton's relationship in Equation 10 and Equation 11.

$$P_{pore} = OBG - \left(OBG - G_{hyd}\right)\left(\frac{v_{log}}{v_{normal}}\right)^{n} \tag{10}$$

$$P_{pore} = OBG - \left(OBG - G_{hyd}\right)\left(\frac{R_{log}}{R_{normal}}\right)^{n} \tag{11}$$

Where:

OBG is the overburden gradient

G_{hyd} is the gradient of hydrostatic pressure

v_{log} and R_{log} are the velocity and resistivity values measured by the log

v_{normal} and R_{normal} are the velocity and resistivity values according to the normal compaction trend

n is the exponent that can be adjusted during calibration. Commonly n is 1.2 when using resistivity and 3.0 when using velocity or slowness.

The pore pressure here is primarily established based on the divergence of the log measurements from the normal compaction trend. This trend is an estimation of how the velocity or resistivity would have been if the pore pressure would have been normal, that means hydrostatic, hence the hydrostatic pressure gradient presented in the equations. It represents the optimum fitted linear trend of the measured data in the low permeable beds. Setting the normal compaction trend correctly is crucial to the outcome of the model. It can be set by linear extrapolating the data in the Transit Zone (TZ) between the depth where the compaction disequilibrium dewatering (CDD) process starts and the depth where the dewatering is seized (fluid retention depth FRD or top of geopressure TOG). This is also called the hydrodynamic zone, while the zone below is the confined or geopressured zone. Above the transit zone is the unconfined zone. In the Transit Zone the formation water is expelled gradually from sediments due to pressure gradient drop from deeper to shallower depth and consequently velocity, density and resistivity increase downward concurrent with the rate of the dewatering process. Below, the water is not capable of escaping. The remaining fluid must support the weight of the overburden which causes the abnormally high pore pressure. The porosity will decrease less rapidly with depth than

expected so frequently higher than expected porosities can be found in over pressured zones.

The relationship is between CDD, TOG and NCT is shown in Figure 12.

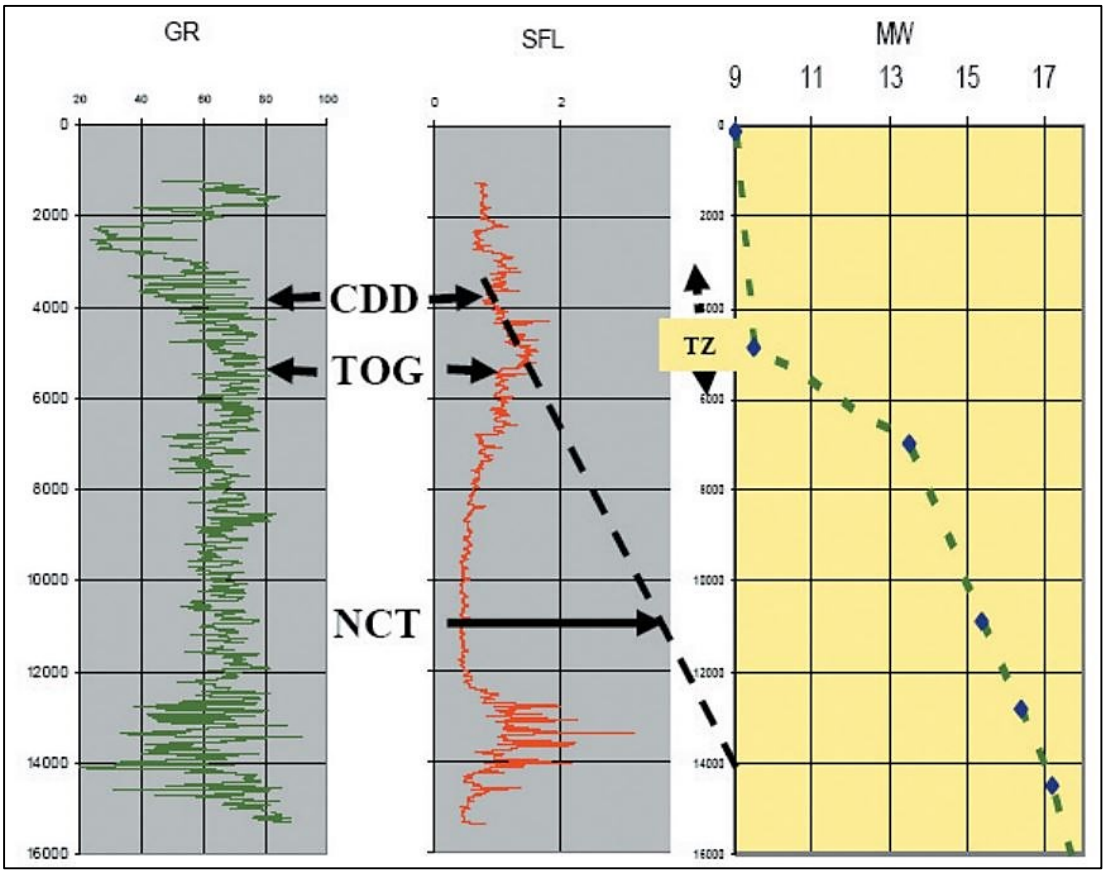

Figure 12: NCT created from Transit Zone data (Shaker 2007)

The major problem with trend-line methods such as Eaton's method is that the user must pick the correct normal compaction trend which is sometimes hard to define because of a lack of data. For example, when the NCT is set over an interval with overpressure, the method will give too low pore pressures resulting in severe risks for drilling.

Zhang (2011) has published non-linear depth dependent equations for the normal values in Eaton's method in case the NCT could not have been determined:

$$R_n = R_0\, e^{bZ} \tag{12}$$

$$v_n = v_0\, e^{bZ} \tag{13}$$

Where R_0 and v_0 are the resistivity and velocity values at the mudline, R_n and v_n the resistivity and velocity values for the normal compaction trend, b is a constant and Z the depth. (Zhang 2013)

2.4.2 Bowers Method

Bowers (1995) effective stress method calculates the effective stresses from measured pore pressure data and overburden stresses and analyzed the corresponded sonic velocities from well logging data in the Gulf of Mexico slope (Zhang 2013). He proposed that the sonic velocity and effective stress have a power relationship as follows:

$$v_p = v_{ml} + A\sigma_e^B \tag{14}$$

Where $v_p$is the compressional wave velocity at a given depth, $v_{ml}$is the compressional wave velocity at the mudline, σ_e is the vertical effective stress, A and B are constants for calibration. Using the relationship $\sigma_e = \sigma_v - p_p$ the pore pressure is obtained as:

$$p_p = \sigma_v - \left(\frac{v_p - v_{ml}}{A}\right)^{\frac{1}{B}} \tag{15}$$

The effective stress and compressional velocity do not follow the loading curve if formation uplift or unloading occurs, and a higher than the velocity in the loading curve appears at the same effective stress. Bowers (1995) proposed the following empirical relation to account for unloading effect:

$$v_p = v_{ml} + A\left(\sigma_{max}\left(\frac{\sigma_e}{\sigma_{max}}\right)^{\frac{1}{U}}\right)^B \tag{16}$$

With parameters as before and U being a constant and σ_{max} the estimated effective stress at the onset unloading.

σ_{max} can be derived as follows:

$$\sigma_{max} = \left(\frac{v_{max} - v_{ml}}{A}\right)^{\frac{1}{B}} \tag{17}$$

Where v_{max} is the estimated velocity at the onset unloading. If the lithology does not change majorly v_{max} is usually set equal to the velocity at the start of the velocity reversal.

Rearranging again for the pore pressure yields:

$$p_{ulo} = \sigma_v - \left(\frac{v_p - v_{ml}}{A}\right)^{\frac{U}{B}} (\sigma_{max})^{1-U} \tag{18}$$

Where p_{ulo} is the pore pressure in the unloading case.

The method is applicable in many basins e.g. Gulf of Mexico but overestimates the pore pressure when the shallow formation is poorly consolidated or unconsolidated because the velocities there are very small. (Zhang 2013)

A couple more methods have been published but they are not used as often as the methods explained above.

2.4.3 Complications

The required calibration points can be measured data or based on instability events encountered while drilling. Such events include the occurrence of kicks (usually because the mud weight is lower than the equivalent density of the pore pressure), loss of circulation (usually because of natural fractures or drilling induced fractures because of too high mud weight) or observations of instabilities in shales.

Furthermore, it is assumed that the rock obeys a single, monotonic, compaction-induced linear trend and that no other effects are occurring. In reality, cementation can be increased by active chemical processes leading to increased stiffness (E) which results in higher velocities masking high pore pressure. The assumed normal pressure would be overestimated in that case and overpressure not detected. Increased temperature transforms the shale mineral, for example a water bearing smectite to a relatively water-free and denser illite. This occurs over a range of temperatures near 110°C varying with fluid chemistry. The depth where these temperatures are reached varies from basin to basin. This effect also causes the stiffness to rise and normal pressure to be overestimated.

The type of pore fluid can have a significant effect on pore pressure predictions as the resistivity and velocity of the rock are affected by the properties of the pore fluid. For example, a salinity increase leads to higher conductivity and lower resistivity which can be misinterpreted as an increase in pore pressure. The fluid resistivity also decreases with increasing temperature. Hydrocarbons have a higher resistivity than

brines so increases in pore pressure could get masked. The compressional wave velocity will decrease because hydrocarbons are less dense than brines but shear wave velocity will increase. The resistivity and compressional velocity are affected in opposite ways by a change to hydrocarbons so using both measurements simultaneously can sometimes identify such zones. Salinity changes are more difficult to identify. (Lake, Fanchi 2006-2007)

2.5 Horizontal Stresses

The forces in the Earth are quantified using stress tensors. The components of these tensors are tractions acting perpendicular or parallel to three planes that are orthogonal to each other. The normals to these three planes form a Cartesian coordinate system with axes x_1, x_2 and x_3 so every point in space can be identified. Of the nine tensor components three are normal stresses acting perpendicular to a plane (S_{11}, S_{22}, S_{33}) and the other six are shear stresses acting along a plane. These relationships are illustrated in Figure 13.

There is a particular stress axes orientation at any point in space for which all shear stress components are zero. These directions are referred to as the „principal stress directions “. The three stresses along these directions are called principal stresses S_1, S_2 and S_3 where S_1 is the greatest principal stress, S_2 the intermediate principal stress and S_3 the least principal stress. The shear stresses are zero.

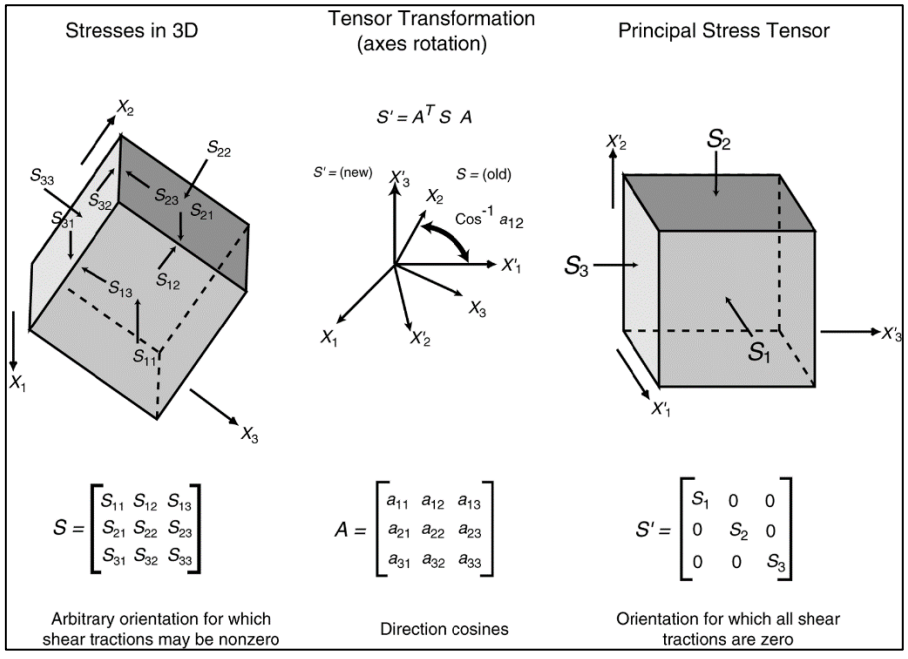

Figure 13: Stress tensor definitions, transformation and principal stress tensor (Lake, Fanchi 2006-2007)

In most parts of the world at depths relevant for drilling the vertical stress or overburden stress is a principal stress. This means that the other principal stresses must act in a horizontal direction. The larger of them is called greatest or maximum horizontal stress S_H and the smaller one minimum or least horizontal stress S_h. The largest components of the stress field, gravitational loading and plate driving stresses, act over large areas so the principal stress orientations and magnitudes in the crust are very uniform. The stress orientation around the world can be seen on the World Stress Map where a lot of data has been compiled. Local perturbations occur and have to be considered for correct geomechanical analysis. For example, while the stress orientation within a field can be uniform, it can be different in other fields in the same basin.

Magnitude wise, the vertical stress could be the greatest, intermediate or least principal stress. Which case is present depends on the type of faulting or faulting regime. In a normal faulting regime, the vertical stress is the greatest principal stress. When the vertical stress is the intermediate principal stress a strike-slip regime is present. If it is the least principal stress the regime is called reverse. The horizontal stresses at a given depth will be smallest in a normal faulting regime, larger in a strike-slip regime, and greatest in a reverse faulting regime. In general, vertical wells will be progressively less stable as the regime changes from normal to strike-slip to reverse, and consequently will require higher mud weights to drill. Figure 14 illustrates the different faulting regimes and corresponding principal stresses.

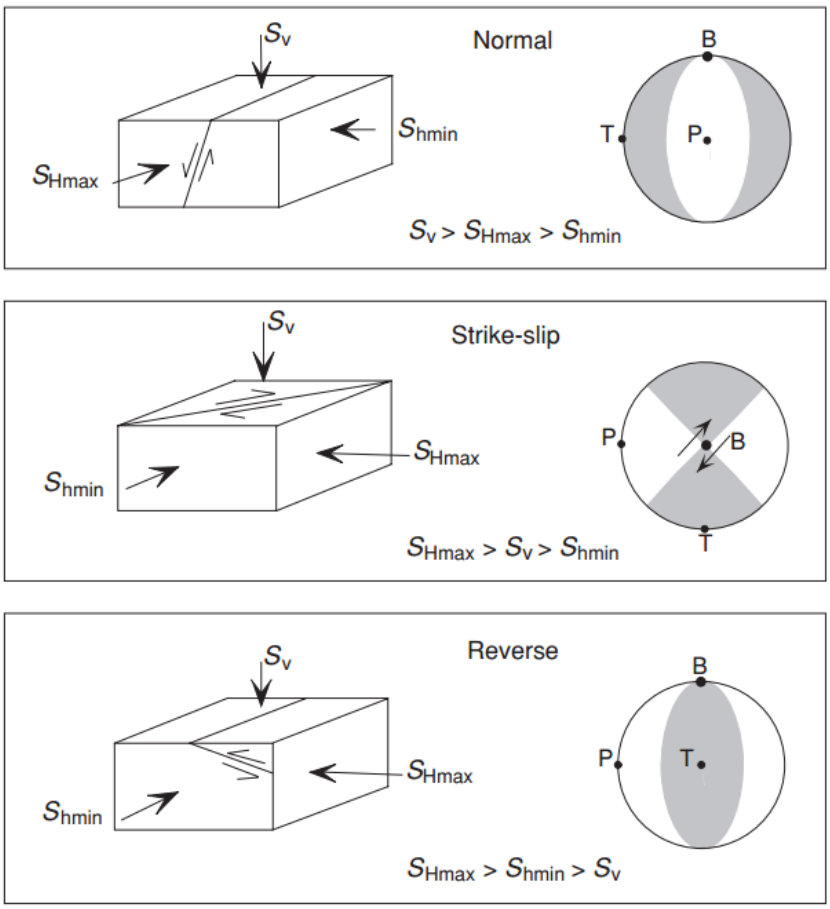

Figure 14: The three faulting regimes and their principal stress magnitudes (Lake, Fanchi 2006-2007)

Usually a Normal faulting regime is encountered. In a Strike-Slip faulting regime the maximum horizontal stress has become larger than the vertical stress but the minimum horizontal stress remains below it. For this to happen, there has to be an additional horizontal stress acting, most likely due to tectonic movement or moving salts. If the horizontal input is so large that the vertical stress is the smallest principal stress, a Reverse faulting regime is present. The main driving mechanism for this regime is compression.

2.5.1 Minimum Horizontal Stress

The minimum horizontal stress can be directly measured using extended leakoff tests (XLOT) or minifrac tests. Fluid is pumped into the wellbore to pressurize an interval of exposed rock until it fractures and the fracture is propagated away from the well by continued pumping at a constant rate. To minimize the energy required for

propagation the fracture will grow away in an orientation that is perpendicular to the far-field least principal stress. Therefore, the pressure required to propagate the fracture will be equal to or higher than the minimum horizontal stress. Fracture propagation will stop when leakoff of fluid from the fracture and wellbore and into the formation occurs faster than the fluid is replaced by pumping. If pumping stops entirely, fluid leakoff will continue from the walls of the fracture until it closes, severing its connection to the wellbore. The fracture will close as soon as the pressure drops below the stress acting normal to the fracture (which is the minimum horizontal stress). The change in flow regime after pumping stops, from one in which the fracture contributes to fluid losses to one in which all fluid losses occur through the walls of the well, can be seen in pressure-time and other plots of pressure after shut-in (pressure vs. square root of time, Figure 15). The minimum horizontal stress is taken to be the pressure at which the transition in flow regime occurs (= fracture closure pressure).

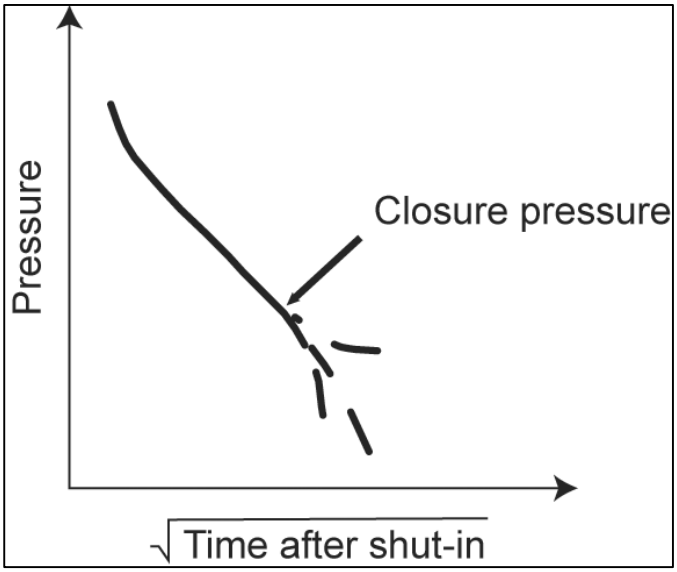

Figure 15: Pressure vs square root of time, closure pressure equals the minimum horizontal stress (Lake, Fanchi 2006-2007)

An extended leak-off test will damage the formation and can cause fluid loss during drilling so XLOT are barely performed, often not even regular leak-off tests (LOT) are done but just formation integrity tests (FIT) which only give information about the maximum used pressure while pumping. They are done to prove the design limit of the next hole section and will not initiate fractures. That means that the minimum horizontal stress is always larger than the used pressure. Figure 16 shows an idealized XLOT. The Leak-Off Pressure (LOP) would be used for the minimum horizontal stress. It is also acquired during a normal LOT. In an XLOT the Fracture Closure Pressure (FCP) is also acquired which is lower because tensile strength was lost.

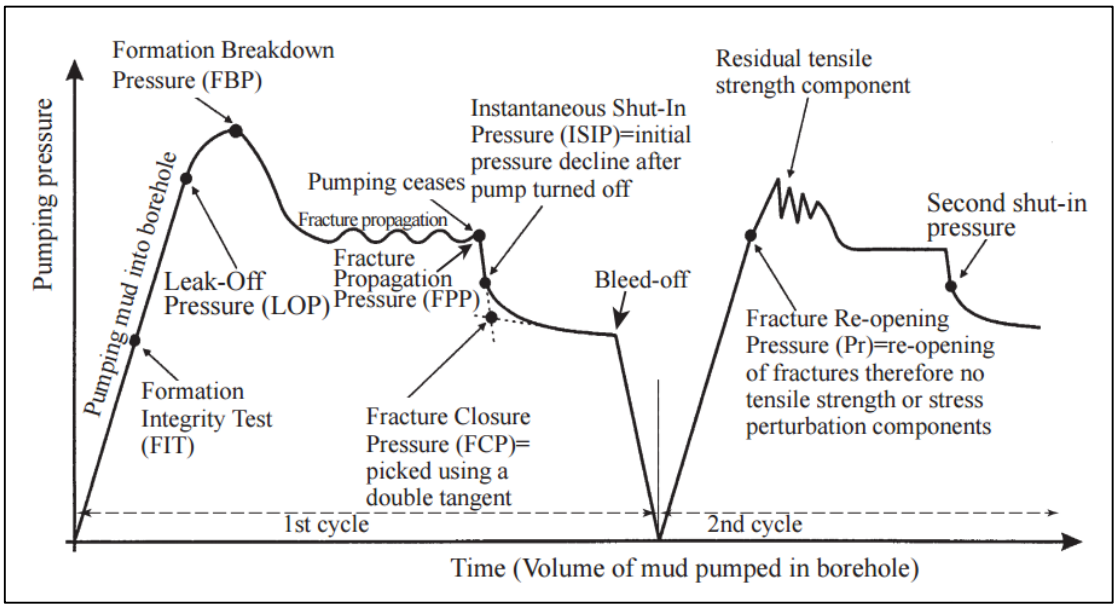

Figure 16: Idealized relationship between pumping pressure and time or volume during an XLOT (Lin et al. 2008)

The gathered data from direct measurements and instability events is used to calibrate the calculated minimum horizontal stress. For the conventional method of calculating the minimum horizontal stress the poroelastic equation is used. Assuming that one stress is vertical and two are horizontal, a uniaxially from a horizontal direction compressed rock will have its total strain value in that direction described as follows:

$$\varepsilon_{H1} = \frac{\sigma_{H1}}{E} - \frac{\nu\sigma_{H2}}{E} - \frac{\nu\sigma_V}{E} \tag{19}$$

Assuming that the strain equals zero and the horizontal stresses are equal, the following is acquired:

$$\sigma_h = \frac{\nu}{1-\nu}\,\sigma_V \tag{20}$$

This calculation indicates the likely values of the natural in-situ stress components based on elasticity theory applied to isotropic rock.

The total stress (principal) is equal to matrix stress (σ_h and σ_V) plus pore pressure. Considering this, the following equation is aquired:

$$S_h = \frac{\nu}{1-\nu}\,(S_V - P) + P \tag{21}$$

Considering that not the whole total stress and pressure changes get converted to effective stress changes, Biot's constant is introduced into the equation. Furthermore, the tectonic stress is added in order to be able to shift the values appropriately. It is usually used as a calibration factor. The final formula is then acquired as:

$$S_h = \frac{\nu}{1-\nu}\,(S_V - \propto P) + \propto P + \sigma_{tect} \tag{22}$$

Where S_h is the minimum horizontal stress, ν the Poisson's ratio, S_V the vertical stress or overburden stress, $\propto$ Biot's constant, P the pore pressure and σ_{tect} the tectonic stress.

Biot's constant is a factor that helps to account for the deformation of a poroelastic material as the pore pressure changes. It illustrates how compressible the dry matrix frame is with respect to the solid material composing the matrix of the rock. It measures the ratio of fluid volume squeezed out to the volume change of the rock if it is compressed while allowing fluid to escape. It is a function of several parameters like porosity, permeability, grain sorting and pressures. It can be calculated as:

$$\propto = 1 - \frac{K_S}{K_{min}} \tag{23}$$

Where K_S is the bulk modulus of the rock and can be calculated from log data as discussed in Chapter 2.2 or as follows:

$$K_S = \frac{E}{3(1-2\nu)} \tag{24}$$

Where E is the Young's modulus and ν the Poisson's ratio. They can be aquired using log data. K_{min} is the bulk modulus of the mineral or grain of the rock itself.

The calculated bulk modulus must be correlated to the static bulk modulus as discussed before, for example using a linear relationship with one correlation factor. Data points from lab measurements have to be used for this. The grain bulk modulus can be acquired from XRD (X-Ray Powder Diffraction) analysis multiplying the weight fraction of each mineral with its bulk modulus and summing it up. Table 6 shows grain bulk moduli of some common minerals.

Mineral	Kmin (GPa)
Quartz	37
K feldspar	37.5
Plagioclase	75.6
Calcite	70
ankerite dolomite	80
dolomite	80
pyrite	143
Fluorapatite	86.5
illite-smectite	23
illite-mica	23
Kaoline	1.5
Chlorite	1.5

Table 6: Grain bulk moduli of common minerals (Song 2012)

Finally, Biot's constant can be calculated. It is a very important and influential factor. Having Biot's constant the minimum horizontal stress can be calculated by setting the tectonic stress as calibration factor with data from measurements or instability events. Other methods have been published but the conventional method is the most popular method.

2.5.2 Maximum Horizontal Stress

Unlike the minimum horizontal stress, the maximum horizontal stress cannot be measured directly and is widely considered as the most difficult component of the stress tensor. It requires knowledge of pore pressure, calibrated rock strength, vertical stress and minimum horizontal stress data. The maximum horizontal stress can be estimated from image logs, frictional limit to stress and DIF (drilling induced fractures) data, micro frac data and caliper data.

Similar to the minimum horizontal stress, the poroelastic equation can be used as below. The only difference is the magnitude of the tectonic stress term, which is higher for the maximum than minimum horizontal stress.

$$S_H = \frac{\nu}{1-\nu}\left(S_V - \propto P\right) + \propto P + \sigma_{tect} \tag{25}$$

The tectonic stress term is used as calibration factor by using the breakdown pressure from micro frac data and adjusting it for breakouts seen in caliper and image logs. The process for determining the stress magnitudes is illustrated in Figure 17.

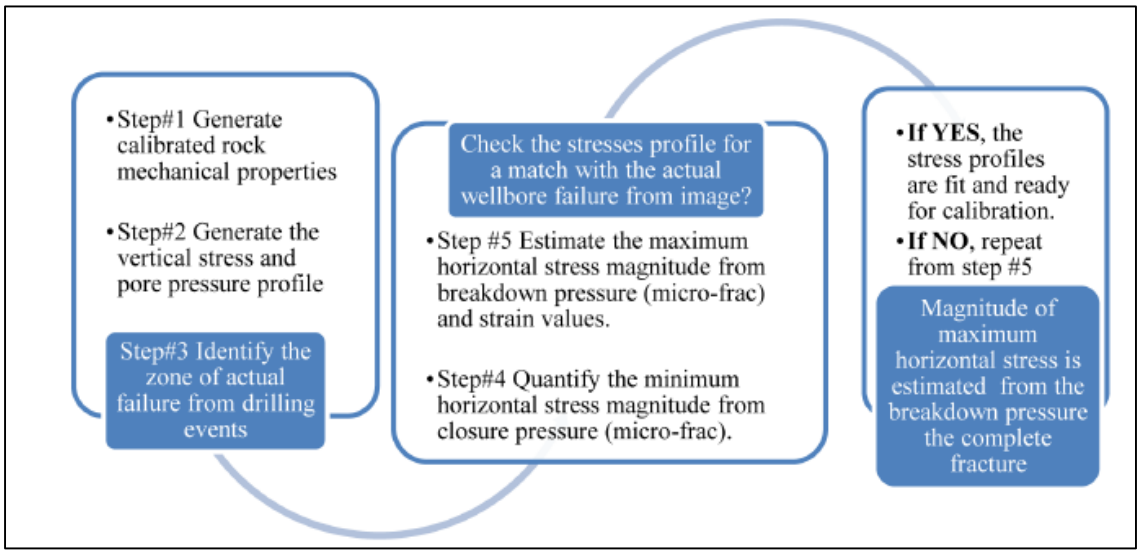

Figure 17: Determination of in-situ stress magnitudes (Haidary et al. 2015)

Another way to use the images of breakouts is to use the observed breakout width or angle as parameter in the Kirsch equations. After inputting the breakout width and pressure data, the equations can be rearranged to calculate maximum and minimum horizontal stress. This is shown in Figure 18.

Not having the required image, log or test data available means that an estimation of the maximum horizontal stress is not possible. Data like image logs is rarely measured in practice so often it can't be estimated properly. In these cases, the maximum horizontal stress is often set to be equal to the minimum horizontal stress. Failure would occur when reaching the minimum horizontal already, so the upper boundary for the mud weight is never set by the maximum horizontal stress anyway.

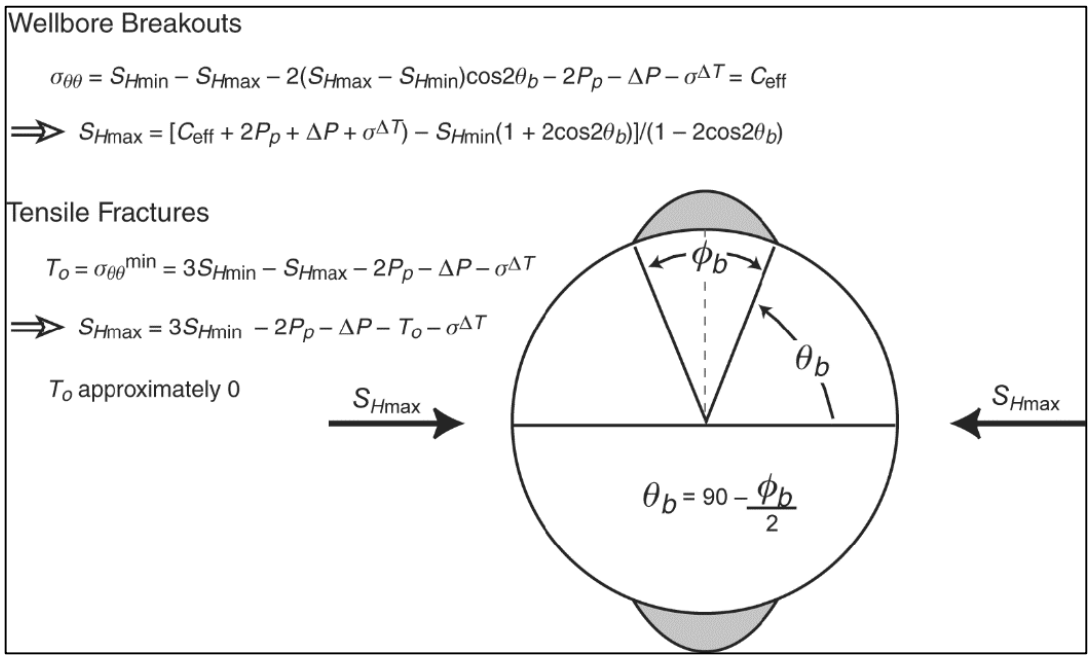

Figure 18: Schematic diagram of a breakout and Kirsch equations (Lake, Fanchi 2006-2007)

As seen in Figure 18 breakouts are not the only form of failure, tensile fractures can appear when the difference between the maximum and minimum horizontal stress is significant and the hoop stress (tangential stress) in the wellbore is a tensile strass and not compressive anymore. This can be the case in a strike-slip regime because the largest principal stress will be S_{Hmax} while the least principal stress will be S_{Hmin} thus the difference is maximal.

To detect drilling-induced tensile fractures image logs are required as they do not propagate far. They stop when the wellbore pressure is equal to the effective minimum hoop stress. The fractures will not have a noticeable influence on the drilling process because of their little size. Figure 19 shows tensile fractures and breakouts in image logs. It has to be noted that image logs are not run frequently so that data is rather rare making modelling S_{Hmax} difficult and introduces high risk. Furthermore, in the literature the use of microfrac data for calibration is challenged by some authors.

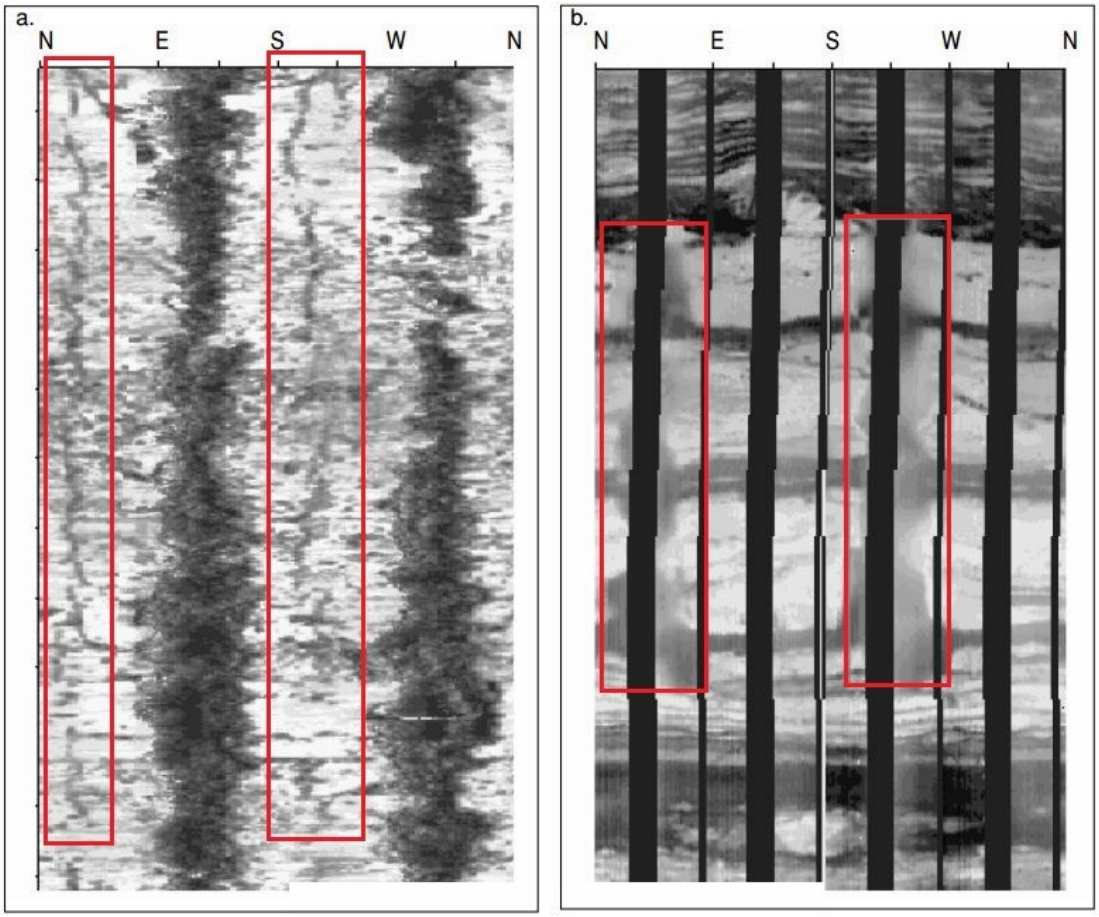

Figure 19: a) Tensile fractures marked in red on Ultrasonic Televiewer image. b) Breakouts marked in red on electrical image (Zoback 2010)

2.5.3 Stress Orientation

The minimum and maximum horizontal stress are principal stresses and thus their directions are perpendicular to each other. The direction of the horizontal stresses can be estimated from analysis of borehole breakouts on image logs and caliper data or earthquake focal mechanisms like fault directions. This thesis concentrates on the log data analysis.

Breakouts are ellipsoidal wellbore enlargements caused by stress induced failure. The breakouts form whenever the circumferential stress exceeds the compressive rock strength. The spalling direction of the breakout in a near vertical wellbore parallels the minimum horizontal stress. In a homogeneous stress field, the direction of breakouts is usually consistent from the top to the bottom of the well. Analysis of four arm caliper data reveals the breakout direction which is the direction of the minimum horizontal stress. The maximum horizontal stress direction is perpendicular to that. Figure 20 shows data from a borehole image tool and its conclusion for stress directions.

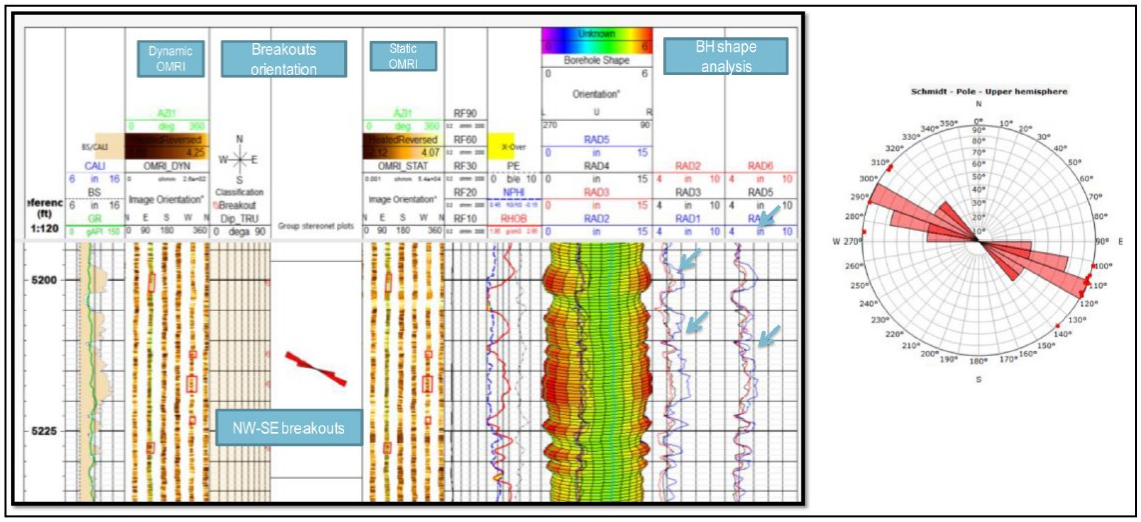

Figure 20: Oil Mud Reservoir Imager (OMRI) tool image showing borehole breakouts and strike orientation towards SE-110 which equals min. horizontal stress direction. Max. horizontal stress is perpendicular, SW-200. (Haidary et al. 2015)

The directions in deviated wellbores depend on the type of faulting regime, deviation angle of the borehole axis from vertical, relative magnitudes of the three principal stresses (min. and max. horizontal stress and vertical stress) and the angle between the horizontal projection of the borehole axis and the direction of the min. horizontal stress. Studies have shown that the influence of well deviation on breakouts in strike slip faulting regime seems insignificant compared with those of normal and thrust faulting regimes. The higher the horizontal differential stress (difference between max. and min. horizontal stress) is the higher the change in breakout direction is. (Adewole, Healy 2013)

Knowing the principal stress directions is important for trajectory planning and hydraulic fracturing and reduces instability.

2.6 Failure Mechanisms

Two types of stress induced failure of rock around the wellbore are encountered during drilling, shear failure and tensile failure. Shear failure is usually caused by low pressure because of a too low mud weight while tensile failure is caused by high pressure because of a too high mud weight. Several models for predicting rock failure and wellbore stability exist. The most commonly used failure criterion is the Mohr Coulomb Criterion to determine shear failure and the maximum tensile stress criteria to determine tensile failure. (Haidary et al. 2015) Other used criteria are the Mogi

Coulomb, Drucker-Prager and Modified Lade criterion. Shear failure leads to borehole collapse and is used as lower boundary for mud weight design while the fracture gradient or min. horizontal stress make the upper boundaries.

Furthermore, the criteria have been studied and benchmarked for a variety of rocks and lithologies to determine their accuracy. A very important difference is that the conventional Mohr-Coulomb criterion is a triaxial criterion meaning that it is applicable to conventional triaxial test data ($\sigma_1 > \sigma_2 = \sigma_3$). A result of this is that the effect of the intermediate principal stress is ignored. The Modified Lade, Mogi-Coulomb and Drucker-Prager criteria are polyaxial criteria that consider the influence of the intermediate principal stress in more sophisticated polyaxial strength tests ($\sigma_1 > \sigma_2 > \sigma_3$). (Colmenares, Zoback 2002)

Comparisons have shown that the Mohr-Coulomb criterion underestimates the rock strength and thus overestimates the required mud weight. The Drucker-Prager criterion does the opposite, it overestimates rock strength and underestimates the required mud weight and is therefore more dangerous. The modified Lade criterion can underestimate or overestimate rock strength. The differences can be large and therefore dangerous when overestimating. The Mogi-Coulomb criterion has been found to be the most accurate criterion for most cases. (Zhang et al. 2010)

To determine which failure criterion fits a specific case best, historical data can be used, if available. The best fitting criterion can then be identified. In the following section equations of popular failure criteria are introduced. They are expressed using the parameters obtained by building a MEM.

2.6.1 Mohr Coulomb

Triaxial, most popular and simple, very conservative

$$\sigma_1 = UCS + q\sigma_3 \tag{26}$$

With

$$q = (1 + \sin(\varphi))/(1 - \sin(\varphi)) \tag{27}$$

Or

$$\tau_{max} = c + \tan(\varphi)\,\sigma_m \tag{28}$$

With

$$c = UCS(1 - sin(\varphi))/(2\cos(\varphi)) \tag{29}$$

Where σ_1 and σ_3 are the largest and least principal stresses, φ is the angle of internal friction, UCS is the unconfined compressive strength, σ_m is the median stress, c is cohesion and τ_{max} the maximum shear stress at which failure will occur. (Al-Ajmi 2012) This makes up the failure envelope. Another popular depiction of the criterion is as follows:

$$\tau^2 = \left(\frac{\sigma_1 - \sigma_3}{2}\right)^2 - \left(\sigma_m - \frac{\sigma_1 + \sigma_3}{2}\right)^2 \tag{30}$$

This means that the shear stress is a circle, the so called Mohr circle with the center at ($\frac{\sigma_1+\sigma_3}{2}$, 0) and radius $\frac{\sigma_1+\sigma_3}{2}$. Failuere occurs at the intersection of envelope and circle. Therefore, a circle constructed by the wellbore stresses leads to failure if it intersects the failure envelope. Figure 21 displays the failure envelope and a Mohr circle.

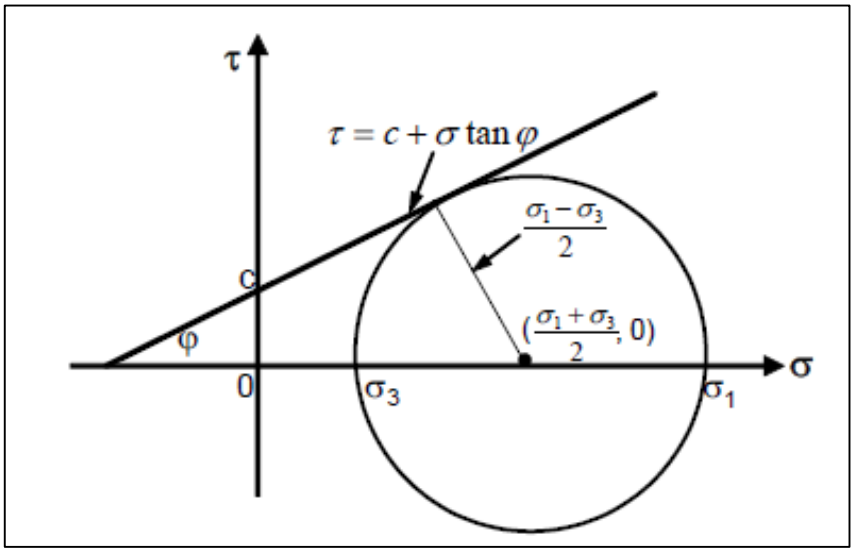

Figure 21: Mohr circle and its failure envelope (Peng, Zhang 2007)

Tensile failure occurs when the stress becomes negative/tensile and exceed a certain limit. This limit is called tensile strength. Often the tensile strength of rock is set to zero or a very low fraction of the UCS but it can be estimated using the Mohr Coulomb criterion. To receive the tensile strength, equation 29 has been input into equation 28 and the shear stress set to zero, as the point where the straight failure line intersects the x-axis is the tensile strength.

$$\tau_0 = -\frac{UCS\big(1 - sin(\varphi)\big)}{2\cos(\varphi)\tan(\varphi)} \tag{31}$$

2.6.2 Drucker Prager

Poly-axial, takes intermediate principal stress into account, overestimates rock strength

$$\tau_{oct} = k \ + m\, \sigma_{oct} \tag{32}$$

Where τ_{oct} is the octahedral shear stress defined by

$$\tau_{oct} = \frac{1}{3}\sqrt{(\sigma_1 - \sigma_2)^2 + (\sigma_2 - \sigma_3)^2 + (\sigma_3 - \sigma_1)^2} \tag{33}$$

and σ_{oct} is the octahedral normal stress defined by

$$\sigma_{oct} = \frac{\sigma_1 + \sigma_2 + \sigma_3}{3} \tag{34}$$

With k and m being material constants that have to be estimated from the intercept and slope of the failure envelope plotted in the τ_{oct}-σ_{oct} plane. The data for this has to be acquired from polyaxial tests.

2.6.3 Modified Lade

Poly-axial, takes intermediate principal stress into account, more conservative than Mohr-Coulomb, less than Drucker-Prager

$$\frac{(I_1)^3}{I_3} = 27 + \ \eta \tag{35}$$

Where

$$I_1 = (\sigma_1' + S) + (\sigma_2' + S) + (\sigma_3' + S) \tag{36}$$

$$I_3 = (\sigma_1' + S)(\sigma_2' + S)(\sigma_3' + S) \tag{37}$$

$$S = \frac{c}{\tan(\varphi)} \tag{38}$$

$$\eta = \frac{4\ tan^2(\varphi)(9 - 7\sin(\varphi))}{1 - \sin(\varphi)} \tag{39}$$

2.6.4 Mogi Coulomb

Requires only tri-axial test but takes into account intermediate principal stress, shown to be rather accurate

$$\tau_{oct} = a + b\,\sigma_m \tag{40}$$

Where a is the intersection of the line on τ_{oct} axis and b is its inclination. They can be acquired using polyaxial tests but are related to the cohesion and angle of internal friction and can be calculated as:

$$a = \frac{2\sqrt{2}}{3}\,\frac{C_0}{q+1} \tag{41}$$

$$b = \frac{2\sqrt{2}}{3}\,\frac{q-1}{q+1} \tag{42}$$

Using the variables discussed for the Mohr-Coulomb criterion. Figure 22 shows the above criteria applied to triaxial and polyaxial test data for rock and it is clear that the Mohr-Coulomb criterion fits the triaxial data and underestimates strength, the Drucker-Prager criterion overestimates strength and the Mogi-Coulomb criterion is a more accurate fit.

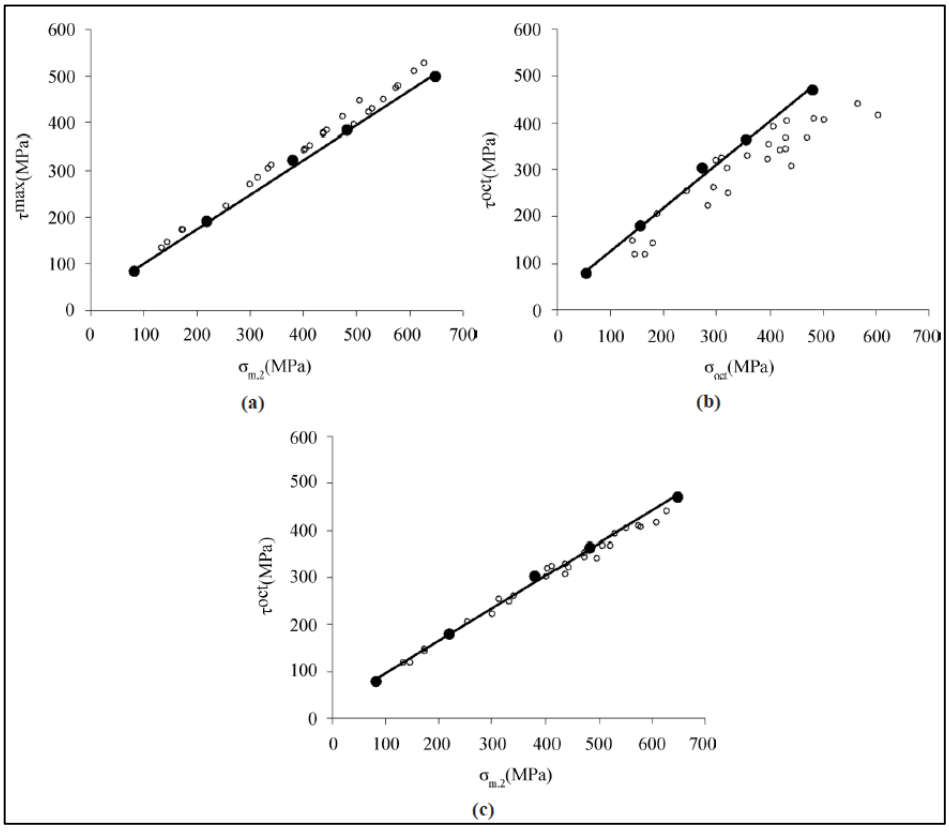

Figure 22: a) Mohr-Coulomb b) Drucker-Prager c) Mogi-Coulomb criteria applied to triaxial and polyaxial rock strength data (Al-Ajmi 2012)

2.7 Mud Window and Wellbore Stability

Borehole instabilities during drilling cause major problems all over the world. Such instabilities often are "stuck pipe" incidents or "lost circulation" incidents. There are many possible reasons for getting stuck but the major reason mechanical collapse of the borehole wall. A lost circulation incident occurs when mud flows into fractures which is usually the case because wellbore pressure is above the fracture pressure. Flow into the wellbore occurs when it is below the pore pressure. These issues are mechanical in nature. Analyzing the geomechanics involved, a safe mud weight window can be established. While many instability incidents stem from chemical reactions with shale, this work focuses on the mechanical issues. Figure 23 shows how different mud weights and pressures affect borehole stability. The window between the pore pressure and minimum horizontal stress is usually considered as safe mud window. While breakouts will occur, they are minor and will not affect the operation too much. The window between breakout pressure and minimum horizontal stress is even safer as the breakouts won't occur, but often it is very narrow.

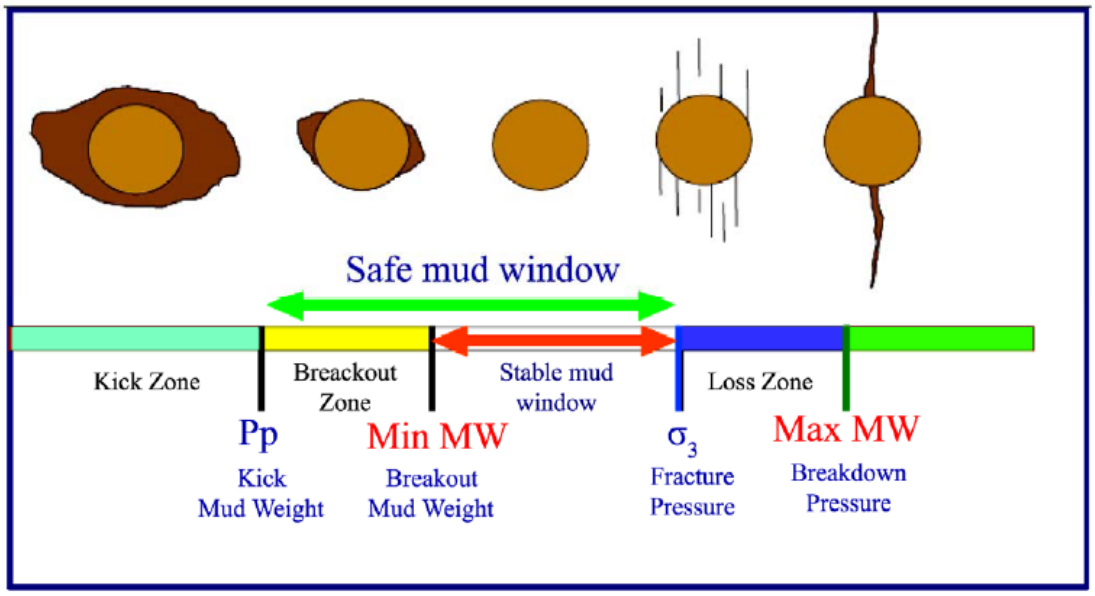

Figure 23: Different mud windows in stability plot (Afsari et al. 2013)

Once a geomechanical model that quantifies the principal stress magnitudes and orientations has been developed, the pore pressure and rock properties it is possible to predict wellbore instability as a function of mud weight and properties. The calculated mud weights are calibrated using real instability events. The breakout mud weight leads to shear failure (breakout) and breakdown mud weight leads to tensile failure (fractures).

To analyze the wellbore stability, the chosen failure criterion discussed above will be calculated using the induced stresses at the borehole wall for the three principal stress parameters. These are commonly acquired using the equations derived by Kirsch in 1898:

$$\sigma_{tan,eff} = 0.5(\sigma_{Hmax} + \sigma_{hmin})(1 + {r_w}^2/r^2) - 0.5(\sigma_{Hmax} - \sigma_{hmax})(1 + 3r_w^4/r^4)\cos(2\theta) - p_w({r_w}^2/r^2) - p_p \quad (43)$$

$$\sigma_{axial,eff} = \sigma_v - 0.5(\sigma_{Hmax} - \sigma_{hmin})v\left(4\frac{r_w^2}{r^2}\right)\cos(2\theta) - p_p \quad (44)$$

$$\sigma_{radial,eff} = 0.5(\sigma_{Hmax} + \sigma_{hmin})(1 - {r_w}^2/r^2) - 0.5(\sigma_{Hmax} - \sigma_{hmax})(1 + 3r_w^4/r^4 - 4r_w^2/r^2)\cos(2\theta) + p_w({r_w}^2/r^2) - p_p \quad (45)$$

With

r_w...wellbore radius

r.....distance from wellbore center to point of interest

θ.....azimuth measured from the direction of maximum horizontal stress

v.....Poisson's ratio

p_p....pore pressure

p_w...wellbore pressure

The pore pressure is subtracted to receive the effective pressures. The stresses can be calculated for any azimuth and distance from the wellbore. Maximum and minima are produced every 90 degrees because of the cosine term. The direction of S_{Hmax} (0 degrees) leads to minima and the direction of S_{Hmin} (90 degrees) leads to maxima. This is why breakouts happen in direction of the minimum horizontal stress and fractures open in direction of the maximum horizontal stress.

The points of interest for a wellbore stability problem are at the borehole wall, so the distance equals the wellbore radius. Setting $r = r_w$ leads to the following, simpler set of equations:

$$\sigma_{tan,eff} = (\sigma_{Hmax} + \sigma_{hmin}) - 2(\sigma_{Hmax} - \sigma_{hmin})\cos(2\theta) - p_w - p_p \quad (46)$$

$$\sigma_{axial,eff} = \sigma_v - 2(\sigma_{Hmax} - \sigma_{hmin})v\cos(2\theta) - p_p \quad (47)$$

$$\sigma_{radial,eff} = p_w - p_p \quad (48)$$

The radial stress loses its cosine term and dependence on azimuth. The reasoning behind this is that the wellbore pressure generated by the mud weight acts uniformly on the wellbore wall.

The equations assume a vertical well, if the section is inclined, formulas from Bradley (1979) are used. The stresses at the wellbore wall can be written as:

$$\sigma_r = p_w \quad (49)$$

$$\sigma_\theta = \sigma_x^\circ + \sigma_y^\circ - p_w - 2\left(\sigma_x^\circ - \sigma_y^\circ\right)\cos(2\theta) - 4\tau_{xy}^\circ \sin(2\theta) \quad (50)$$

$$\sigma_z = \sigma_z^\circ - \nu[2\left(\sigma_x^\circ - \sigma_y^\circ\right)\cos(2\theta) + 4\tau_{xy}^\circ \sin(2\theta)] \quad (51)$$

$$\tau_{\theta z} = 2(-\tau_{xz}^\circ \sin(\theta) + \tau_{yz}^\circ \cos(\theta)) \quad (52)$$

$$\tau_{r\theta} = 0 \quad (53)$$

$$\tau_{rz} = 0 \quad (54)$$

where σ and τ with subscript of r and θ are the normal and shear stresses in a cylindrical coordinate system with the z-direction parallel to the drilling direction; while σ and τ with subscript of x, y and z are the normal and shear stresses in a Cartesian coordinate system which has the same z-axis as the cylindrical system, with the z-direction parallel to the drilling direction; θ is the azimuthal angle measured from the x-axis. The stresses are not effective, so to acquire the effective stresses, pore pressure has to subtracted.

To obtain the stresses required for the calculation above, the conversion of the Cartesian coordinate system's stresses from in-situ principal stresses can be performed through coordinate transformation. The following formulas can be used:

$$\sigma_x^\circ = (\sigma_H \cos(\omega)^2 + \sigma_h \sin(\omega)^2)\cos(\delta)^2 + \sigma_v \sin(\delta)^2 \quad (55)$$

$$\sigma_y^\circ = (\sigma_H \sin(\omega)^2 + \sigma_h \cos(\omega)^2) \quad (56)$$

$$\sigma_z^\circ = (\sigma_H \cos(\omega)^2 + \sigma_h \sin(\omega)^2)\sin(\delta)^2 + \sigma_v \cos(\delta)^2 \quad (57)$$

$$\tau_{xy}^\circ = \frac{1}{2}(\sigma_H - \sigma_h)\sin(2\omega)\cos(\delta) \quad (58)$$

$$\tau_{xz}^\circ = \frac{1}{2}(\sigma_H \cos(\omega)^2 + \sigma_h \sin(\omega)^2 - \sigma_v)\sin(2\delta) \quad (59)$$

$$\tau_{yz}^\circ = \frac{1}{2}(\sigma_H - \sigma_h)\sin(2\omega)\sin(\delta) \quad (60)$$

Using these stresses on the wellbore wall in conjunction with the chosen failure criterion makes calculating safe mud weights possible using the wellbore pressure term from above equations as the wellbore pressure is formed by the mud weight. The resulting equations need to be solved for the wellbore pressure to obtain collapse pressure. Generally, the wellbore pressure has to be higher than the collapse pressure and pore pressure (low critical boundary) and lower than the minimum horizontal strength (high critical boundary, fracture pressure) and not lead to failure according to the failure criterion (shear failure, tensile failure).

Tensile failure occurs when one of the above stresses becomes negative and thus tensile and exceeds the tensile strength. The tensile strength of rocks is generally low and often set to zero, but when reliable data is available it can be given that value. If tensile failure occurs, it is usually due to the tangential stress becoming negative. This does most likely happen in strike slip faulting regimes causing drilling induced fractures. When the wellbore pressure drops below the pore pressure, the radial stress becomes tensile and could cause tensile failure as well.

Chapter 3 MEM Building Process (Case Study)

In this chapter the process of building 1 D MEM for an offshore well are explained in details. The required parameters for developing the MEM are derived according to the geophysical and geomechanical principles and equations presented in the literature review (chapter 2). The applicability of the theory and problematic areas and assumptions are discussed. It is necessary, before we go further to list all the possible challenges which associate with building process of a MEM, the following points are the summary of few of them:

- How reliant a MEM is on which data and how available this data usually is in real operations.
- If information is lacking or the data quality is too low, can reasonable assumptions be made.
- Which data is absolutely necessary to ensure usability of the MEM.

The following flowchart summarizes the workflow of building the model.

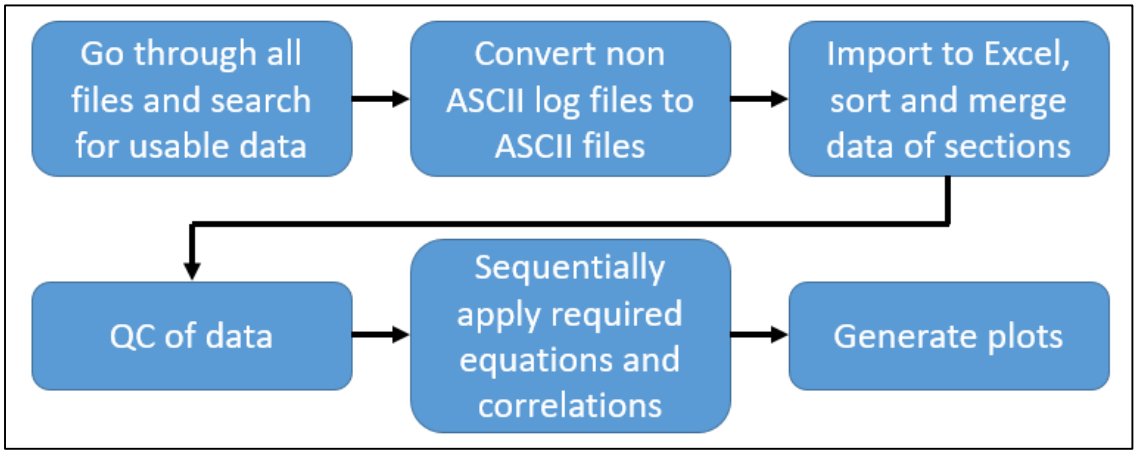

Figure 24: Flowchart for building the model using Excel

3.1 Well Overview

The well is an offshore vertical exploration well in Western Africa with a depth of 5834m at a water depth of 1882m.

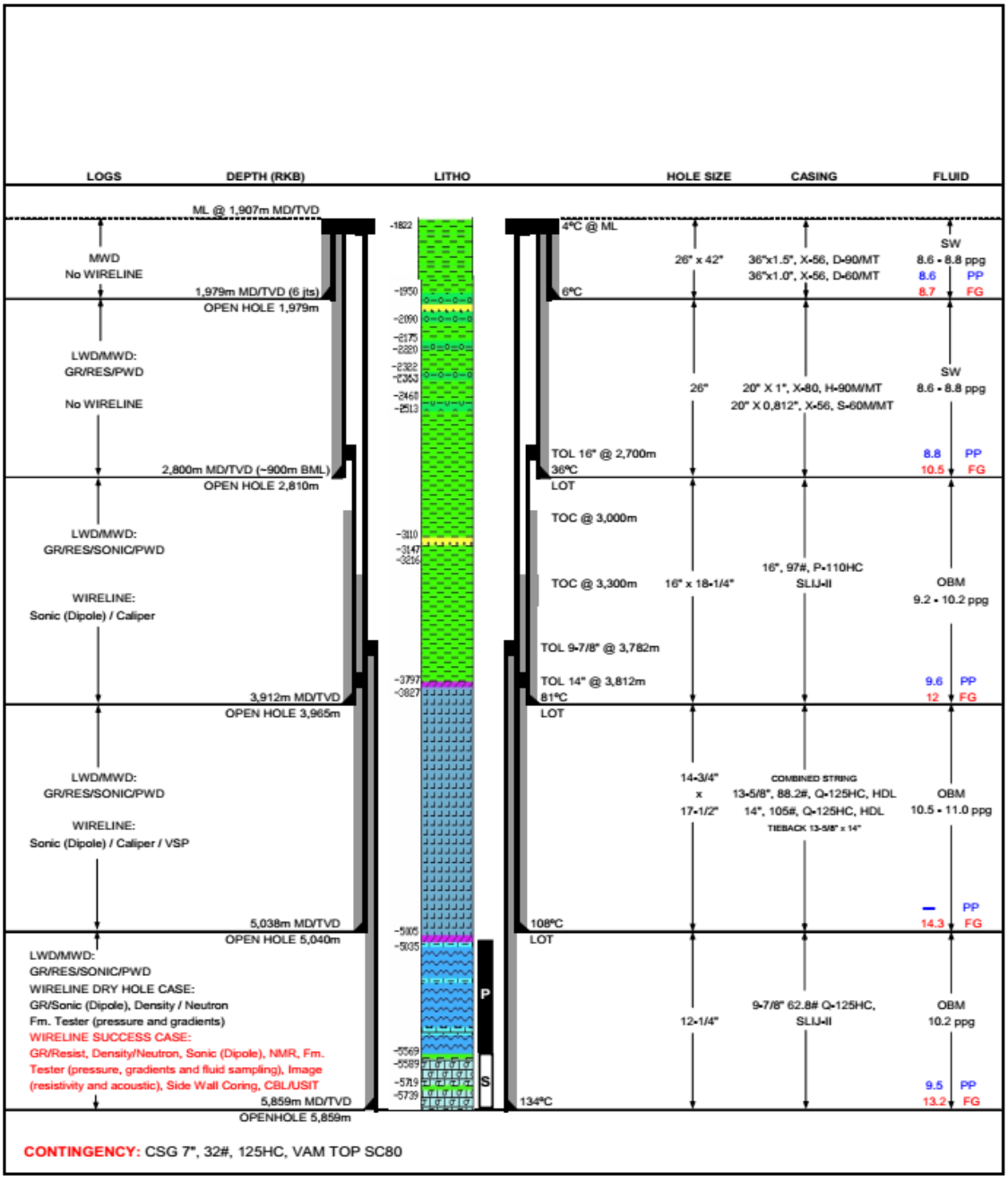

Figure 25: Well schematic

Figure 25 shows the well schematic as it was planned. It has information about the lithology, casing and hole sizes and setting depths, expected pore pressure and fracture

gradients and planned mud weights. On the left side it lists which logs are planned to be run for each section.

As seen in the well schematic, LWD measurements are taken for all but the short surface casing. Table 7 shows the planned logging program. The last interval is run with additional density measurements and formation testing. The reason is that this interval contains the reservoir.

PHASE	INTERVAL	SERVICES
Pilot 8 ½ inch	1882 to 2810m	LWD (Gamma ray, Resistivity, Sonic)
I 26 inch x 42 inch	1907 to 1979m	MWD
II 26 inch	1979 to 2810m	LWD (Gamma ray, Resistivity)
III 16 inch x 18 ¼ inch	2810 to 3965m	LWD (Gamma ray, Resistivity, Sonic)
IV 14 ¾ inch x 17 ½ inch	3965 to 5040m	LWD (Gamma ray, Resistivity, Sonic)
V 12 ¼ inch	5040 to 5859m	LWD (Gamma ray, Resistivity, Density, Sonic)

Table 7: Logging program of the well

In the well planning phase, the company has created a pre drill safe mud weight window. The pore pressure, fracture pressure and overburden stress have been estimated using log measurements and LOT and incidents from offset wells. The results of these estimations are displayed in Figure 26. The pore pressure (red) has been estimated using instability events and the fracture gradient (blue) has been set along LOT data from the offset wells (blue squares). For the salt formation, a pore pressure of 0 has been set and a Poisson's ratio of 0.4 has been used. The pore pressure there was set to zero and the fracture gradient was set equal to the overburden gradient.

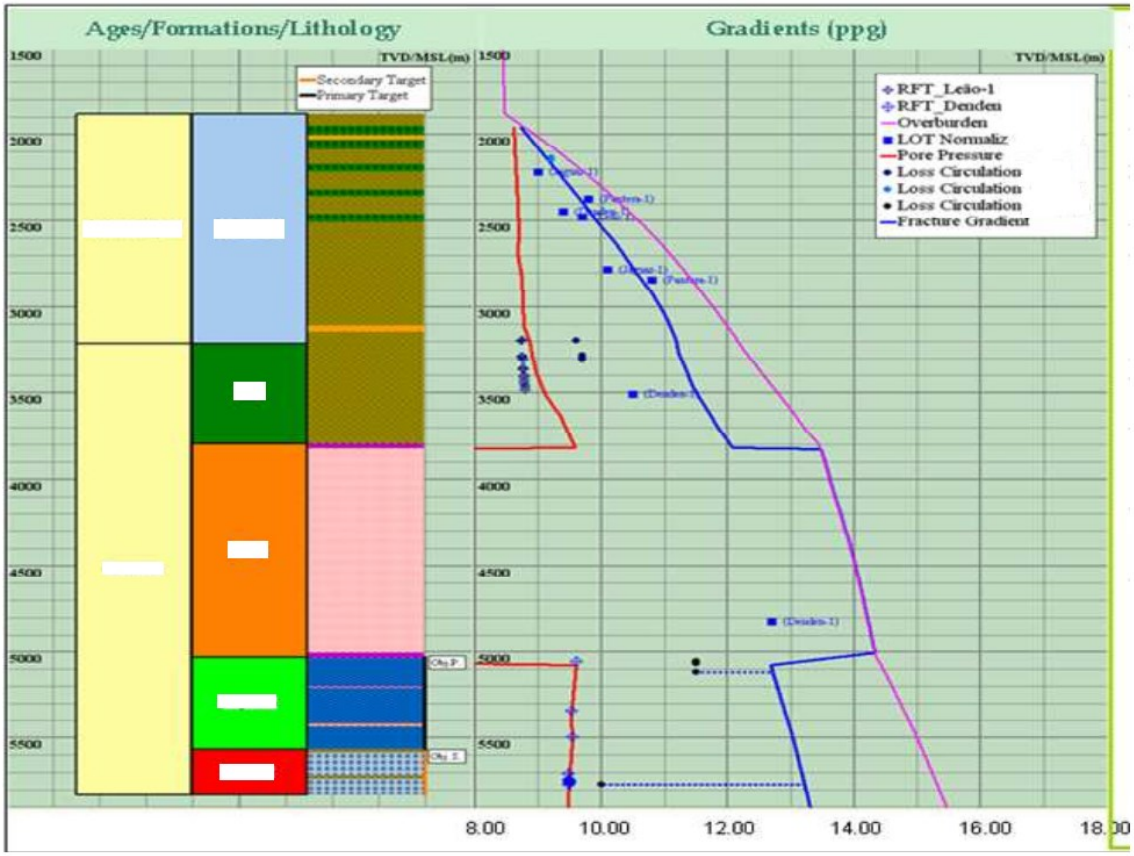

Figure 26: Geopressure forecast using offset well data

The company used these estimations to set the safe mud weights for the well which is under investigation by this study. Instability events occurred while drilling the well, which means that the conventional estimations could not successfully predict the pressures in these trouble zones. At the end of this chapter, the simple MEM built in this thesis is compared with the instability events to assess its quality and find out whether it could predict the trouble zones better than the conventional method of planning mud window.

3.2 Data Gathering

The available data set from an offshore exploration well in Western Africa has been checked and the following is available to work with:

- Drilling program
- Hydraulics data
- BHA plans
- Bit run summary reports
- Drilling mechanics data reports (ROP, WOB, Torque, Shocks, ECD)

- End of Well report
- Petrophysical log data plots and data files in ASCII and DLIS formats, sometimes .pbin and .bin files
- Survey reports, trajectory data
- Fishing diagrams
- Pilot hole log data
- Incident reports
- Test data

3.3 Log and Core Data

The well has been drilled with following sections: 26″, 16″, 14 ¾″, 12 ¼″. Before that, a 8″ pilot hole was drilled. Looking through various data files this MEM relevant log data has been found:

26″ section: Gamma Ray, Resistivity, ECD, Annulus Pressure, Compressional slowness,

16″ section: Gamma Ray, Resistivity, ECD, Annulus Pressure, Compressional slowness, shear slowness

14 ¾″ section: Gamma Ray, Resistivity, ECD, Annulus Pressure, Delta-T Compressional

12 ¼″ section: Gamma Ray, Resistivity, ECD, Annulus Pressure, Delta-T Compressional, Bulk Density

8″ pilot hole: Delta-T Compressional

Furthermore, the following test data has been acquired from files.

Depth (m)	E (GPa)	UCS (kPa)
3702	11.01	27011
3721	12.57	28774
3857	26.12	119443
3861	21.69	142306
3925	21.07	72065
4036	16.47	49930
4074	18.26	76398

Table 8: Young's Modulus and UCS measurements from cores

Depth (m)	LOT (kPa)	Minifrac (kPa)
2795	34956	
3665	61817	
3725		62692
3760		63613
3802	60336	
3930		67537
3990		69802
4050		71754
5030	82978	

Table 9: LOT and Minifrac results

3.4 Data Conversion and Quality Control

After identifying all relevant and usable data files the non-ASCII files have been converted to ASCII files using free software from a service company. Figure 27 shows a part of such a file for the 26″ section opened by a text editor.

```
#-------------------------------------------------------------
#            DEPT         ROP5          TVDE          GR        GR_CAL         A16H         A16L         A22H         A22L
#                    (DRILLING_)  (DnMWorkfl)      (ARC9)       (ARC9)       (ARC9)       (ARC9)       (ARC9)       (ARC9)
#                            (RT)         (RT)        (RM)         (RM)         (RM)         (RM)         (RM)         (RM)
#                          (6in)        (6in)       (6in)        (6in)        (6in)        (6in)        (6in)        (6in)
~ASCII
       1959.86400     46.36394   1959.85800     36.65499     14.65341      0.20000      0.15000      0.20000      0.30000
       1960.01640     55.30130   1960.01039     47.03617     18.80345      0.20000      0.15000      0.20000      0.30000
       1960.16880    168.81230   1960.16279     59.83333     23.91931      0.20000      0.15000      0.20000      0.30000
       1960.32120    164.59200   1960.31518     61.57736     24.61652      0.20000      0.15000      0.20000      0.30000
       1960.47360     81.64381   1960.46758     56.46983     22.57470      0.20000      0.15000      0.20000      0.30000
       1960.62600     80.87986   1960.61997     52.70618     21.07012      0.20000      0.15000      0.20000      0.30000
       1960.77840     73.15200   1960.77237     49.93661     19.96294      0.20000      0.15000      0.20000      0.30000
       1960.93080     15.29665   1960.92476     47.36333     18.93423      0.20000      0.15000      0.20000      0.30000
       1961.08320     15.51291   1961.07716     46.63350     18.64248      0.20000      0.15000      0.20000      0.30000
       1961.23560     15.56388   1961.22955     49.03690     19.60327      0.20000      0.15000      0.20000      0.30000
       1961.38800     14.89523   1961.38195     49.92402     19.95791      0.20000      0.15000      0.20000      0.30000
       1961.54040     14.22576   1961.53434     46.93550     18.76320      0.20000      0.15000      0.20000      0.30000
       1961.69280     13.15161   1961.68674     45.04173     18.00614      0.20000      0.15000      0.20000      0.30000
       1961.84520     11.68562   1961.83914     43.47762     17.38086      0.20000      0.15000      0.16302      0.30000
       1961.99760     11.00950   1961.99153     42.08340     16.82350      0.20000      0.15000      0.14733      0.30000
       1962.15000     10.26456   1962.14393     49.46725     19.77531      0.20000      0.15000      0.14907      0.30000
       1962.30240      9.62526   1962.29632     59.94658     23.96459      0.20000      0.15000      0.14915      0.30000
       1962.45480     15.63077   1962.44872     61.66796     24.65274      0.20000      0.15000      0.20000      0.30000
       1962.60720     13.75038   1962.60111     56.51890     22.59432      0.20000      0.15000      0.20000      0.30000
       1962.75960     13.22024   1962.75351     52.83452     21.12143      0.20000      0.15000      0.14907      0.30000
       1962.91200     13.10444   1962.90590     51.71713     20.67474      0.20000      0.15000      0.16611      0.30000
       1963.06440     12.39864   1963.05830     49.12498     19.63848      0.20000      0.15000      0.14712      0.30000
       1963.21680     12.00960   1963.21069     49.09982     19.62842      0.20000      0.15000      0.14730      0.30000
       1963.36920     12.97021   1963.36309     54.56094     21.81160      0.20000      0.15000      0.20000      0.30000
       1963.52160     11.96163   1963.51548     59.97174     23.97465      0.20000      0.15000      0.14938      0.30000
       1963.67400     12.00525   1963.66788     56.82593     22.71706      0.20000      0.15000      0.20000      0.30000
       1963.82640     12.38465   1963.82027     50.34556     20.12643      0.20000      0.15000      0.14911      0.30000
       1963.97880     13.51346   1963.97267     53.11388     21.23311      0.20000      0.15000      0.14962      0.30000
       1964.13120     14.47599   1964.12506     53.75562     21.48965      0.20000      0.15000      0.14807      0.30000
       1964.28360     14.40000   1964.27746     45.56393     18.21490      0.19795      0.15000      0.14388      0.30000
       1964.43600     14.78814   1964.42986     45.52617     18.19980      0.20000      0.15000      0.14695      0.30000
```

Figure 27: ASCII data file Example

The measured parameters are lined up at the top with the measured values below. The next step was to import all these text files for the different sections into a Microsoft Excel file. The columns not required for the MEM, such as above Resistivity measurements at various frequencies, have been deleted and the data from the sections combined in one sheet to receive continuous streams of data for the whole wellbore.

The data included many Null values represented by a certain set value. This makes it impossible to plot and analyze it properly. The values have been replaced by values lying linearly between the previous and next measured value. Sometimes longer sections of Null values occurred making this methodology prone to error.

The following figure shows an excerpt of the Excel file after replacing the null values.

	A	B	C	D	E	F	G	H	I	J	K
1											
2	Section	DEPTH [m]	TVD [m]	Gamma Ray	Gamma Ray Calibrated	Downhole Annulus Pressure [psi]	ECD [ppg]	Compressional slowness [us/ft]	Shear Slowness [us/ft]	Compressional slowness computed	Bulk Density [g/cm³]
3											
4											
12182	16	3815.6388	3815.628		15.58067	6442.99982	9.91327	65.7317	171.2	-999.25	2.3254
12183	16	3815.7912	3815.772		15.1273	6447.99927	9.92053	68.93079	127.2	65.99999	2.3681
12184	16	3815.9436	3815.907		14.1229	6446.00065	9.91712	69.38007	164.8	68.20001	2.3928
12185	16	3816.096	3816.036		13.19552	6444.99989	9.91527	70.40874	160	70.20001	2.4155
12186	16	3816.2484	3816.225		12.83633	6444.00058	9.91321	70.65301	173.6	-999.25	2.4389
12187	16	3816.4008	3816.359		12.61717	6446.00065	9.91585	70.52298	151.6	70.99999	2.4758
12188	16	3816.5532	3816.547		13.43988	6451.0001	9.9233	70.44806	129.6	70.99999	2.4006
12189	16	3816.7056	3816.637		15.23583	6444.99989	9.91372	68.97398	124.8	70	2.3481
12190	16	3816.858	3816.848		16.02353	6449.00003	9.91936	68.91796	168	69.19999	2.2683
12191	16	3817.0104	3816.994		15.82048	6449.99934	9.92068	67.92181	171.2	67.4	2.2511
12192	16	3817.1628	3817.144		15.75396	6449.00003	9.9188	67.24123	172.8	68.40002	2.2377
12193	16	3817.3152	3817.288		15.97451	6449.00003	9.91823	66.27562	174.4	67.19999	2.2374
12194	16	3817.4676	3817.433		15.41437	6447.99927	9.91625	65.99365	169.2	66.59999	2.2688
12195	16	3817.62	3817.603		14.96276	6447.99927	9.9159	66.3937	164	66.2	2.3034
12196	16	3817.7724	3817.762		15.05378	6453.00017	9.92341	65.66072	163.2	65.80001	2.2993
12197	16	3817.9248	3817.901		15.20607	6449.99934	9.91809	65.04124	171.2	66.59999	2.2807
12198	16	3818.0772	3818.049		15.80647	6451.99941	9.92103	65.60412	172	64.19999	2.2891
12199	16	3818.2296	3818.167		16.66769	6453.00017	9.9219	66.88885	174.4	64.79999	2.2799
12200	16	3818.382	3818.362		16.60467	6447.99927	9.91413	67.26177	172.8	64.79999	2.3
12201	16	3818.5344	3818.513		14.75796	6447.99927	9.91372	68.54845	171.2	67.4	2.346
12202	16	3818.6868	3818.622		13.10729	6453.00017	9.92079	69.50327	163.2	67.79999	2.4703
12203	16	3818.8392	3818.825		13.15981	6453.00017	9.92032	68.78586	172	68.59999	2.4977

Figure 28: Log data in Excel

As next step the data has been plotted to get an idea about its quality. The sonic, gamma ray and density measurements had a lot of outliers. The outliers have been reduced using a simple IF function in Excel that equals the previous value in case the difference between current and previous value gets bigger than a certain value. The figure below shows a comparison between shear slowness plots before filtering and the same graph after filtering.

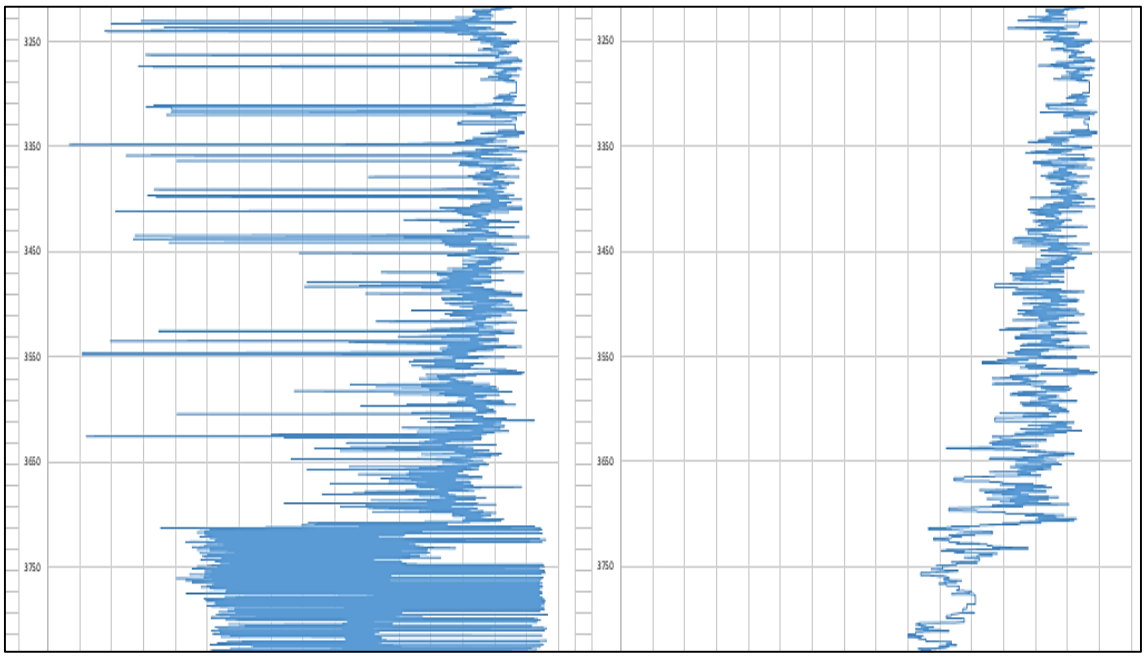

Figure 29: Comparison of unfiltered (left) and filtered (right) bulk density data

With the log data finally imported and rough outliers filtered out the calculation of stresses and rock properties could begin.

3.5 Overburden Stress

As discussed before, in theory the overburden stress will be derived using bulk density data. The reality in this case is that density measurements have not been acquired over the whole depth. It has only been measured for two tool runs. As a result, a compromise had to be done. The equivalent density of the overburden gradient from the drilling program has been added to the data file. That data has been acquired from multiple offset wells so the reliability is seen as rather high. Where density measurements are available, they were used, otherwise the stress has been calculated using the gradient from the offset wells. The following figure shows the overburden stress. The change in overpressure gradients did not have a big impact on the slope of the pressure, it is close to linear.

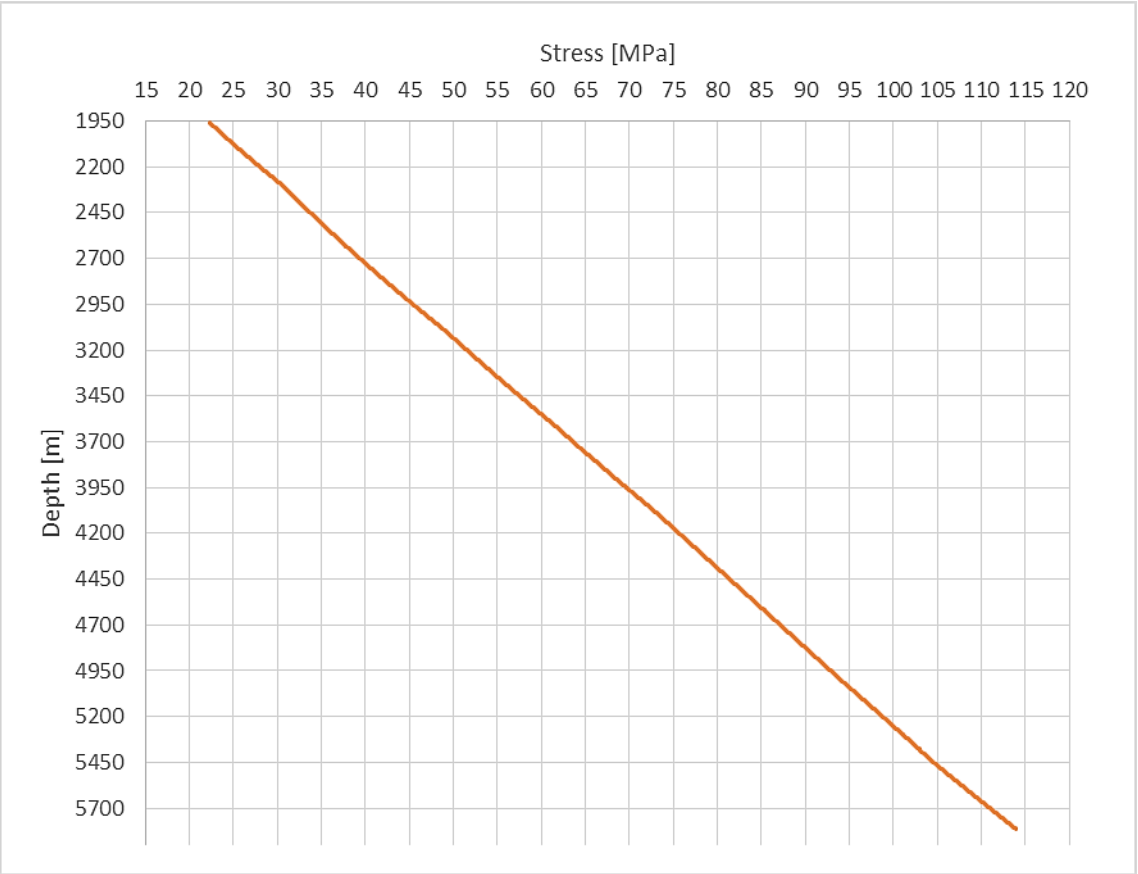

Figure 30: Overburden stress

3.6 Elastic Properties

The equations 2 to 5 in chapter 2.2 were used to calculate the elastic moduli. Unfortunately, they require the bulk density for calculation which was not measured over the whole range. Using the overburden stress data, the density has been backwards calculated for the sections without density data. Where the overburden stress slope changes, the density makes a jump. Using this data, the dynamic shear, bulk and Young's modulus and poissons ratio could be calculated. The available Young's modulus data from cores has been used to calibrate the section they were taken from. The calculated value for R squared equals 0.9997 so a good fit could be achieved. The other sections did not have core data but they have been slightly modified to be in line with the calibrated section. The following figure shows the calibrated static Young's modulus together with the core data. As no core data was available for other sections, the accuracy of their measurements has to be doubted and is prone to error. In the literature often the assumption has been made that the dynamic properties equal the static properties. As other assumptions have been made for these sections like backwards calculating the density, the accuracy drops further.

But it should be noted that increasing trend of the Young's modulus makes sense because of compaction and it fits nicely with the calibrated data. The following plots show the Young's modulus for the section with cores and the whole depth.

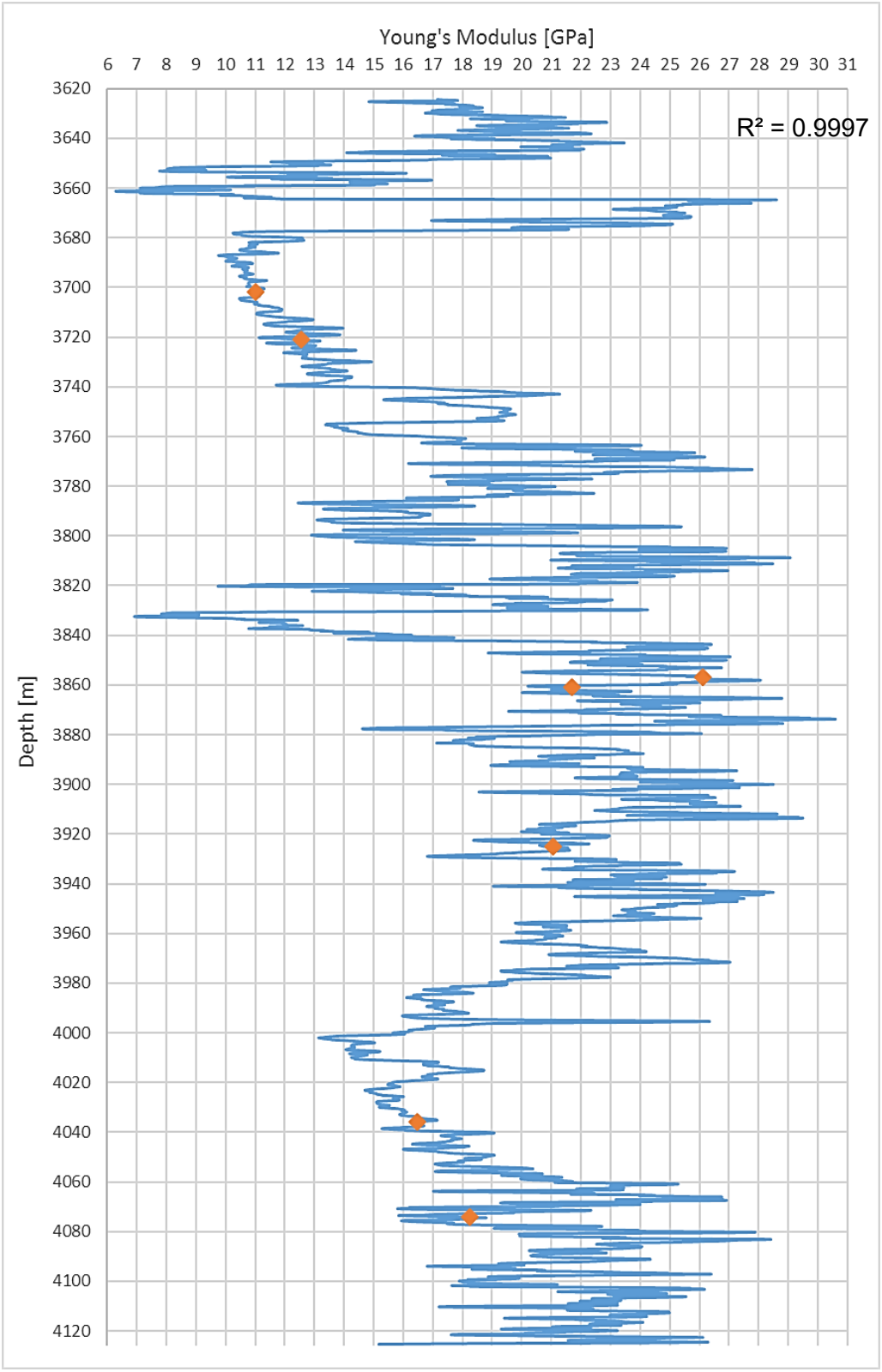

Figure 31: Static Young's Modulus, log data in blue, core data in orange

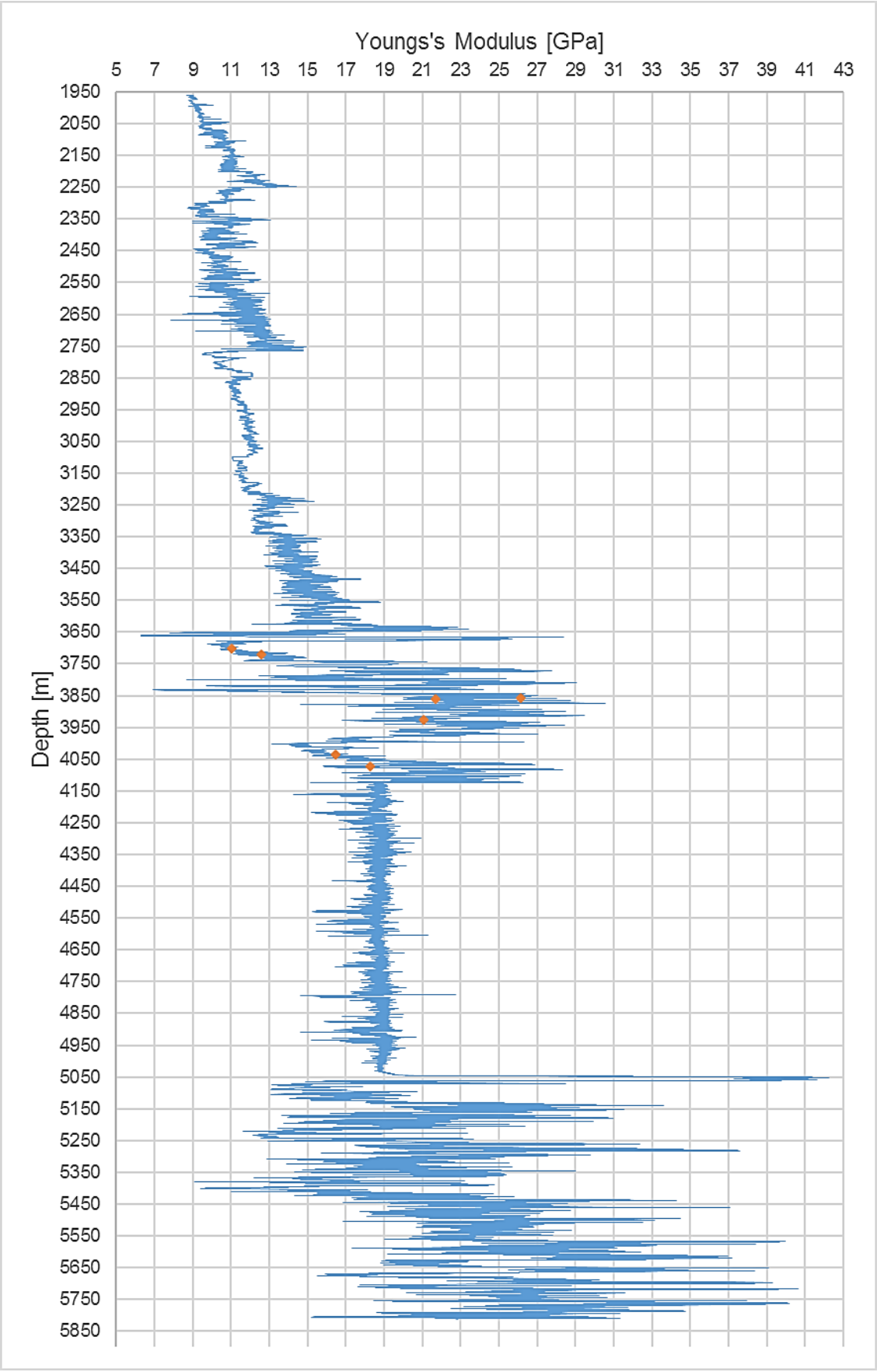

Figure 32: Static Young's modulus over whole depth

3.7 Rock Strength

In theory, UCS is usually derived from published correlations for rock types using the Young's modulus. The results are then calibrated using core data. Not having data available can lead to high deviations. As for the Young's modulus, UCS data from cores is available from the same cores. The core data was plotted and multiple correlations run and modified to find a good fit using a R squared calculation.

The best fit for the sections has been achieved using the correlation from Militzer and Stoll (1973) from Table 3. The correlation uses the compressive slowness measurements. The R squared value is 0.983. It has also been applied to other sections, but as no core data is available for calibration the reliability of the results is highly uncertain. The following two figures show the UCS in the section that had cores available and over the whole depth.

Looking at the second plot it is easy to recognize the section that has been calibrated compared to the ones that have not. It is a lot more volatile to fit the core data while the other sections have a rather clear linear or constant trend. It can be assumed that a MEM without core data for calibration is very bad even though literature sometimes states that uncalibrated data can be used if no cores are available.

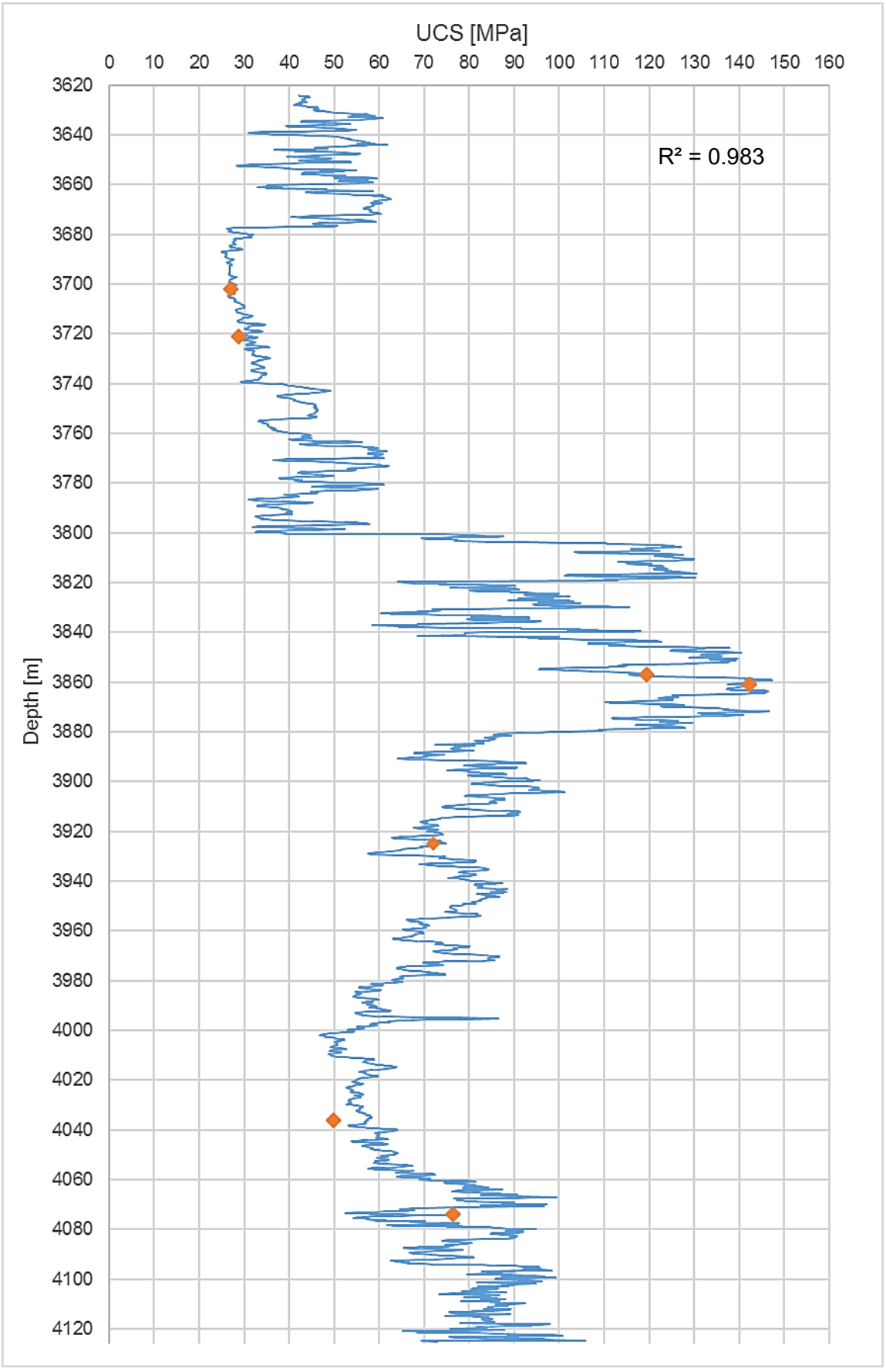

Figure 33: UCS for section with cores

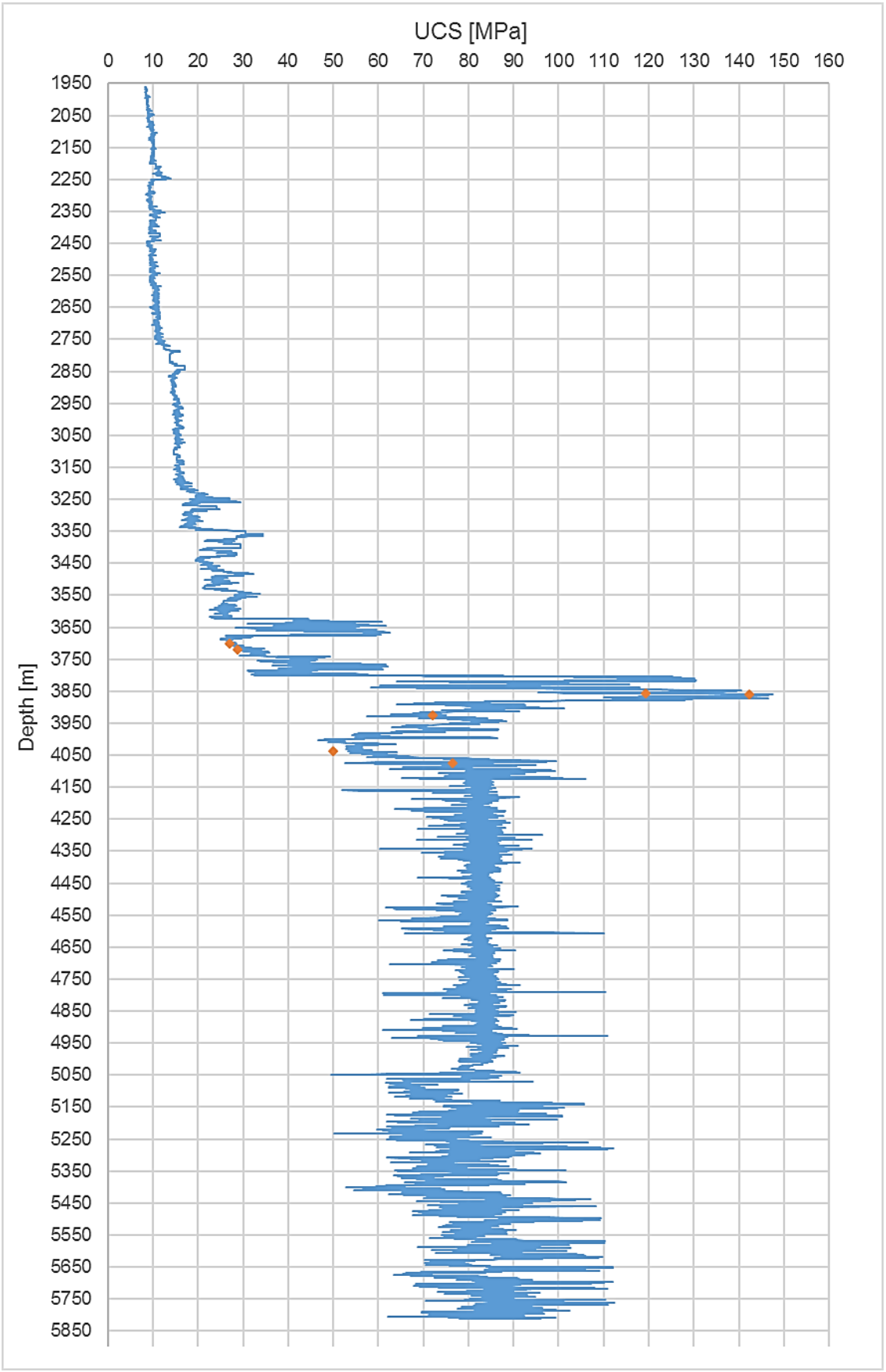

Figure 34: UCS for the whole depth

3.8 Pore Pressure

For pore pressure gradient data, the available data from the drilling program has been input into the table. The halite section did not have data available so a model for that section was made. Resistivity data was used to find a linear equation for the normal compaction trend. This has been used for Eaton's method assuming 8.7ppg as gradient for the hydrostatic pressure. The calculated pore pressure gradients have been input into the file and the corresponding pressure values calculated.

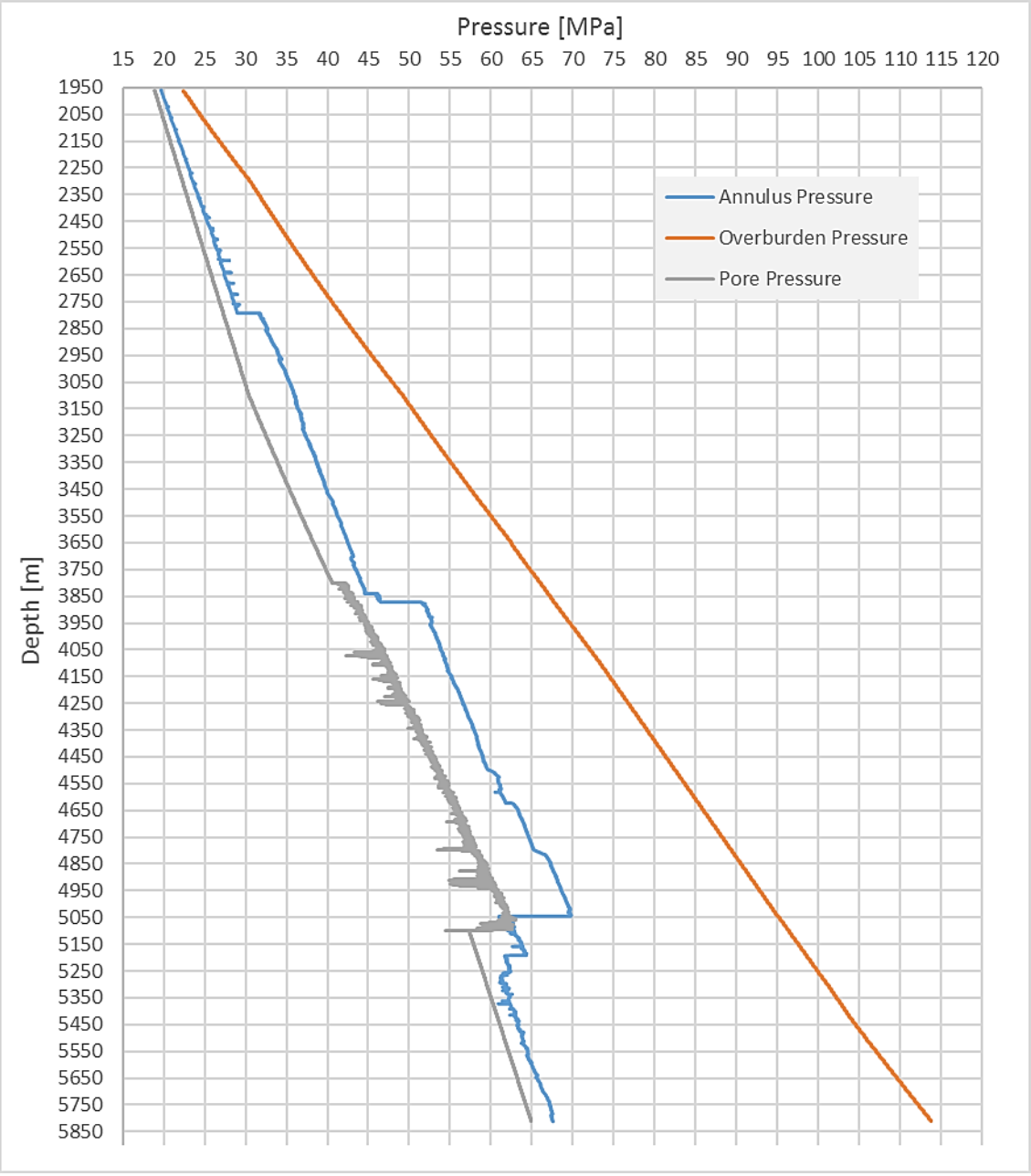

Figure 35: Pressure profiles in comparison

3.9 Min. and Max. Horizontal Stress

To calculate the minimum horizontal stress multiple formulas have been found and tried. In the end the formulas mentioned in chapter 2.5.1 in this thesis have been used. The tectonic stress has been set as calibration factor. The maximum horizontal stress has then been estimated using the same equation but different calibration using the minifrac results. No image logs were available to analyze fractures. Calibration is required for reliable results, so the following available test data from the drilling program have been used.

Depth (m)	LOT (kPa)	Minifrac (kPa)
2210	23390	
2390	27824	
2450	27082	
2490	28549	
2790	32973	
2795	34956	
2850	36028	
3510	43340	
3665	61817	
3725		62692
3760		63613
3802	60336	
3880	61506	
3930		67537
3990		69802
4050		71754
4810	71836	
5030	82978	

Table 10: Pressure test results

The resulting plots for the minimum and maximum horizontal stress including core data and overburden stress is displayed on the next page.

As no images were available, the orientation of the stresses is unclear.

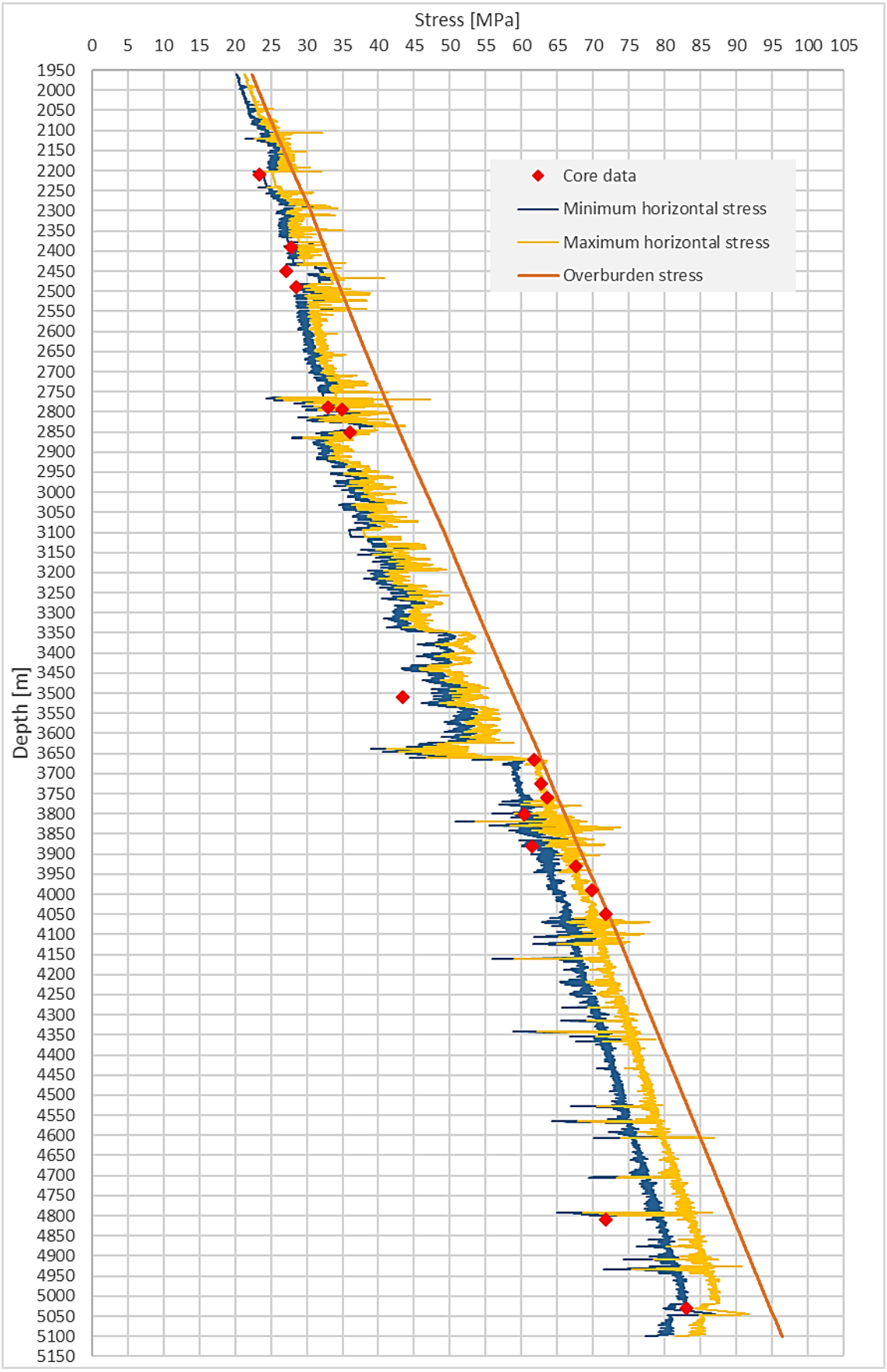

Figure 36:Principal horizontal stresses with overburden stress and core data

3.10 Induced Stresses

The induced stresses were calculated using the Kirsch equations discussed in chapter 2.7. For wellbore stability considerations, the stresses at the borehole wall are relevant so the equations where the radius was set to wellbore radius were used. The pore pressure is subtracted to receive effective stresses. As an example, the following figure shows the induced effective stresses at the borehole wall at the depth 3700m.

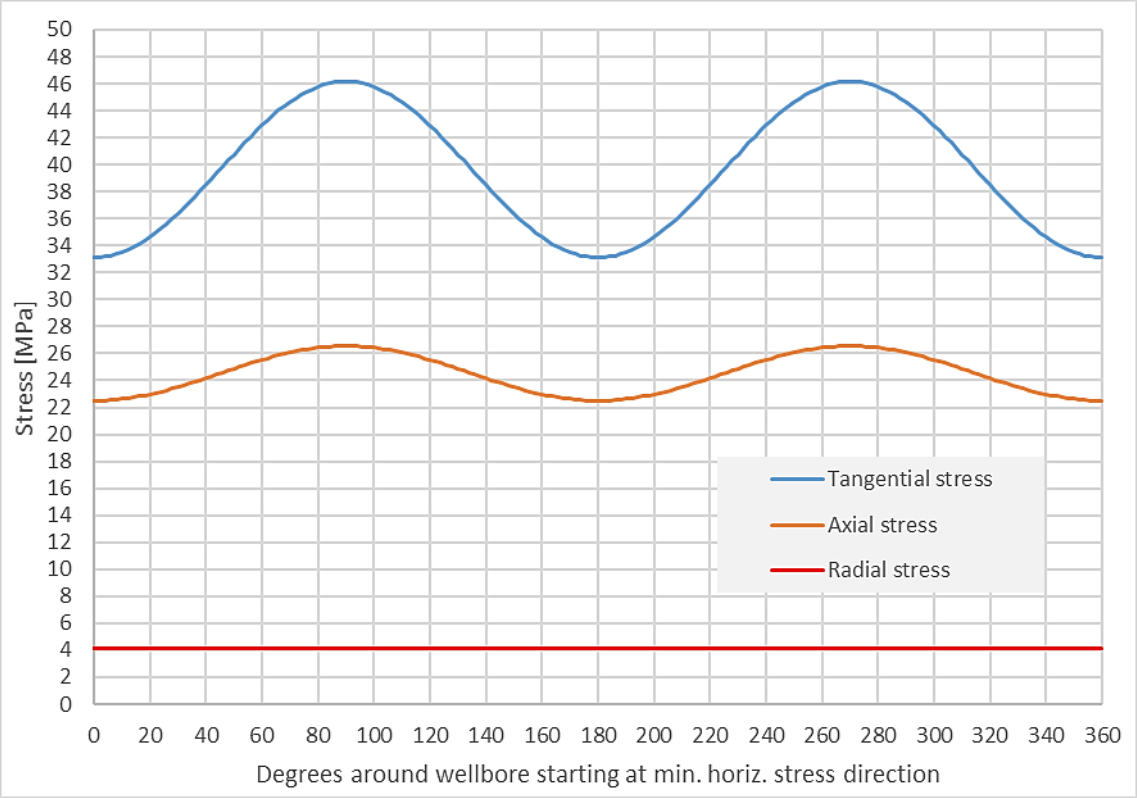

Figure 37: Induced effective stresses at 3700m

As can be seen in the plot the minimum values occur at 0 degrees and the maximum values at 90 degrees measured from the minimum stress direction around the borehole. So the maxima occur in direction of the min. hor. stress and the minima in direction of max. horizontal stress. This is why fractures start perpendicular to the minimum stress direction. The following page shows the plot of these minimum and maximum stresses and the radial stress.

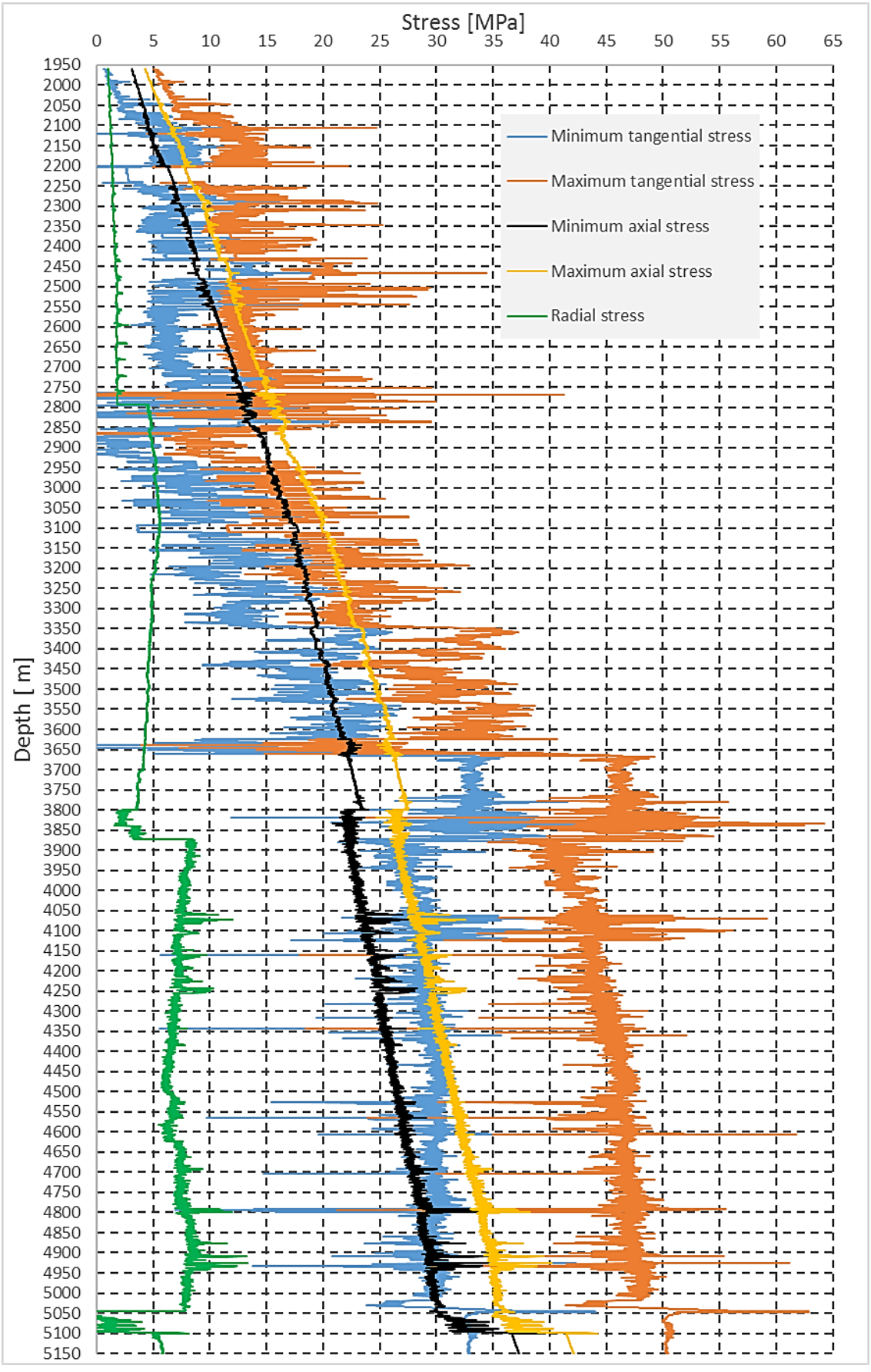

Figure 38: Induced effective stresses for the whole depth

3.11 Failure and Stability

As next step a failure criterion had to be chosen for comparison. For this case study the Mohr Coulomb criterion has been used, because the other criteria lead to the need to solve complex equations for the wellbore pressure which is very complicated using Excel. The Mohr Coulomb criterion leads to rather conservative results. The angle of internal friction has been assumed to be 34 degrees, no core data was available. Correlations are available, but without core data to calibrate the results, the uncertainty is too high.

Tensile failure can occur when either tangential stress is negative (tensile) or the radial stress is lower than the tensile strength. The radial stress equals wellbore pressure minus pore pressure, so this happens when the wellbore pressure drops too low. These values have been calculated and found to be very low. Collapse would occur before tensile failure at low mud weights would occur so it was not included into the following plots. This boundary is often not even calculated in practice.

As seen in the last chapter, the most interesting angles are 90 degrees from the minimum horizontal stress and 0 degrees or 180 degrees. At 90 degrees the stresses are maximal, so collapse (shear failure) may occur, at 0 or 180 degrees the stresses are minimal so fractures may occur.

For the direction of the maximum horizontal strength (90 degrees from minimum) the equations for the induced stresses become:

$$\sigma_{tan,eff} = 3\sigma_{Hmax} - \sigma_{hmin} - p_w - p_p \tag{61}$$

$$\sigma_{axial,eff} = \sigma_v + 2(\sigma_{Hmax} - \sigma_{hmin})v - p_p \tag{62}$$

$$\sigma_{radial,eff} = p_w - p_p \tag{63}$$

The stresses have been calculated and analyzed which stresses are the principal stresses σ_1 and σ_3. Most of the time the tangential stress was the largest principal stress and for some sections the axial stress was larger than the tangential stress, the radial stress being the smallest.

That leaves two cases with differing ways to calculate the wellbore pressure causing collapse:

$$\sigma_{tan,eff} > \sigma_{axial,eff} > \sigma_{radial,eff} \tag{64}$$

Resulting in failure occurring at:

$$p_w \leq \frac{3\sigma_{Hmax} - \sigma_{hmin} - p_p(1-q) - UCS}{(q+1)} \tag{65}$$

$$\sigma_{axial,eff} > \sigma_{tan,eff} > \sigma_{radial,eff} \tag{66}$$

resulting in failure occurring at:

$$p_w \leq \frac{\sigma_v + 2(\sigma_{Hmax} - \sigma_{hmin})v - p_p(1-q) - UCS}{q} \tag{67}$$

The stresses and pressures were then used to calculate their equivalent mud weights to create typical stability plots. The following figures show the results for different sections and the whole profile. To smooth the data further, the increment has been reduced.

The last figure shows the used ECD, lower and upper MW boundaries. The "used MW" data was taken from daily reports and final log reports.

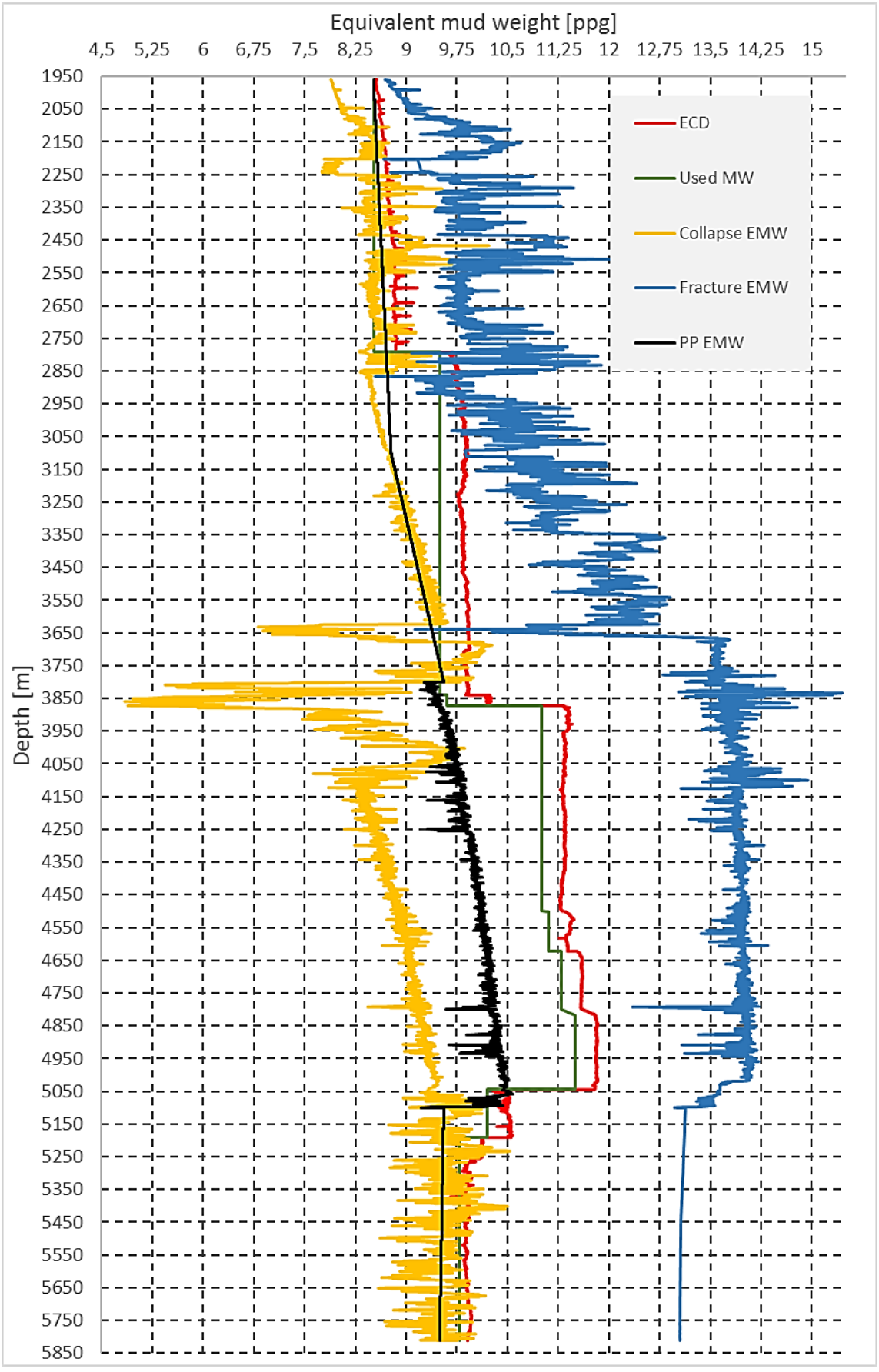

Figure 39: EMW for whole depth

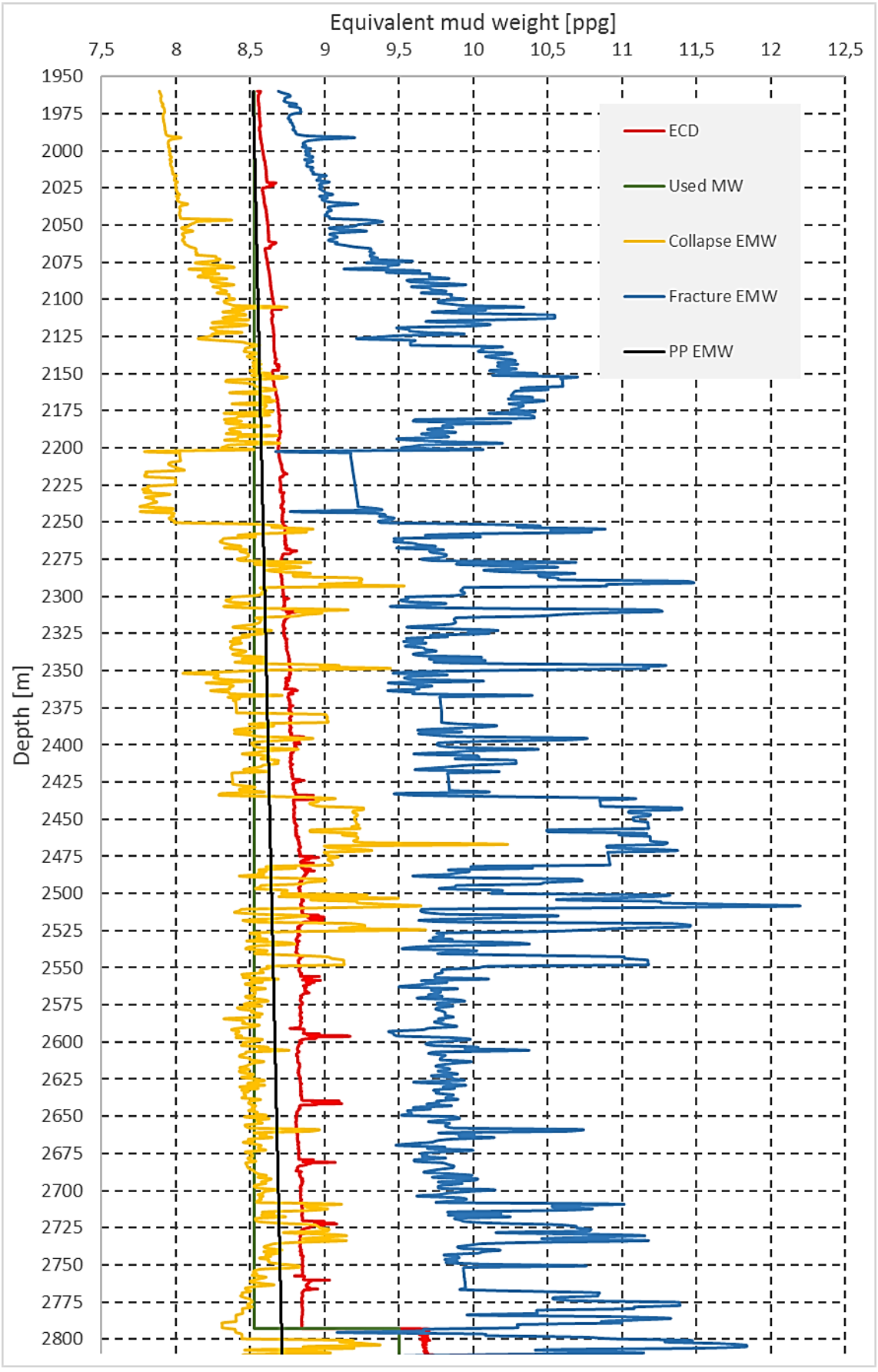

Figure 40: EMW for 26 inch section

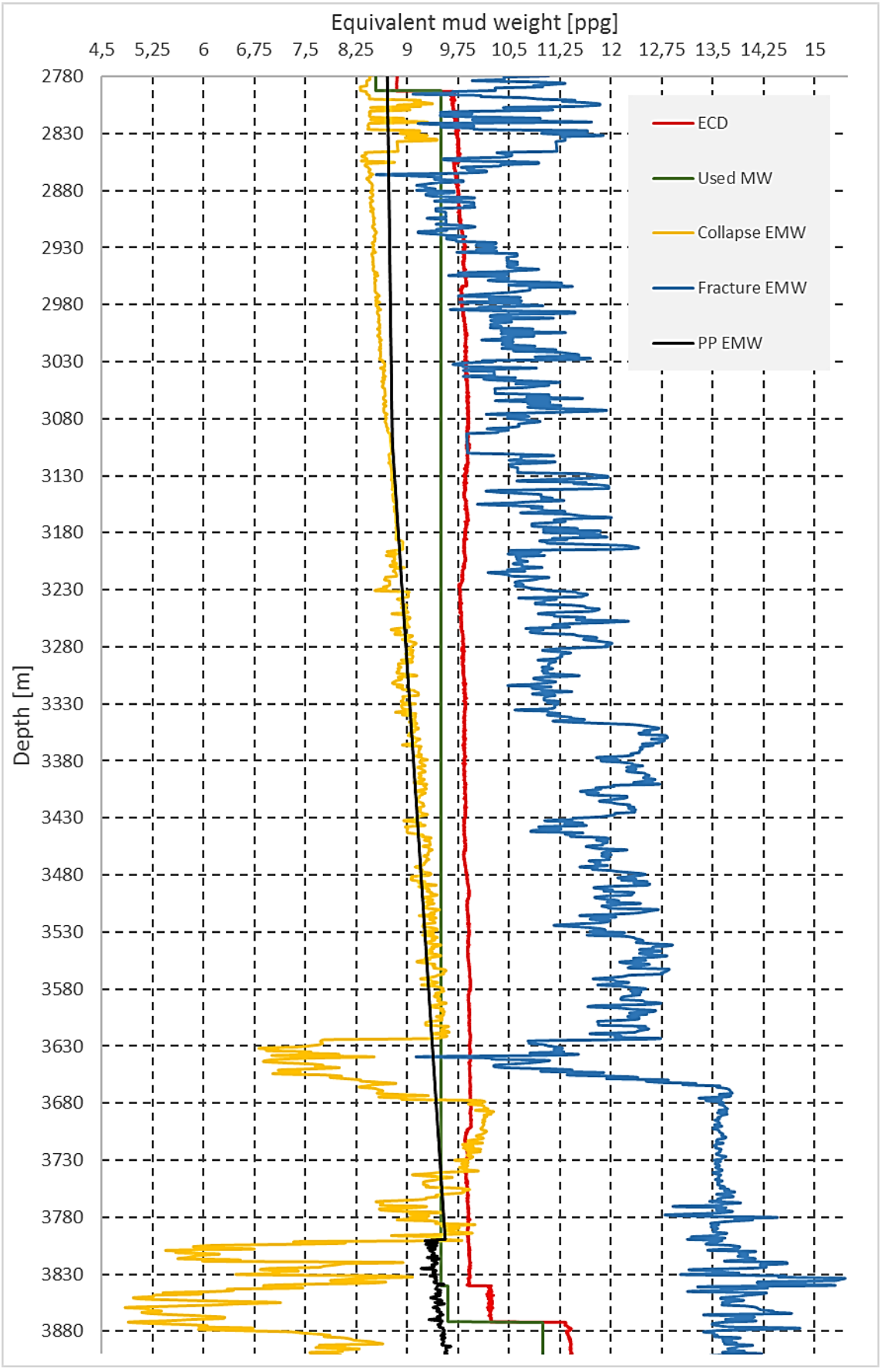

Figure 41: EMW for 16 inch section

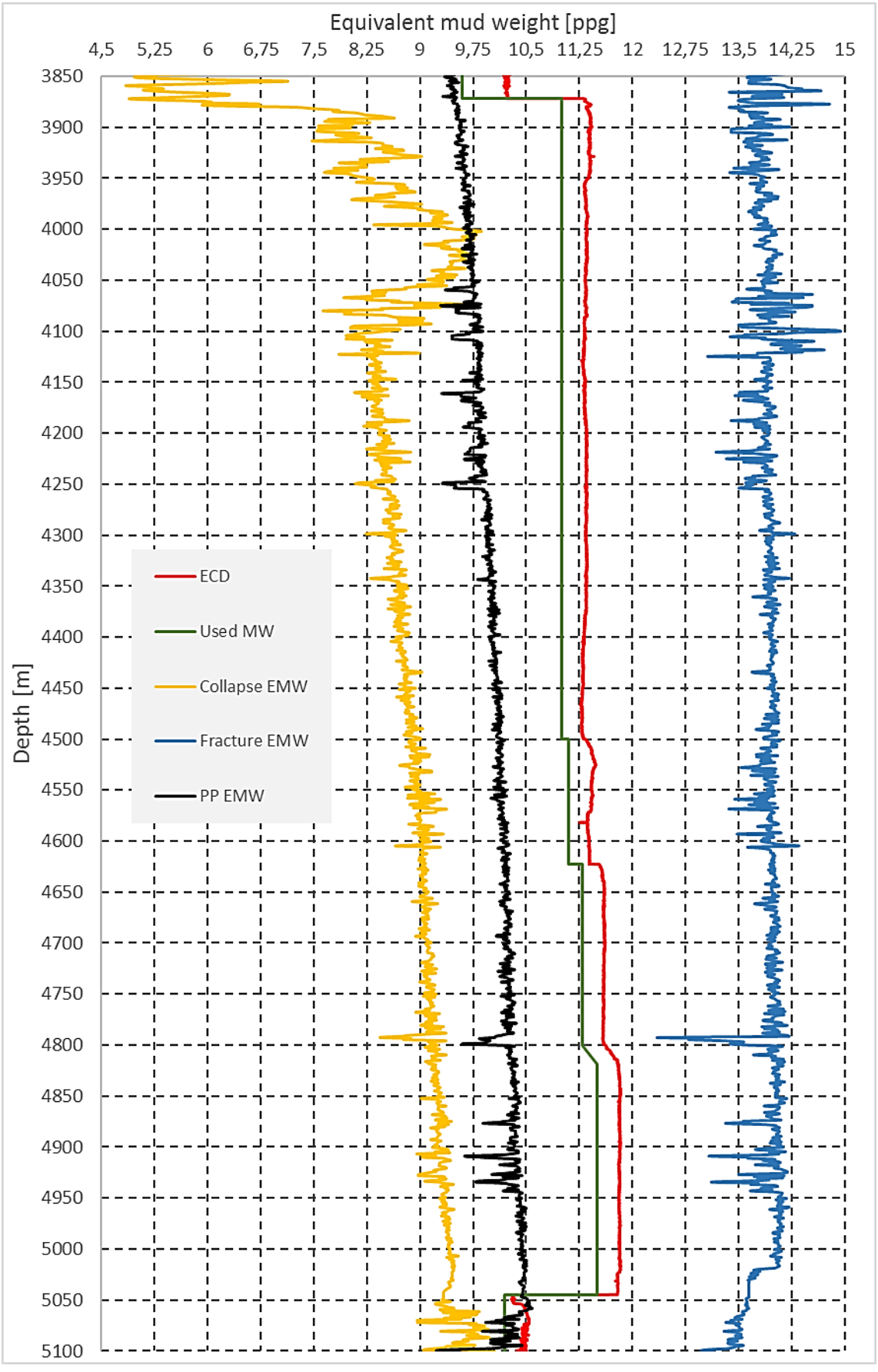

Figure 42: EMW for 14 ¾ inch section

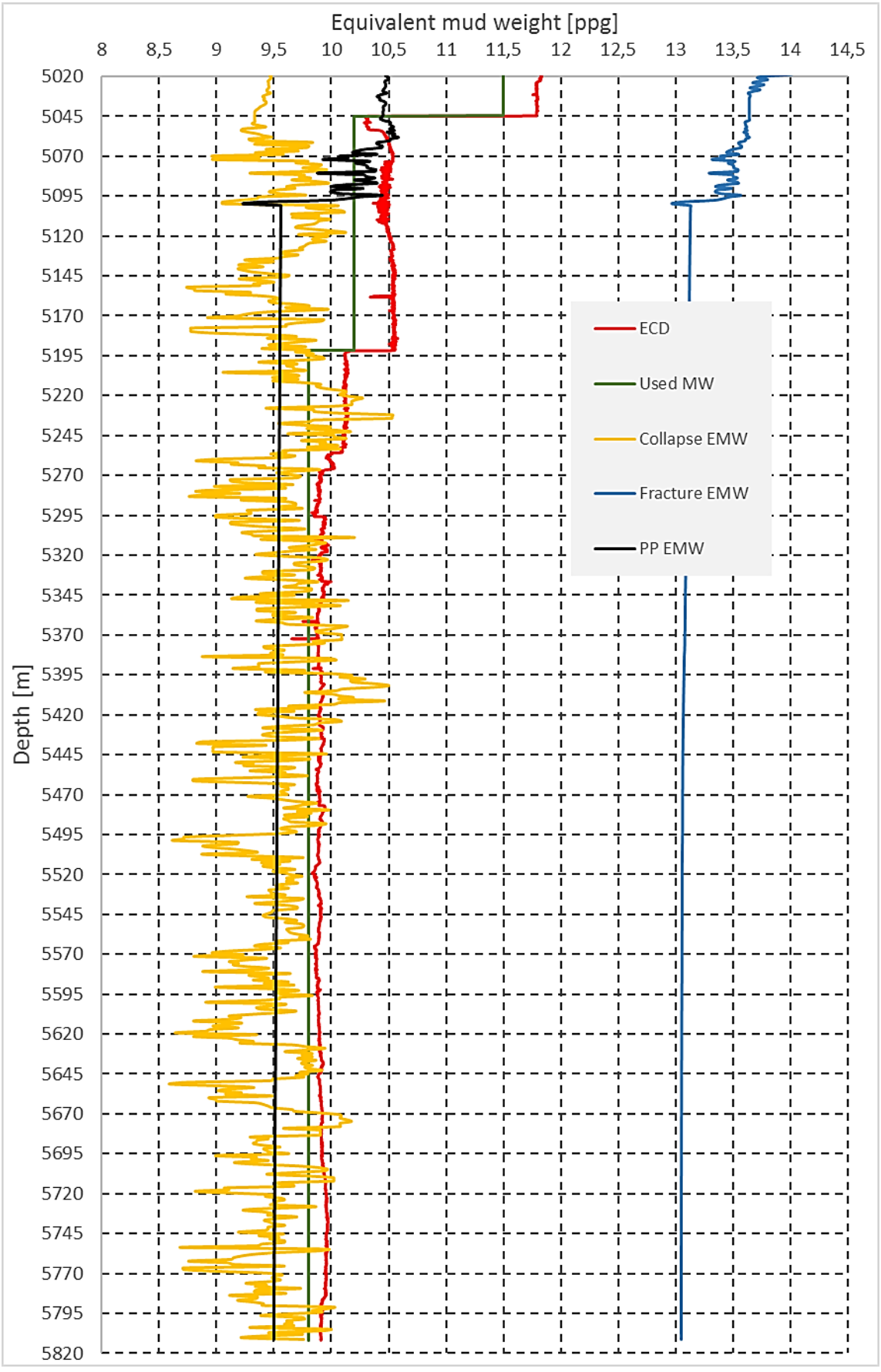

Figure 43: EMW for the 12 ¼ inch section

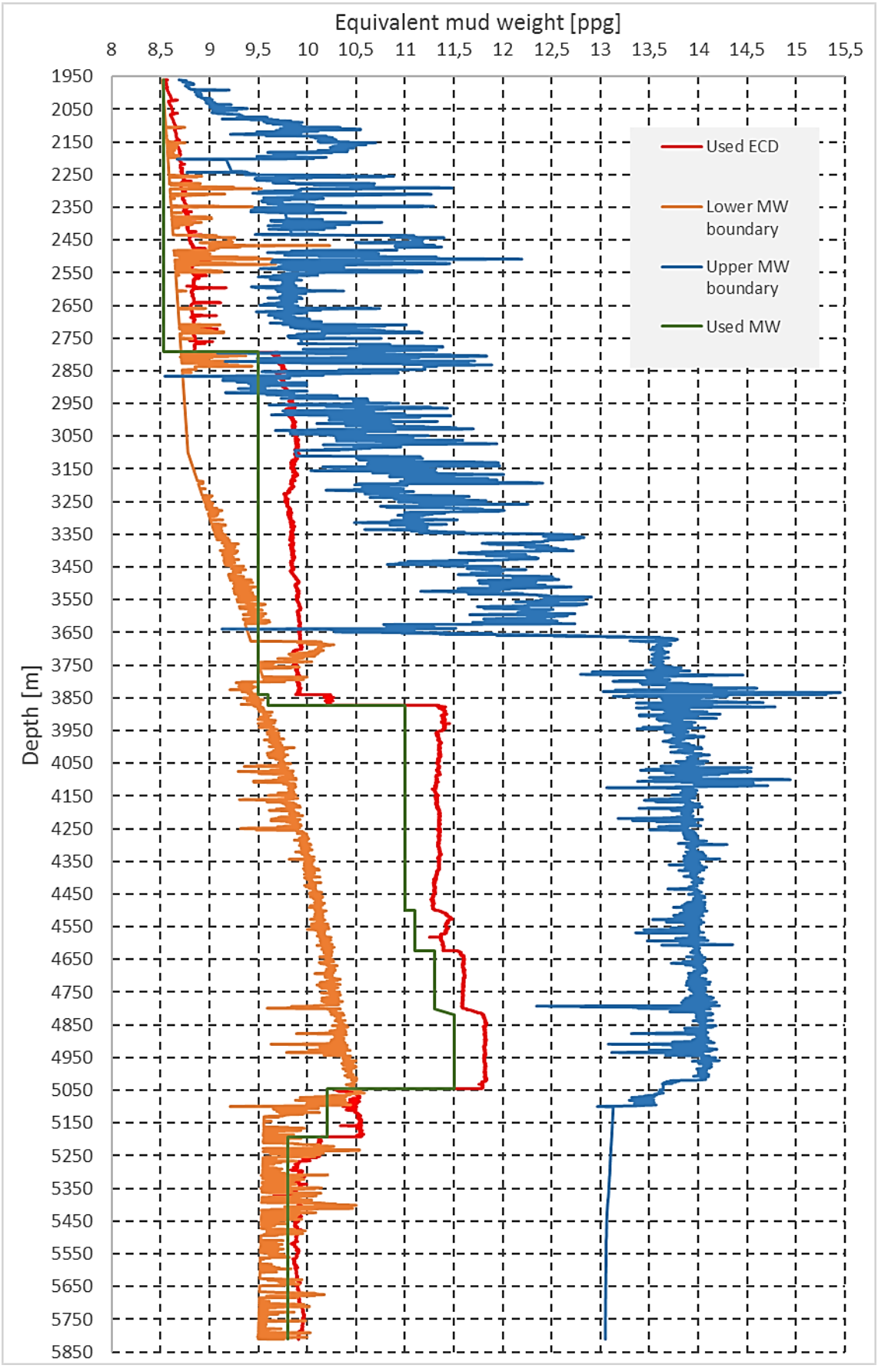

Figure 44: Upper and lower MW boundary with ECD and used MW

3.12 Discussion

In this section the results of the built MEM are discussed. Predicted instability zones are compared to information about instability events from the data set to assess the quality of the model. Looking at the stability plots from the previous section, three main zones of potential instability can be identified. They were marked in Figure 45.

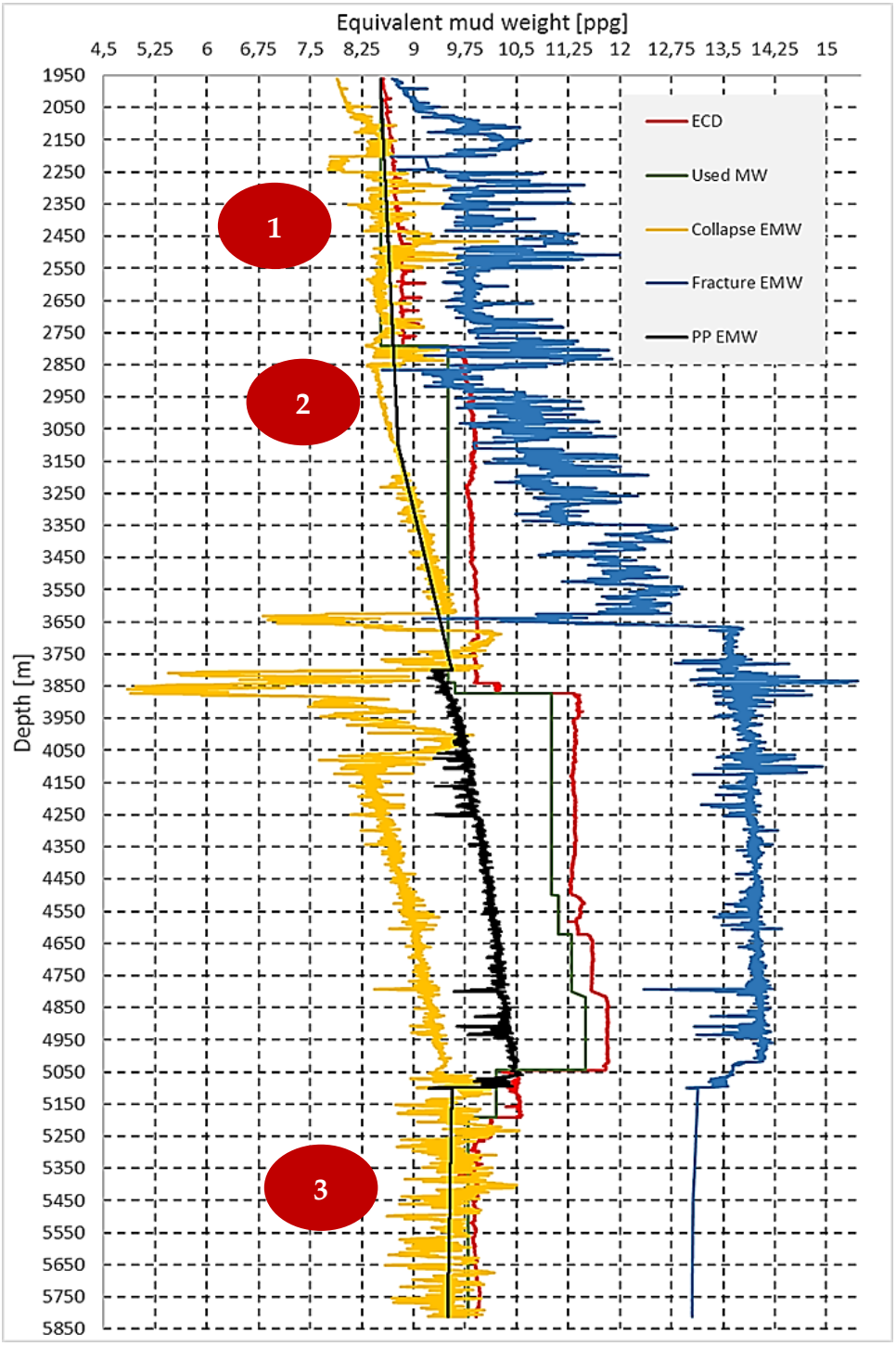

Figure 45: Stability plot with numbered main instability zones

3.12.1 Trouble Zone 1

Figure 40 shows a closer look at the first instability zone. The used ECD was below the collapse pressure on many occasions and the used mud weight was too low most of the time. This indicates that borehole breakouts would occur, especially when the pump is turned off. This would show in a caliper log as increased borehole diameter but no caliper was available for this section of the well. The used mud weight is also below the pore pressure which indicates that influx of pore fluid into the well would occur. The end of well report lists incidents and issues while drilling the well. It was reported that breakouts occurred along the 26 inch section so drilling operations were hampered because of material falling into the wellbore. The model overestimated the collapse and PP EMW as it would indicate more severe problems than were actually reported. According to the calculations, a higher mud weight at around 8.7ppg is recommended.

3.12.2 Trouble Zone 2

For better visibility, Figure 46 shows a detail of trouble zone 2. The spike in collapse EMW was avoided by setting the casing at around 2790 and increasing the mud weight. Although, increasing mud weight was a good solution, the ECD ended up being above the fracture EMW due to the narrow mud window. This would lead to fracturing of the formation and mud loss. The daily drilling reports of the well confirm that these issues occurred after setting the casing and drilling this section. Deeper in the section there was no trouble. The MEM results are in agreement with this except that they imply that collapse occurs near the end of the section. No issues of that sort were reported.

One idea to reduce trouble in this case is to use a lower mud weight of 9.25 ppg between around 2795 m and 2855 m depth. At 2855m the casing should be set, so a new section can be started using a lower mud weight of around 9 ppg to stay below the low fracture EMW between 2865 m and 2925 m depth. The recommended casing depths are shown in another figure for the whole well later in this section. From 2795 m to 2855 m an expandable casing could be optimal solution.

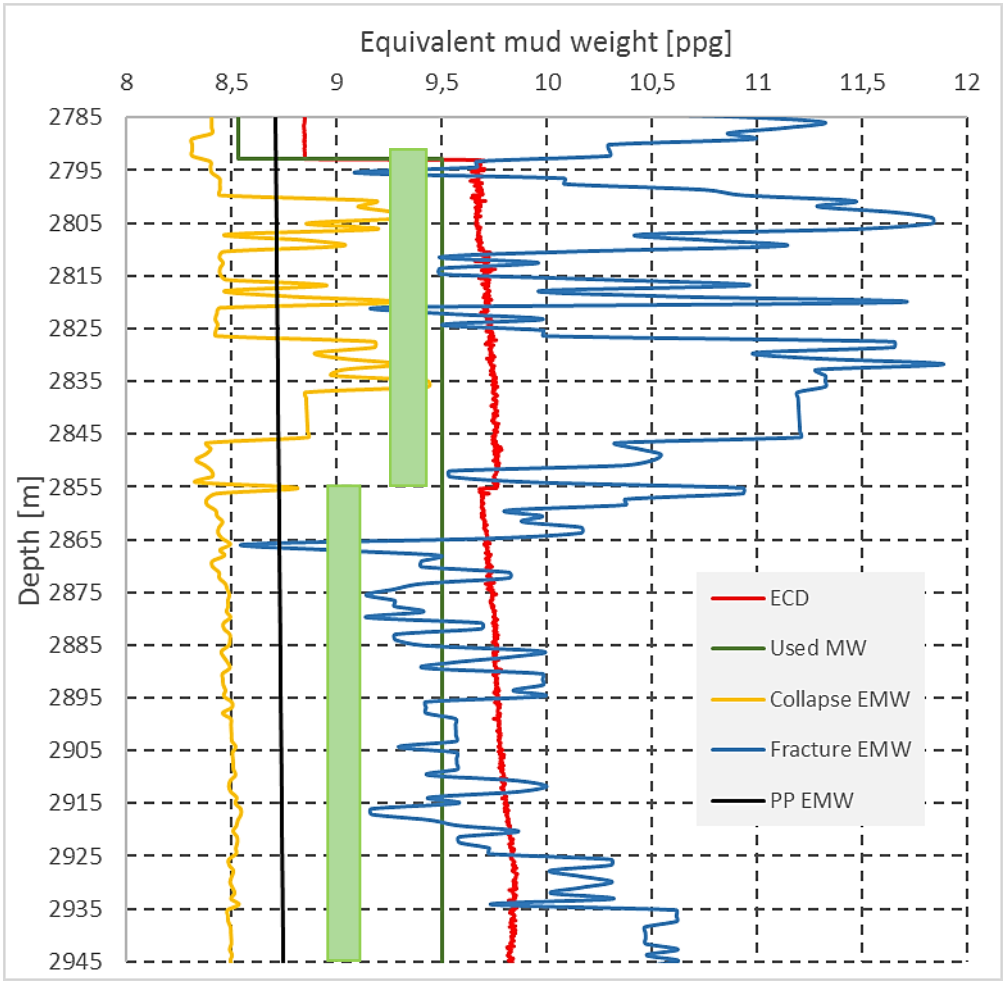

Figure 46: Trouble zone 2. The green boxes indicate the recommended mud weight

3.12.3 Trouble Zone 3

In zone 3, the ECD and used mud weight are below the collapse EMW on many occasions in that section. The breakouts are confirmed in the report and caliper data is available. The report states that the BHA was significantly worn and scratched and it was probably caused by the breakouts and voids measured. Severe losses were recorded and pictures of the worn equipment provided. Many drilling breaks were required. The section had the most severe problem drilling the well.

In the Figure 47 the model is compared with the caliper data. The used bit size was 12.25 inch. According to the caliper readings, collapse predominantly occurred between 5370 m and 5445 m depth. The model predicts a spike in collapse EMW within that interval. The results indicate that generally the chosen mud weight was low and too close to the collapse EMW so breakouts were prevalent. However, it could not accurately predict the other breakouts at around 5505 m and 5615 m depth.

The predicted fracture pressure EMW is high in this section so there is a lot of space for using an increased mud weight. The recommendation according to the model is to use a mud weight of 10.5 ppg.

3.12.4 Recommendation for Casing Seat Selection and Mud Weight

In the analysis of the trouble zones some recommendations were given. They were combined in the recommended design presented in Figure 48. For the recommended casing sizes and depths, it was assumed that the production casing has to stay the same size as designed. A 20 inch expandable liner was used cover the upper section in trouble zone 2. The 16 inch casing had to be set at 3250 m depth to avoid fracturing the formation in the lower part of trouble zone 2. As a result an additional casing had to be set. In order to prevent the required casing sizes to get too large the clearance used is low. Otherwise the required size for the surface casing would increase and require an expendable liner that can be extended to that larger diameter. Another possible approach would be to reduce the last casing size and use normal clearance. In the original design a 7 inch casing was planned as contingency.

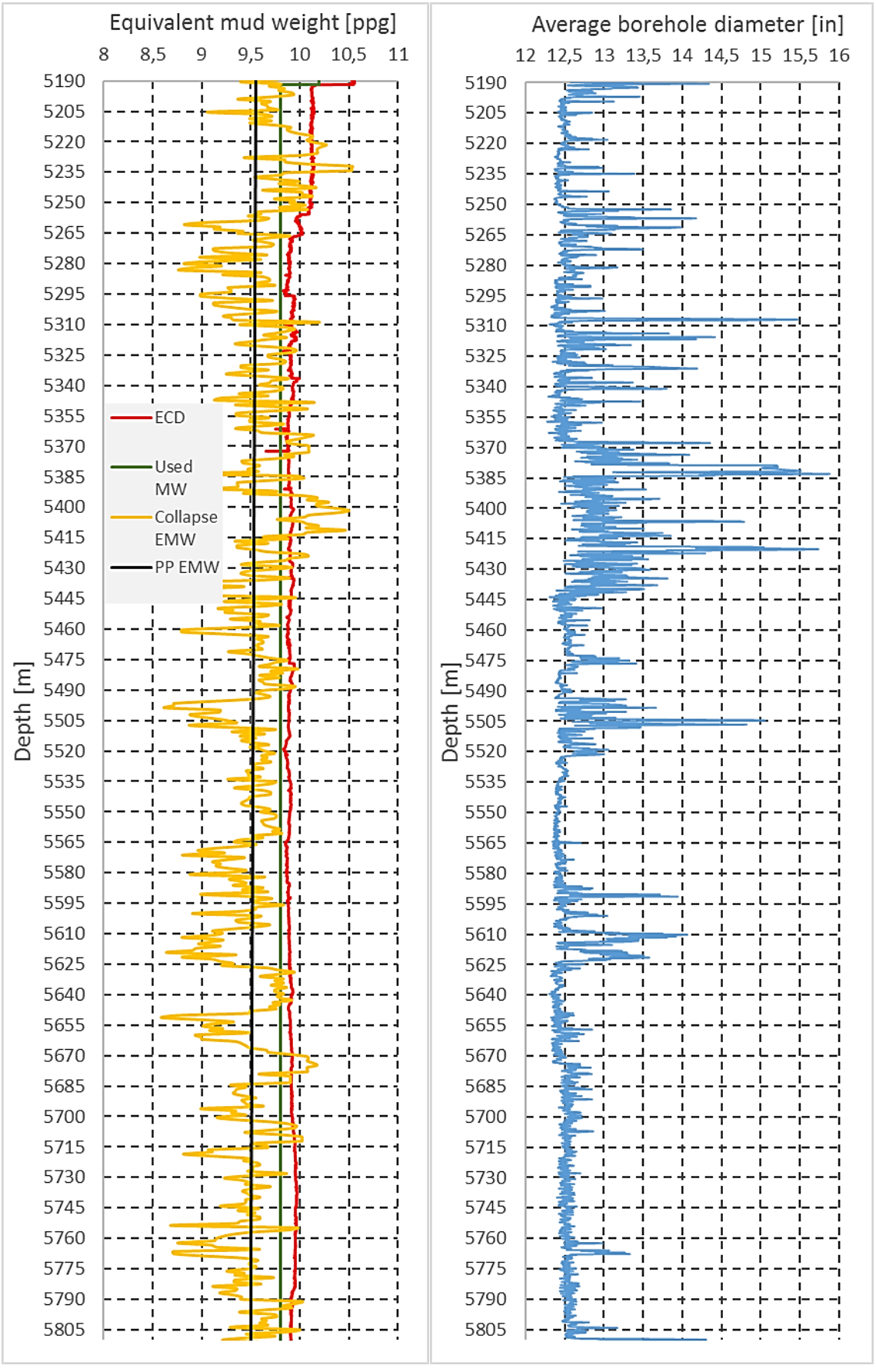

Figure 47: Trouble zone 3 compared with calliper readings on the right

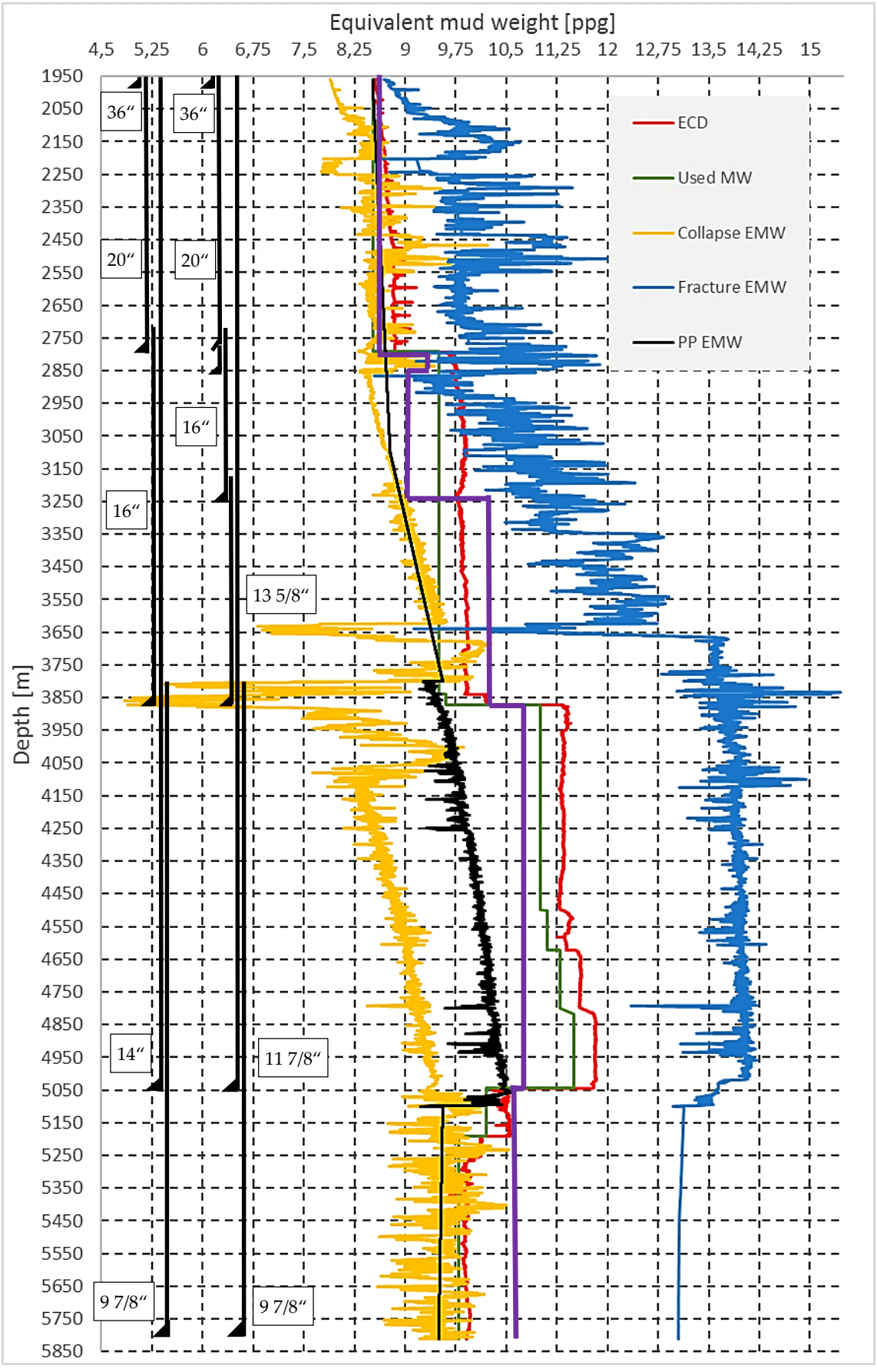

Figure 48:Actual (left) and recommended (right) casing design and MW (purple)

Chapter 4 Conclusion and Recommendations

4.1 Conclusion

While the different parameters in the MEM are interconnected in various ways they fundamentally all stem from the same basic set of log measurements. The results always have to be calibrated using core data, pressure tests, image logs and incident reports from offset wells. The following data is required:

- Sonic slowness/velocity, Bulk density, Gamma ray, Resistivity from logs
- UCS, Young's Modulus, Poisson's Ratio, Angle of internal friction from cores
- Pressure tests, image logs, caliper logs, incident reports for calibration

Some of these can be estimated, worked around or neglected in practical applications, for example the maximum horizontal stress is set to equal the minimum horizontal stress when no reliable images are available. Eaton's method for pore pressure also works with sonic data, so resistivity might not be required. If the mechanical stratigraphy is already known, gamma ray is not required. There is no way around sonic, density and core data. This means that if these measurements are not available, because the logs have not been run in that region or cores have not been tested or retrieved, a model cannot be made. Uncalibrated data is highly uncertain as the difference between calibrated and uncalibrated parameters (e.g. dynamic and static data) are potentially very big. Any uncertainty in the data will increase the uncertainty of the results of the model. Figure 49 summarizes the relationships between the input parameters of the 1D-MEM modeling process of this thesis.

An especially weak point of the MEM is the estimation of the maximum horizontal stress. It requires exotic logs like image logs and the possibility to use pressure test results to estimate it is being disputed in the literature (Zoback 2010). Having to accept such high level of uncertainty for this parameter is unfortunate, as it is a crucial component of further calculations as it is required for the calculation of the induced stresses and thus failure criteria and the resulting safe mud weight.

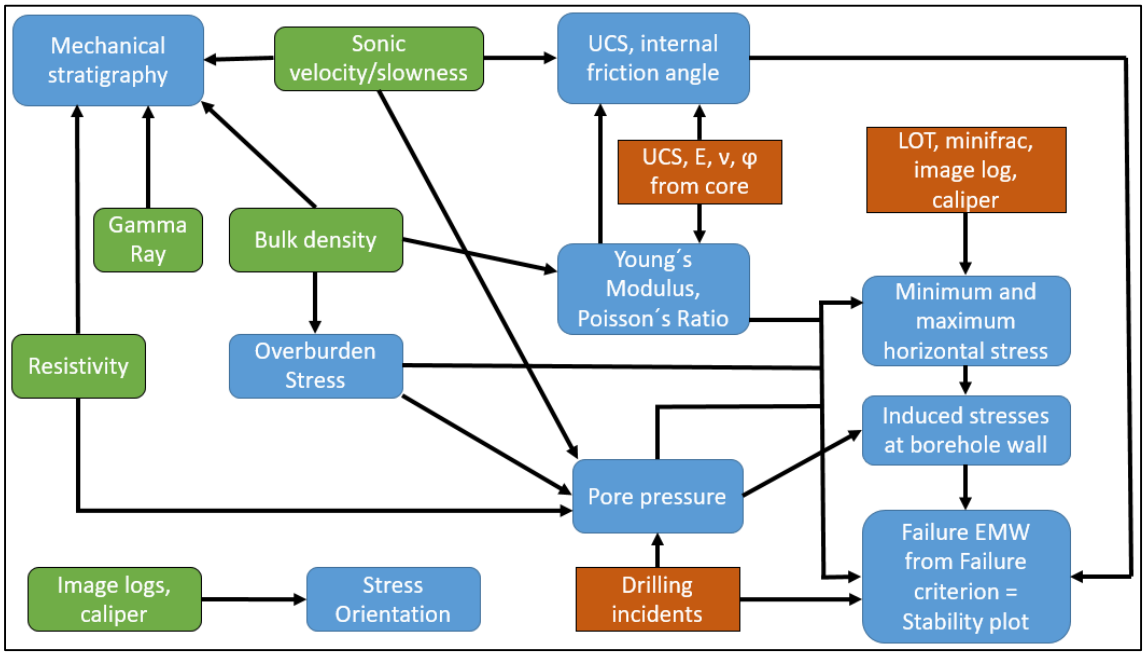

Figure 49: Parameter relationships for the 1D MEM modelling process. Green and brown boxes contain the input measurements, blue boxes contain results

Building the model in the previous chapter, it got clear that core data and pressure tests for calibration are very important. For this data set, some log data such as shear slowness and bulk density was missing for some sections even though it was originally planned to measure them. Core and LOT data was only available for some sections. Additionally, the reliability of the available core and LOT data was questionable. As some data like this for calibration was not available for most sections, assumptions had to be made or the results were left uncalibrated. The more data is not available and the more unreliable it is, the more unreliable the results of the model will get.

Even though multiple assumptions were made, the final results did indicate three main trouble zones that could be validated by incident reports and caliper readings. Some reported incidents were not predicted and some predicted trouble was not mentioned in the reports. It is not clear whether it did not happen or it was simply not reported.

To conclude, the relatively simple 1D MEM built in this thesis enabled predictions that could be validated even though some data for calibration was unavailable. It did not require large amounts of data and professional software to build so using the means available to the industry it is definitely possible to use available data to quickly and economically build a 1D MEM for a well and use it as part of the well planning process to reduce instability and the associated costs. During the drilling process the model should be updated to enhance it. It highly relies on certain log measurements and core

data for calibration so its quality depends on the availability and quality of the input data. The potential savings are high if the data can be managed and used efficiently.

4.2 Recommendations and Future Work

As summarized in the conclusion and presented in Figure 49, a simple 1D MEM for a well only requires data from a few sources. Analyzing publicly accessible data from various wells in Alaska and the Netherlands it was striking that all necessary data never was available. This leads to the impression that the data is usually not collected, especially image logs and core data.

The quality of a MEM is a function of the quality of the data that it uses. If a company plans to engage in a region and drill multiple wells there, as first step, it should make sure to collect all the relevant data to build the preliminary MEM and use it to plan the future wells in the region. The new data collected while drilling a new well can then be used immediately to update the model to reduce uncertainty. Creating the model itself should not be too expensive to offset its benefits, especially using professional software. Most steps of the process could possibly beget automated leading to the possibility of real time application.

Service companies do offer their customers to build a pre-drill MEM from offset data to aid well design and also so called real time geomechanics. This means they will update the pre-drill MEM as the real time data is collected drilling the well. It would be interesting to do further research in collaboration with companies on that topic in order to compare the actual costs of such services and their success rate and benefits.

The operators own the data, so the question arises if they couldn't at least create pre-drill MEM themselves economically. Globally, hundreds of thousands of wells have been already drilled and probably most regions have at least one well already, so the amount of collected data across the industry must be staggering. Proper management and efficient use of that data surely is a challenge for the future that holds a lot of potential for research and optimization.

Bibliography

1) Adewole, E. O.; Healy, D. (2013): Quantifying in Situ Horizontal Stress in the Niger Delta Basin, Nigeria. In *JET* 2 (3).

2) Adisornsuapwat, Kanitthorn; phuat tan, Chee; Anis, Leo; Vantala, Aurifullah; Juman, Reayad; Boyce, Barry (2013): Enhanced Geomechanical Modeling with Advanced Sonic Processing to Delineate and Evaluate Tight Gas Reservoirs. In : SPE Middle East Unconventional Gas Conference and Exhibition. Muscat, Oman, 2011-01-31: Society of Petroleum Engineers.

3) Afsari, Meisam; Ghafoori, Mohammadreza; Roostaeian, Mohammad; Haghshenas, Ashkan; Ataei, Abdolrahim; Masoudi, Rahim (2013): Mechanical Earth Model (MEM): An Effective Tool for Borehole Stability Analysis and Managed Pressure Drilling (Case Study). In : SPE Middle East Oil and Gas Show and Conference. Manama, Bahrain, 2009-03-15: Society of Petroleum Engineers.

4) Ahmed, Sajjad; Khan, Khaqan; Omini, Peter Itam; Aziz, Azly; Ahmed, Mujahed; Yadav, Anurag Singh; Mohiuddin, Mohammad Ahmed (2014): An Integrated Drilling and Geomechanics Approach Helps to Successfully Drill Wells along the Minimum Horizontal Stress Direction in Khuff Reservoirs. In : Abu Dhabi International Petroleum Exhibition and Conference. Abu Dhabi, UAE, 2014-11-10.

5) Al-Ajmi, Adel M. (2012): Mechanical Stability of Horizontal Wellbore Implementing Mogi-Coulomb Law. In *Advances in Petroleum Exploration and Development* 4 (2), pp. 28–36.

6) Ali, A. H. A. et al. (2003): Watching rocks change—Mechanical earth modeling. In *Oilfield Review* 15.

7) Chang, Chandong; Zoback, Mark D.; Khaksar, Abbas (2006): Empirical relations between rock strength and physical properties in sedimentary rocks. In *Journal of Petroleum Science and Engineering* 51 (3-4), pp. 223–237.

8) Colmenares, L.B; Zoback, M.D (2002): A statistical evaluation of intact rock failure criteria constrained by polyaxial test data for five different rocks. In *International Journal of Rock Mechanics and Mining Sciences* 39 (6), pp. 695–729.

9) Formento, Jean-Luc (2004): Seismic Pore Pressure Prediction. In : EAGE. Paris. Available online at http://www.cgg.com/technicaldocuments/cggv_0000001681.pdf, checked on 11/6/2016.

10) Haidary, S. A.; Shehri, H. A.; Abdulraheem, A.; Ahmed, M.; Alqam, M. H. (2015): Wellbore Stability Analysis for Trouble Free Drilling. In : SPE Kuwait Oil and Gas Show and Conference. Mishref, Kuwait, 2015-10-11: Society of Petroleum Engineers.

11) Halliburton (2016): Reduce Non-Productive Time (NPT). Available online at http://www.halliburton.com/en-US/ps/solutions/deepwater/challenges-solutions/reduce-non-productive-time.page?node-id=hgjyd452&Topic=DeepwaterWestAfrica, checked on 11/18/2016.

12) Lake, Larry W.; Fanchi, John R. (2006-2007): Petroleum engineering handbook. Richardson, TX: Society of Petroleum Engineers.

13) Last, N.; Plumb, R.; Harkness, R.; Charlez, P.; Alsen, J.; McLean, M. (2013): An Integrated Approach to Evaluating and Managing Wellbore Instability in the Cusiana Field, Colombia, South America. In : SPE Annual Technical Conference and Exhibition. Dallas, Texas, 1995-10-22: Society of Petroleum Engineers.

14) Lin, Weiren; Yamamoto, Koji; Ito, Hisao; Masago, Hideki; Kawamura, Yoshihisa (2008): Estimation of Minimum Principal Stress from an Extended Leak-off Test Onboard the Chikyu Drilling Vessel and Suggestions for Future Test Procedures. In *Scientific Drilling* (6, July 2008).

15) Mody, Fersheed K. (2013): Bridging the Gap: Challenges in Deploying Leading Edge Geomechanics Technology to Reducing Well Construction Costs. In : SPE/IADC Indian Drilling Technology Conference and Exhibition. Mumbai, India, 2006-10-16: Society of Petroleum Engineers.

16) Najibi, Ali Reza; Ghafoori, Mohammad; Lashkaripour, Gholam Reza; Asef, Mohammad Reza (2015): Empirical relations between strength and static and dynamic elastic properties of Asmari and Sarvak limestones, two main oil reservoirs in Iran. In *Journal of Petroleum Science and Engineering* 126, pp. 78–82.

17) Peng, Suping; Zhang, Jincai (2007): Engineering geology for underground rocks. Berlin, New York: Springer.

18) Plumb, Richard; Edwards, Stephen; Pidcock, Gary; Lee, Donald; Stacey, Brian (2013): The Mechanical Earth Model Concept and Its Application to High-Risk Well Construction Projects. In : IADC/SPE Drilling Conference. New Orleans, Louisiana, 2000-02-23: Society of Petroleum Engineers.

19) Qiu, Kaibin; Gonzalez Felgueroso, Julio; Lalinde, Gabino; Coste, Bernard Jean; Naas, Abdulmajid; Fuller, John (2013): Geomechanics Enables the Success of Horizontal Well Drilling in Libya: A Case Study. In : IADC/SPE Drilling Conference. Orlando, Florida, USA, 2008-03-04: Society of Petroleum Engineers.

20) Schlumberger (2016): Real-Time Drilling Geomechanics. Available online at http://www.slb.com/~/media/Files/dcs/product_sheets/geomechanics/geomechanics_rt_ps.pdf, checked on 11/18/2016.

21) Shaker, Selim (2007): Calibration of Geopressure Predictions using the Normal Compaction Trend: Perception and Pitfall. In *CSEG Recorder*.

22) Song, Lisa (2012): Measurement of Minimum Horizontal Stress from Logging and Drilling Data in Unconventional Oil and Gas. Master thesis. University of Calgary, Alberta. Department of Chemical and Petroleum Engineering.

23) York, Patrick Leon; Prichard, David M.; Dodson, James K.; Dodson, Ted; Rosenberg, Steven Michael; Gala, Deepak; Utama, Budi (2009): Eliminating Non-Productive Time Associated with Drilling through Trouble Zones. In : Offshore Technology Conference. Houston, Texas, 2009-05-04.

24) Zhang, Jincai (2013): Effective stress, porosity, velocity and abnormal pore pressure prediction accounting for compaction disequilibrium and unloading. In *Marine and Petroleum Geology* 45, pp. 2–11.

25) Zhang, Lianyang; Cao, Ping; Radha, K. C. (2010): Evaluation of rock strength criteria for wellbore stability analysis. In *International Journal of Rock Mechanics and Mining Sciences* 47 (8), pp. 1304–1316. DOI: 10.1016/j.ijrmms.2010.09.001.

26) Zoback, Mark D. (2010): Reservoir geomechanics. Cambridge: Cambridge University Press.

Acronyms

1D MEM	One dimensional Mechanical Earth Model
ASCII	American Standard Code for Information Interchange
BHA	Bottom hole assembly
DIF	Drilling induced fracture
DLIS	Digital Log Interchange Standard
ECD	Equivalent circulating density
EMW	Equivalent mud weight
FCP	Fracture closure pressure
FIT	Formation integrity test
LOP	Leak off pressure
LOT	Leak off test
LWD	Logging while drilling
MEM	Mechanical Earth Model
MW	Mud weight
MWD	Measurement while drilling
NPT	Non-productive time
OBG	Overburden gradient
PP	Pore pressure
QC	Quality control
ROP	Rate of penetration
UCS	Unconfined compressive strength
WOB	Weight on bit
XLOT	Extended leak off test
XRD	X-Ray Powder Diffraction

List of Figures

Figure 1: NPT for non sub-salt wellbores in the Gulf of Mexico (York et al. 2009) 1
Figure 2: NPT for sub-salt wellbores in the Gulf of Mexico (York et al. 2009) 2
Figure 3: Typical deep-water narrow margin PP/FG curve (York et al. 2009) 3
Figure 4: Statistical NPT breakdown by drilling event type (Qiu et al. 2013) 4
Figure 5 Thesis flowchart 5
Figure 6: Concept of the MEM (Ali, A. H. A. et al. 2003) 8
Figure 7: MEM construction workflow (Ahmed et al. 2014) 12
Figure 8: Comparison of various published correlations to test data (Najibi et al. 2015) 16
Figure 9: Difference between calculated and measured UCS for shale (Chang et al. 2006) 19
Figure 10: Internal friction angle correlations compared to test data (Chang et al. 2006) 21
Figure 11: Overburden and pore pressure gradients and effective stress (Formento 2004) 22
Figure 12: NCT created from Transit Zone data (Shaker 2007) 24
Figure 13: Stress tensor definitions, transformation and principal stress tensor (Lake, Fanchi 2006-2007) 27
Figure 14: The three faulting regimes and their principal stress magnitudes (Lake, Fanchi 2006-2007) 29
Figure 15: Pressure vs square root of time, closure pressure equals the minimum horizontal stress (Lake, Fanchi 2006-2007) 30
Figure 16: Idealized relationship between pumping pressure and time or volume during an XLOT (Lin et al. 2008) 31
Figure 17: Determination of in-situ stress magnitudes (Haidary et al. 2015) 34
Figure 18: Schematic diagram of a breakout and Kirsch equations (Lake, Fanchi 2006-2007) 35
Figure 19: a) Tensile fractures marked in red on Ultrasonic Televiewer image. b) Breakouts marked in red on electrical image (Zoback 2010) 36
Figure 20: Oil Mud Reservoir Imager (OMRI) tool image showing borehole breakouts and strike orientation towards SE-110 which equals min. horizontal stress direction. Max. horizontal stress is perpendicular, SW-200. (Haidary et al. 2015) 37
Figure 21: Mohr circle and its failure envelope (Peng, Zhang 2007) 39
Figure 22: a) Mohr-Coulomb b) Drucker-Prager c) Mogi-Coulomb criteria applied to triaxial and polyaxial rock strength data (Al-Ajmi 2012) 41
Figure 23: Different mud windows in stability plot (Afsari et al. 2013) 42
Figure 24: Flowchart for building the model using Excel 46
Figure 25: Well schematic 47
Figure 26: Geopressure forecast using offset well data 49
Figure 27: ASCII data file Example 51
Figure 28: Log data in Excel 52
Figure 29: Comparison of unfiltered (left) and filtered (right) bulk density data 53
Figure 30: Overburden stress 54
Figure 31: Static Young's Modulus, log data in blue, core data in orange 55
Figure 32: Static Young's modulus over whole depth 56
Figure 33: UCS for section with cores 58
Figure 34: UCS for the whole depth 59
Figure 35: Pressure profiles in comparison 60
Figure 36:Principal horizontal stresses with overburden stress and core data 62
Figure 37: Induced effective stresses at 3700m 63
Figure 38: Induced effective stresses for the whole depth 64
Figure 39: EMW for whole depth 67

Figure 40: EMW for 26 inch section 68
Figure 41: EMW for 16 inch section 69
Figure 42: EMW for 14 ¾ inch section 70
Figure 43: EMW for the 12 ¼ inch section 71
Figure 44: Upper and lower MW boundary with ECD and used MW 72
Figure 45: Stability plot with numbered main instability zones 73
Figure 46: Trouble zone 2. The green boxes indicate the recommended mud weight 75
Figure 47: Trouble zone 3 compared with calliper readings on the right 77
Figure 48:Actual (left) and recommended (right) casing design and MW (purple) 78
Figure 49: Parameter relationships for the 1D MEM modelling process. Green and brown boxes contain the input measurements, blue boxes contain results 80

List of Tables

Table 1: Relationship between drilling decisions and the mechanical earth model (Plumb et al. 2013) 7
Table 2: Data required for building an MEM (Ali, A. H. A. et al. 2003) 11
Table 3: Various correlations for UCS and static Young's Modulus (Najibi et al. 2015) 15
Table 4: Various published correlations to receive the UCS (Chang et al. 2006) 18
Table 5: Equations for internal friction angle (Chang et al. 2006) 20
Table 6: Grain bulk moduli of common minerals (Song 2012) 33
Table 7: Logging program of the well 48
Table 8: Young's Modulus and UCS measurements from cores 50
Table 9: LOT and Minifrac results 51
Table 10: Pressure test results 61